UNIVERSITÀ DEGLI STUDI DI NAPOLI FEDERICO II

XVIIIth PhD. Course in

"Technologie Innovative per Materiali, Sensori ed Imaging"

GROWTH AND CHARACTERIZATION OF FILMS OF PEROVSKITE BASED ORGANIC-INORGANIC HYBRID MATERIALS FOR ELECTRONICS

by

Fabio Chiarella

PHD. SUPERVISOR:

Prof. Ruggero Vaglio

NAPOLI, DECEMBER 2005

INDEX

Chapter 3: Optical properties and technological impact

Chapter 4: Transport properties and possible applications

Introduction

In this work the synthesis and characterization of two perovskite-based hybrid series of compounds has been mainly treated.

The search for new materials plays a central role in the framework of new technologies and in the field of consume electronics. In the last ten years, in fact, the foreseen possibility of reaching the physical limit of standard semiconductor technology, has required the search of new ideas to develop new device concepts. In particular an extraordinary growth has been registered in organic electronics were the availability of cheaper materials and technologies could generate new applications and form factors to drive the growing needs for pervasive computing and enhanced connectivity.

The research in organic-inorganic hybrids in the last years was focused on using the range of interactions found within organic and inorganic worlds in order to create, design and engineering new materials with the desired, innovative or increased functionalities relative to that achievable with organic and inorganic materials alone.

The attention in this work has been focused on the perovskite based hybrid compounds, proposed by D. B. Mitzi of IBM research center, that represent a remarkable example for potentially useful physical properties, including enhanced exciton binding energies, nonlinear optical properties, electroluminescence, organic-like mobility, magnetic response, good conductivity and other interesting properties.

The advantage of the hybrid compounds is mostly related to the greater thermal stability related to full long-range structural ordering in respect to ordinary organic compounds, without losing flexibility and simple processability that represent the main attractive for low-cost electronics. Simple processability, in organic-inorganic compounds, as the perovskite based hybrids, is in many cases overdrew by self-assembling properties.

In this thesis work, the attention has been focused on two series of compounds: $(C_nH_{2n+1}NH_3)_2CuCl_4$ (where n =1,…,4) and $CH_3NH_3SnX_3$ (where X =Cl and Br) where alkylammonium chains are the organic components while the constituent unit of the inorganic structure is the octahedral cluster MX_6^{4-}. The bonding between organic and inorganic components is realized by an ordinary ammine group (NH_3^+) that realizes an hydrogen/ionic bond with the halogen atoms.

The choice of these two classes of compound is related to the interesting electrical, magnetic and optical properties of the isostructural compounds reported in literature. The possibility to synthesize and study optical properties of transition metal halide compounds has been explored in view of exploiting such a potentiality and to find new materials for UV-LED applications and conductive compounds with organic-like or enhanced mobility. In the framework of the research of enhanced mobilities materials, in fact, hybrid compounds have stimulated a great interest. As for analogues inorganic oxide-based perovskite layered family, metal-semiconductor transitions as a function of the perovskite layer thickness have been reported in literature in the tin (II) <100> and <110> oriented perovskite families. This first example of conducting layered organic-inorganic halides enable an examination of the electrical transport properties as a function of the dimensionality of the metal halide framework

In **Chapter 1** of this thesis work, it is proposed an introduction on the world of new materials for electronics and a brief overview of hybrid compounds with particular attention on the perovskite based ones.

In **Chapter 2** synthesis problems and the possible techniques for the realization of polycrystalline powders and films of the two series of selected materials are discussed. In fact, many potential applications involving the organic-inorganic hybrids depend on the availability of simple and reliable thin film deposition techniques.

On this base, a single source evaporative technique (Single Source Thermal Ablation)

has been used for film deposition. The obtained films were primarily investigated and optimized in respect to the crystallographic quality. The main technique used for the determination of the structural properties of the films realized by SSTA is X-rays diffraction. $CH_3NH_3SnCl_3$ is the more complex compound to be realized in thin film form. Its surface has been also deeply investigated by AFM (Atomic Force Microscope) and SEM (Scanning electron Microscope) analysis.

In the **Chapter 3**, it is analyzed the change in the optical properties with the change of one component in the 2D $[(C_nH_{2n+1}NH_3)_2CuCl_4]$ and 3D $[CH_3NH_3SnX_3]$ series structure to understand the possible correlations between structure and optical behavior. Besides, the 2D layered hybrid structures have attracted the scientists' interest because these systems act as artificial multi-quantum well structures. In principle in this type of structure it is possible to obtain excitonic states and, as a consequence, photoluminescence and electroluminescence, by quantum and dielectric confinement effects. Moreover, the intrinsic two-dimensional layered structure of some hybrids, added to self-assembling properties, can lead to the possibility to design and synthesize an emitter material with the capability to control electron/hole drain and separation.

Analysis of the absorption data was carried out to test the optical quality of SSTA deposited films as well as to determine the predominant optical transition and electronic configuration, while the presence of excitonic transitions has been investigated by photoluminescence measurements performed on the films.

In the **Chapter 4**, transport properties of perovskite based hybrid materials have been discussed. Resistivity and its temperature dependence has been measured by standard technique for the deposited films of the two series, while the $CH_3NH_3SnBr_3$ film mobility was determined by field effect analysis. A field effect device based on a $SrTiO_3$ dielectric substrate has been realized and characterized varying gate voltages and temperature. Finally a study on the sensitivity to humidity of the much hygroscopic compounds has been reported, that shows the high potentialities of these materials also for sensor applications.

Chapter 1

Hybrid organic-inorganic materials

1.1 Low cost electronics: devices, materials and technologies

In the last 50 years, traditional electronics has carried a constant growth, producing devices at lower cost and with enhanced performances, responding to the requirement of the market. The developed technologies, related to inorganic semiconductors, insulators, and metals, have been the backbone of this extraordinary industrial success. In the last ten years an extraordinary growth of the consumer electronics sector has been registered too. The increasing demand of connection between communication and information technologies and the foreseen possibility of reaching the physical limit of semiconductor technology, have required the search of new ideas and technologies. In particular a wide research effort was dedicated to develop cheaper materials and technologies that could

"generate new applications and form factors to address the growing needs for pervasive computing and enhanced connectivity", as written by J. M. Shaw in the introduction article of the IBM journal first 2001 issue [1], dedicated to 'organic electronics'.

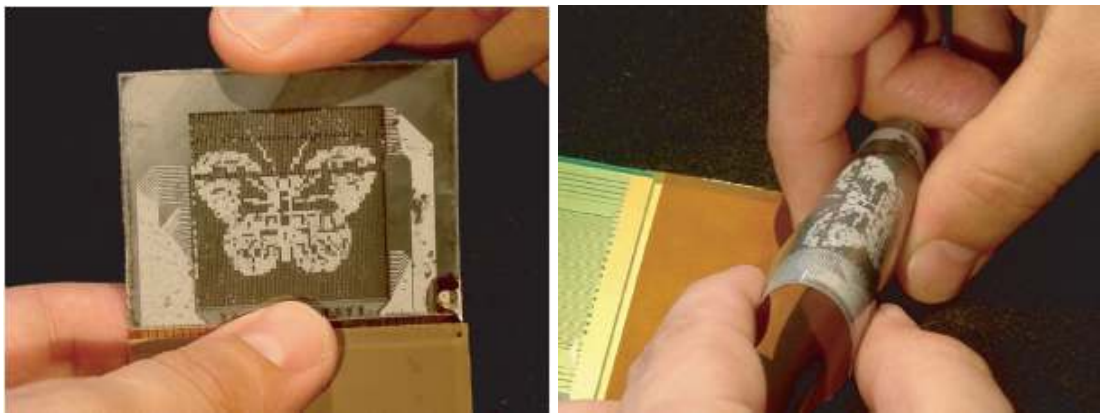

Figure 1.1 – *Philips active-matrix display driven by solution-processed pentacene transistors. Photographs of the electrophoretic display on the left and while bent to a curvature radius of ~1 cm on the right. The 3.5 cm by 3.5cm display has 64 × 64 pixels. Pixel size is 540 × 540 μm^2.The row electrodes are driven at –27V during the line selection time and 23 V during the remaining frame time of 20 ms. The electronic ink is driven at ±15V.The common electrode voltage is set to 4 V to compensate for capacitive coupling between the gate and pixel electrode* [2].

Some organic materials were already known in the world of electronics for "passive" uses (photoresist, protection layers, etc.), but what is so attracting in organic electronics? The main point is that organics, and polymers in particular, can be synthesized using easy and cheap techniques, thanks to the huge variety of combinations between their components (chains and radicals). Moreover, it is possible to obtain tunable electronic properties and to process these active materials at low temperature on large areas as well as plastic or paper materials [3,2], using unique technologies and new functionalities. All these characters can meet industry requirements and fascinate scientists (an example is shown in **Figure 1.1**).

The material functionalities required to have low cost electronics are: memory effect to storage information, efficient light emitting properties to realize active matrix devices for display, high mobility in thin film transistors to perform logic functions and computing, as well as cheaper processability.

In the past 50 years, the organic semiconductors (from polymers and oligomers to single organic molecules) were considered mostly a scientific curiosity, but in any case they have been the subject of an intense scientific investigation. This work, due to the recent key

contributions, has now reached a relative maturity, with a growing industrial interest for both passive and active components.

In particular organic materials have provided improved performances and reliability for storage products and displays. The density of magnetic storage has increased at an even faster rate compared to semiconductor devices. The resolution of displays based on active matrix liquid crystals is approaching photographic quality. Similar enhancements in performance have been seen in the development of organic light-emitting diodes (OLEDs) (see **Figure 1.2**) that have shown a higher luminous efficiency in respect to incandescent light bulbs. Evaporated films of pentacene have achieved mobilities comparable to that of amorphous silicon used to realize the electronic devices to pilot the liquid crystal pixels in LCD technology. In addition to these properties, these materials in thin film form possess good mechanical properties, as flexibility and toughness, and can be processed by solution casting, ink-jet printing, and stamping. These roll-to-roll technologies could lead to new applications and lower production costs.

Figure 1.2 – *Same examples of the use of OLED (Organic Light Emitting Diode) technologies in displays of commercialized products.*

The main difference between organic and inorganic semiconductors is that excitations in inorganic matter are delocalized, described by a wave vector *k*, while in organic matter, excitations are usually localized and *k* is not a good quantum number. The key to understand this lies in the chemistry of carbon and its neighborhoods. Carbon has the characteristic feature to bond with itself and a huge set of elements generating more then 10 million of compounds.

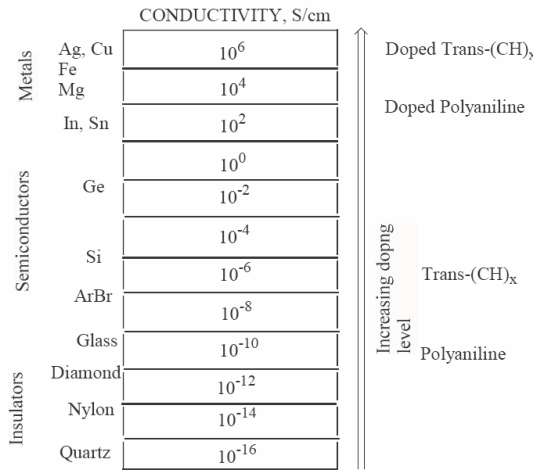

Figure 1.3 – *Table of conductivity of inorganic materials in respect to increasing doping in organic polymers. To obtain p-type doping it is needed an oxidizing element, whereas reducing elements are required to obtain a n-type doping.*

Organic materials weak intermolecular bonds give rise to their semiconducting or insulating properties. The general argument given by Peierls, affirms that a one-dimensional metal cannot exist (*Peierls' transition*) [4]. This seems to exclude the possibility of metallic polymers.

However, organic semiconductors can be made quasimetallic if a high level of doping is introduced [5] as show in **Figure 1.3** and this drives the possibility to utilize these materials in electronics as active or passive elements as already discussed. Unfortunately, the potential of a wide use of organic active electronics devices such as solar cell, light emitters, and thin-film transistors remains still partially unfulfilled mostly because organic materials have often proved to be unstable. On the other hand, the low carrier mobility characteristics, due to low order parameters, prevents their common use in fast electronic applications (greater then 10 *MHz*).

To increase electrical conduction properties (conductivity and mobility) the main route, after introducing an high doping level as discussed before**,** is to enhance crystallinity (long range order) as show in **Figure 1.4.** The reason for low crystallinity is mainly due to the thermal instability of organic molecules, in turn due to the weak intermolecular bonds whose energies are comparable with the thermal vibration energies of the molecules. Finally, it is worth mentioning that it is not easy to make reliable electrical contacts to organic materials, and that when exposed to air, water or ultraviolet light, their electronic properties can degrade rapidly needing for protection (encapsulation).

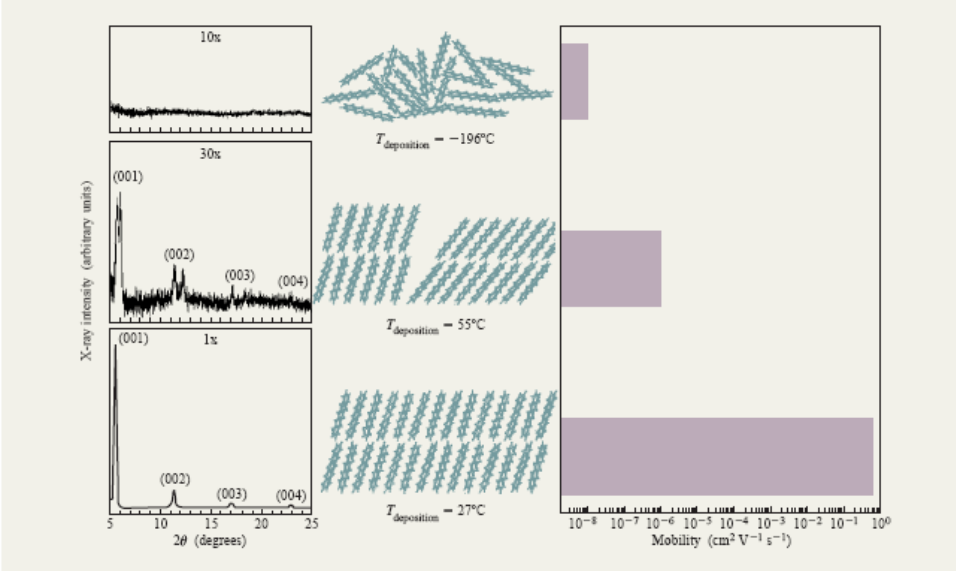

Figure 1.4 – *Comparison of X-ray diffraction patterns, schematic representations of structural order, and field-effect mobilities for three different phases of thin-film pentacene. An amorphous phase is achieved using a substrate temperature, $T_{deposition}$, of −196°C and a deposition rate DR of 0.5 Å s^{-1}. A single phase results at the temperature $T_{deposition}$ = 27°C and DR = 1 Å s^{-1}, while $T_{deposition}$ = 55°C and DR = 0.25 Å s^{-1} yields a double phase. Data partially taken from* [6].

In this framework, the class of hybrid materials composed of both organic and inorganic units at nanometric scale can give very interesting perspectives. The research in organic-inorganic hybrids in the last years has focused on using the range of interactions found within organic and inorganic worlds in order to create, project and engineering new materials with the desired, innovative or increased functionalities relative to that achievable with organic and inorganic materials alone.

1.2 Organic-inorganic hybrid materials

The search for new materials plays a central role in the framework of new technologies for electronics.

Hybrid structures, based on a molecular scale intercalation of inorganic and organic components, offer wide opportunities for new functional materials for scientific exploration and technological applications.

Nature exhibits a large number of examples in which organic-inorganic hybrid materials are utilized. One interesting example of this is a gastropod mollusk shell (*Trochus niloticus*). The section of this mollusk shell (**Figure 1.5**) consist of a highly organized laminated microstructure of aragonite $CaCO_3$ crystals (0.5 μm thick) separated by a thin layer (50 *nm*) of proteinaceous organic matter. The resultant strength and fracture toughness of this "brick and mortar" microstructure is order of magnitude greater than each of the components [7].

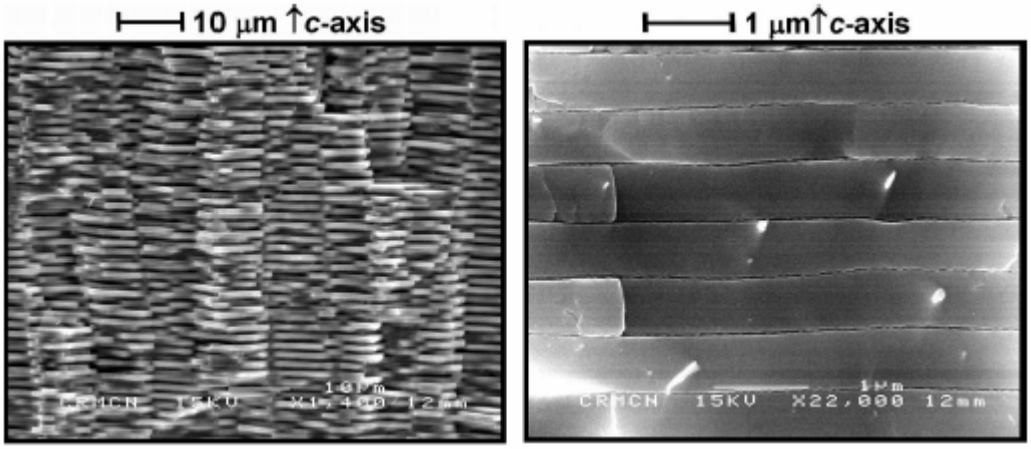

Figure 1.5 – *SEM images of side view of inner laminated, columnar nacreous microstructure of Trochus niloticus freshly fractured. The two pictures show a different enlargement of the lamellar structure* [7].

Learning from natural systems, technologies based on synthetic hybrid composites have experienced a significant improvement. Molecular dispersed polymer/layered silicate nanocomposites have shown an high degree of stiffness, strength, heat resistance and barrier properties, with far less inorganic content than comparable glass or mineral

reinforced "filled" polymers with a remarkable reduction in weight. These structures with enhanced performances, are a result of the molecular scale interaction between the two components [8,9]. An example is a polymer composite based on modified phyllosilicates (organoclay) and poly-(ethylene-*co*-vinyl acetate) (EVA) prepared by melt processing to study their combustion behavior. Tuning the degree of dispersion and intercalation spacing and changing type of organoclay in these materials, it is possible to obtain either a microcomposite or an exfoliated nanocomposite. Combustion experiments showed that the microcomposite burns in the same way as the pure polymer (EVA), whereas the heat release is reduced by 70-80% when nanocomposites with low silicate loadings (2-5%) are burned, because a protective charred ceramic surface layer is formed as a result of reassembly of the clay layers and catalyzed charring of the polymer. So less than 5% nanoscopic dispersion of inorganic lamellas in the polymer matrix leads to hybrid composites enhanced properties of fire extinction that cannot be reached with the same fillers dispersed at microscopic level (**Figure 1.6**) [10].

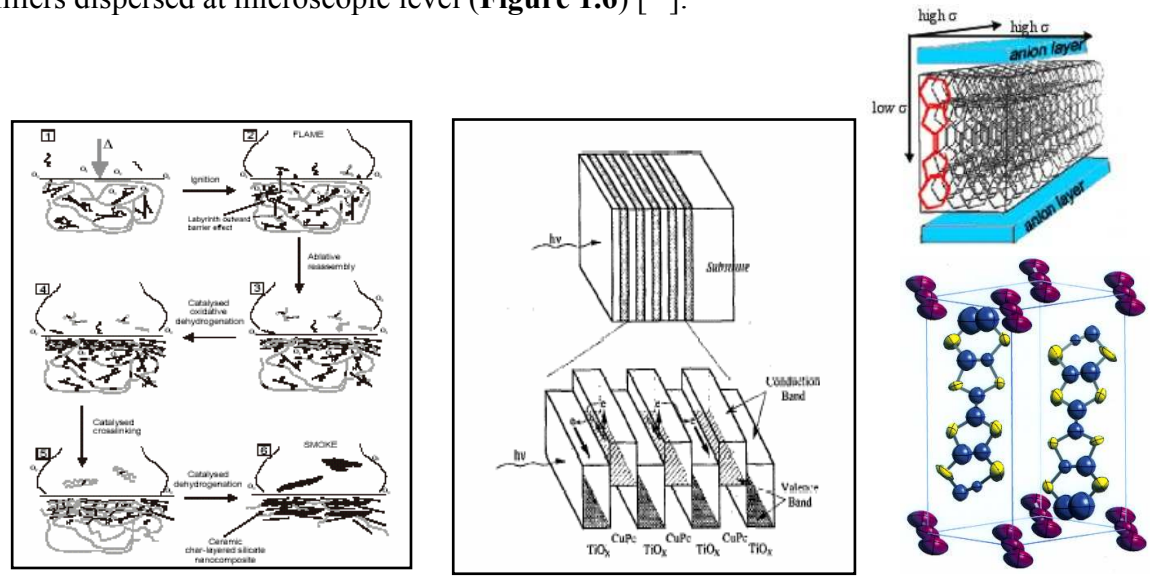

Figure 1.6 – *On the left side: schematic representation of fast extinction process of a flame for an exfoliated hybrid nanocomposite (EVA-LNC)*[10]. *At the center: CuPc/TiO_x heteromultilayer structure for a new concept of optoelectronic material* [11].*On the right-up side: a schematic crystal structure of a BEDT-TTF based organic conductor. A single BEDT-TTF molecule is shown in red. On the right-down side: crystal cell of $(BEDT\text{-}TTF)_2I_3$ superconductor (Tc=8 K).*

Organic-inorganic superlattices, created using sequential evaporation of organic and inorganic layers, are another area of active interest for solar cell and light emitting devices. Takada et al. [11] created a heteromultilayer structure consisting of alternating amorphous

layers of copper phthalocyanine (CuPc) and TiO_x, with an artificial periodicity greater than 50 Å (**Figure 1.6**). This hybrid multilayer is found to exhibit 40 times higher photoconductivity than an organic CuPc single layer, commonly used as photoelectron converter. This enhanced performance has been attributed to the fact that TiO_x has a larger energy gap and therefore exhibits no photoconductive sensitivity over most of the visible spectrum, but it has a larger electron affinity and a substantially larger mobility (0.1–1 $cm^2/V\,s$). In this way, the electrons generated in the CuPc layers are expected to transfer to the TiO_x layer. By physically separating holes from electrons, the probability of recombination reduces and the photoconductivity should be enhanced over the value observed for pure CuPc thin films. Another similar example is a heteromultilayer of MgF_2 and 8-Hydroxyquinoline aluminum (Alq) [12].

To conclude this brief overview on the huge world of hybrid materials, we should mention the organic superconductors, that represent a very different example from the previous ones. It is known that polymers or organic molecular aggregates, doped with inorganic atoms or cluster, can be conductors and, in some fascinating cases, even superconductors (as the doped fullerene K_3C_{60}). Organic superconductivity was first theorized in 1964 by Little [13], but its discovery dates 1979, when the "*Bechgaard salts*" $(TMTSF)_2ClO_4$, a synthetic metal based on organic molecules, drew attention because it gave the first evidence of superconductivity in any organic material (T_c=1.2 K at ambient pressure) [14]. These crystalline hybrid compounds consist of an electron donor, typically a planar organic molecule, and an electron acceptor, an inorganic anion cluster (**Figure 1.6**). The critical transition temperatures of these superconductors are small, comparable with conventional metallic superconductors. The record (in 2002) is still held by the k-$(ET)_2Cu[N(CN)_2]Cl$ compound with a transition temperature of about 12 K (at 0.3 Kbar) [15]. However they show very interesting properties. As an example, the critical magnetic field for $(TMTSF)_2PF_6$ is 6 T, a fairly large value even for conventional metallic superconductors.

As in these examples, all different hybrid compounds share the peculiarity that enhanced performances and new functionalities are born from the intimate interconnection, at nanometric level, of organic and inorganic components. Inorganic materials offer the potential for a wide range of electronic properties (enabling the design of insulators, semiconductors, metals and superconductors), magnetic and dielectric transitions,

mechanical hardness, and thermal stability. The organic molecules provide high fluorescence efficiency, large polarizability, plastic mechanical properties, easy of processing and versatility. In some cases, an even more very fascinating possibility arises from the formation of fully new phenomena at the interfaces between the organic and the inorganic subunits.

Hybrid compounds with full long-range structural ordering, can have a special role as new materials for low-cost electronics. The advantage of these compounds is mostly related to the greater thermal stability in respect to ordinary organic compounds, without losing flexibility and simple processability. In particular, perovskite based hybrid compounds are a remarkable example for potentially useful physical properties including enhanced exciton binding energies, nonlinear optical properties, electroluminescence, organic-like mobility, magnetic properties, conductivity and other properties.

The relevance of these compounds is also related to the possibility to deposit thin films on flexible and amorphous substrates with good crystalline quality thanks to their self-assembling properties, as described below.

1.3 Self-assembled systems

Self-assembly is one of the most important strategies used in biology for the development of complex, functional structures. There are countless examples of self-assembly all around us, from molecular crystals to mammals. The crucial idea for this area is the "molecular shaping", the interplay between enthalpy and entropy (thermodynamical stability), and the nature of non-covalent forces that connect the particles in self-assembled molecular aggregates. In particular “self-assembling” and “self-organizing” terms were born in bio-chemical ambient to mean the natural formation of “high complexity” structures through the interaction of a number of different types of forces between its components. In other words, the constituents of a self-assemble material are naturally functionalized to bond together into an ordered, complex structure. Obviously stressing the

self-assembling concept, also an inorganic salt can be considered a self-assembled materials because atoms "create" the structure by ionic (or covalent) bonding, without having to force them into this configuration or to manipulate them to realize the structure. In this way, the term "self-assembling" becomes somewhat vague. Therefore, from the point of view of applications and new technologies, the term has the beneficial connotation of "easy and cheap to make".

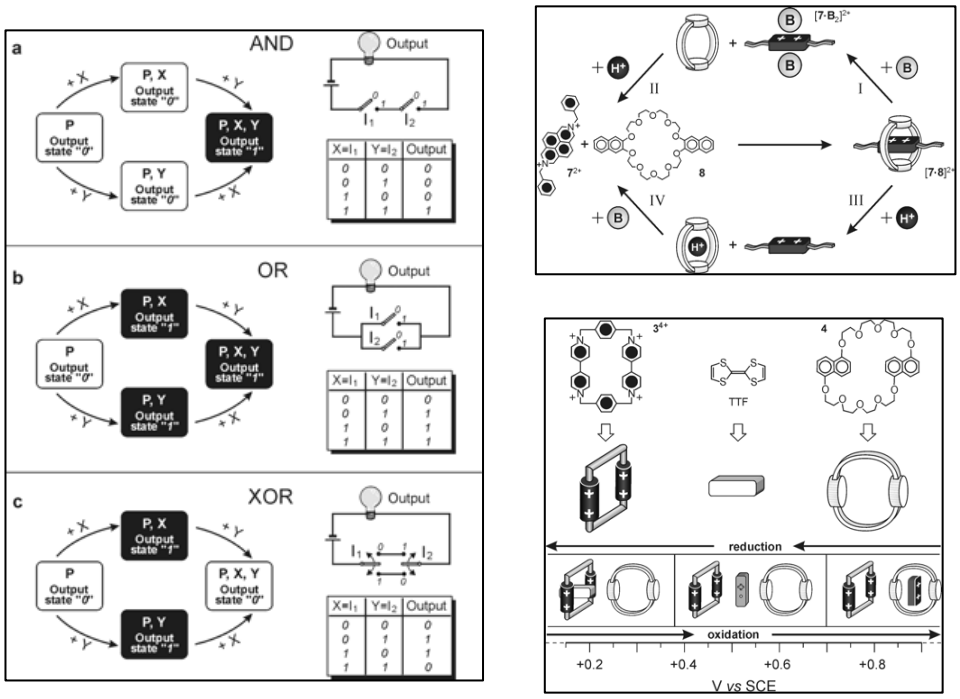

Figure 1.7– *On the right-down side: components of a three-pole supramolecular switch and schematic representation of the ranges of electrochemical stability of the three states available to the system. On the left side: schematic representation of a chemical system (P) which performs the AND (a), OR (b), and XOR (c) logic operations under the action of two chemical inputs (X and Y). The truth tables of such operations are also shown, along with their representations based on electric circuit schemes. On the right-up side: schematic representation of the threading/dethreading pattern of pseudorotaxane* ***[7·8]***$^{2+}$*, which corresponds to an XOR logic function.* [18].

Self-assembly strategy has some advantages:

a) Molecular self-assembly is a strategy for nanofabrication that involves designing molecules and supramolecular entities so that shape-complementarity causes them to aggregate into the desired structures. It carries out many of the most difficult steps in

nanofabrication, those involving atomic-level modification of the structures, using the very highly developed techniques of synthetic chemistry.

b) It takes inspiration from the enormous wealth of examples in biology.

c) It can incorporate biological structures directly as components in the final systems.

d) It tends to produce structures that are relatively defect-free and self-healing because it requires that the target structures be the thermodynamically most stable ones between the possible configurations.

There are a range of different molecular systems that make self-assembling. An example are the so-called self-assembled monolayers (SAMs) that form ordered, monomolecular structures, realized by the coordination of molecules to a surfaces. These structure are reasonably well understood, and increasingly useful technologically [16]. Another example are the molecular machine systems in which self-assembling and stimulated disassembling states can be designed to perform controlled switching, photo-switched conductors [17], photo-chemically driven pistons, or logic gates (**Figure 1.7**) [18].

Hybrid organic-inorganic compounds, as the perovskite based hybrids [19], possess in many cases self-assembling properties. These materials involve different types of interactions allowing the assembly of relative complex and highly ordered structures. The relevant interactions giving rise to crystalline assembly within the hybrid perovskites include covalent/ionic bonding (which favors the formation of sheets of corner-sharing metal halide octahedra), hydrogen/ionic bonding between the organic cations and the halogens in the inorganic sheets, and various weaker interactions (van der Waals, π–π, etc.) between the organic R-groups. These interactions generate a propensity of the organic cations to align in a tail-to-tail arrangement, with the ammonium group hydrogen bonding to the halogens in the inorganic cluster, and the tendency of many metal halides to form extended corner-sharing networks of MX_6 octahedra. All these reasons induce the self-assembly features of the perovskite hybrid compounds.

1.4 Perovskite based hybrid compounds

In this thesis work, attention has been addressed to hybrid perovskite based compounds of interest for electronic applications.

As already stated, organic-inorganic hybrid compounds put together the thermal stability and the elevated structural order degree of inorganic components with the interesting characteristics of organic materials as functional versatility, mechanical flexibility and low cost processability. This possibility of merging typical inorganic crystals properties with those of molecular organic solids has stimulated attention in the last 15 years [[20]].

Perovskite based hybrids can be synthesized with simple and cheep techniques thanks to their self-assembling character [[21]] and are very interesting both for fundamental physics exploration (Jahn-Teller distortion effect and perovskite system study [[22,23]], low dimensional magnetic system [[24,25]], electronic confinement [[26]], etc.) and technological applications. It has been demonstrated, in fact, the possibility to fabricate opto-electronic devices (as Thin Film Transistor or Organic-Inorganic Emitting Diode) utilizing perovskite hybrids as active materials ($(C_6H_5C_2H_4NH_3)_2PbCl_4$ in OILED [[27]], $(C_6H_5C_2H_4NH_3)_2SnI_4$ in OIFET [[28]]), obtaining comparable performances in respect to typical organic materials.

The mixing of organic molecules and inorganic clusters, through the use of the entire set of interactions present in the nature, is the typical goal of material science and engineering, allowing the design of brand new materials.

1.4.a Perovskites

The basic building component of organic-inorganic perovskite hybrids is the AMX_3 perovskite structure (**Figure 1.8**). This simple structure consists of a 3D network corner-sharing MX_6 octahedra, where the A cations are located in the larger 12-fold coordinated hales between the octahedra. It is typically composed from a metal cation (M) and its ligant anions as O^{2-}, Cl^-, Br^-, I^-, or S^{2-} [[29]].

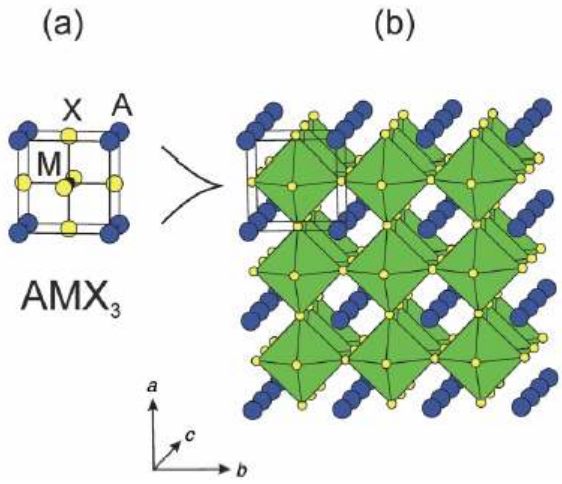

Figure 1.8 – (a) *Ball and stick model of the basic AMX_3 perovskite unit cell and* (b) *polyhedral representation of how the structure extends in three dimensions.*

The stability of the perovskite structure has been rationalized in terms of a parameter, termed Goldschmidt tolerance factor, t , defined as:

$$t = \frac{r_{A-X}}{\sqrt{2} \cdot r_{M-X}} \tag{1.1}$$

where r_{A-X} and r_{M-X} are the distances A-X and M-X respectively. These distances are generally expressed in terms of the ionic radii of the atoms that compose the unit cell [30]. The more the t parameter is close to unity ($r_{A-X} = \sqrt{2} \cdot r_{M-X}$), the greater is the stability of the perovskite structure. As an example $BaTiO_3$ has a tolerance factor ~0.97 and it is stable over a wide temperature range. $BaCeO_3$, on the other hand, has a tolerance factor of ~0.89, and is unstable at low temperatures [31], producing a structural transition. Obviously a tolerance factor equal to 1 is merely an ideal case. Distorted perovskite structures can occur when the tolerance factor is far from unity. In particular we can consider two possible cases:

1. $r_{A-X} > \sqrt{2} \cdot r_{M-X}$ (tolerance factor > 1) there is a tendency to distort towards a tetragonal elongation;

2. $r_{A-X} < \sqrt{2} \cdot r_{M-X}$ (tolerance factor < 1) there is a tendency to distort towards buckling of octahedra.

More generally, the structure can be distorted as a result of cation displacements, as in $BaTiO_3$ [32] or $PbTiO_3$ (**Figure 1.9 (b)**) or by tilting of the octahedra as in $CaTiO_3$ (**Figure 1.9 (a)**) [33]. In the first case the cation displacement, due to steoreochemically active pairs of A cations, gives rise to the useful properties of ferroelectricity and antiferroelectricity of many perovskite systems. Some example of undistorted cubic perovskite are $SrTiO_3$ (t =1.00) [34] and $CsSnBr_3$ (t =0.98) [35].

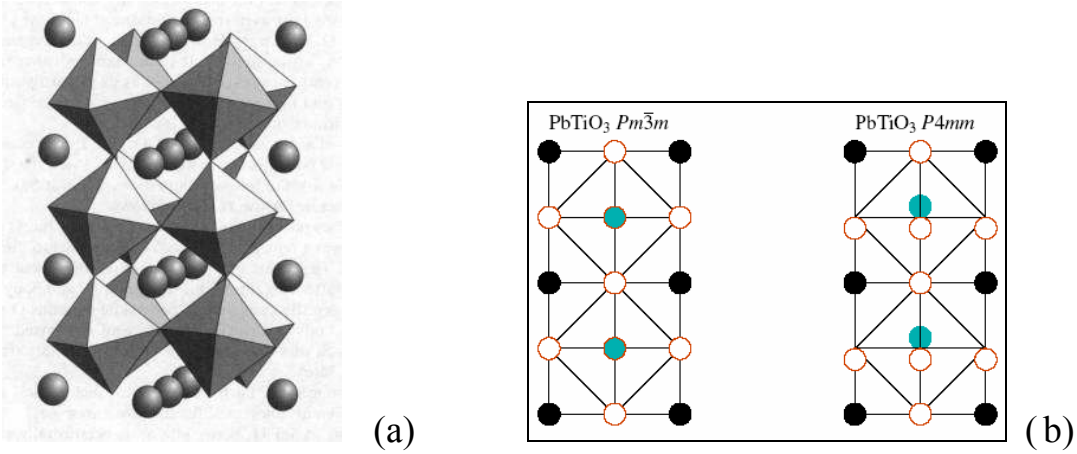

Figure 1.9 – (a) *Distortion structure of $CaTiO_3$ compound where octahedra are tilted.*. (b) *In the particular case of $PbTiO_3$, the phase transition from the cubic, paraelectric phase to the tetragonal ferroelectric phase (a displacive phase transition) is associated with the freezing of a phonon associated with the Ti atom in the center of the octahedron.*

In addition to the 3D perovskites, layered perovskites can also be formed by taking an n-layer-thick cut from 3D perovskite structure along some crystallographic directions as <100>, <110>, and <111>. Particular attention has been given, in the past, to the <100> type structure. In this class, the Ruddlesden-Popper series [36], $A_{n+1}M_nX_{3n+1}$ (**Figure 1.10 (a)**), and the Aurivillium oxide family [37], $(Bi_2O_2)A_{n-1}M_nO_{3n+1}$, (**Figure 1.10 (b)**) deserve to be specially mentioned. The Aurivillium family possess interesting ferroelectric properties with potential for use in nonvolatile random access memory devices [38]. An example of Ruddlesden-Popper compound, instead, is the system $Sr_{2-x}Ln_{1+x}Mn_2O_7$ (Ln = Lantanides) which exhibits the giant magnetoresistence effect [39]. High temperature superconductivity (HTS) appears in members of both these families, the most popular being $La_{2-x}Sr_xCuO_4$ or $Bi_2Sr_2CaCu_2O_{8+\delta}$.

All these complex layered structures consist of an active layer, as the CuO_2 layer in HTS superconductors, separated electronically and mechanically by “soft modulation

layers" [19]. "Soft" because these layers contain ions that do not have an essential physical role, they are less tightly bonded and can be substituted with ions in a different valence state without any relevant change of the structure of the compounds.

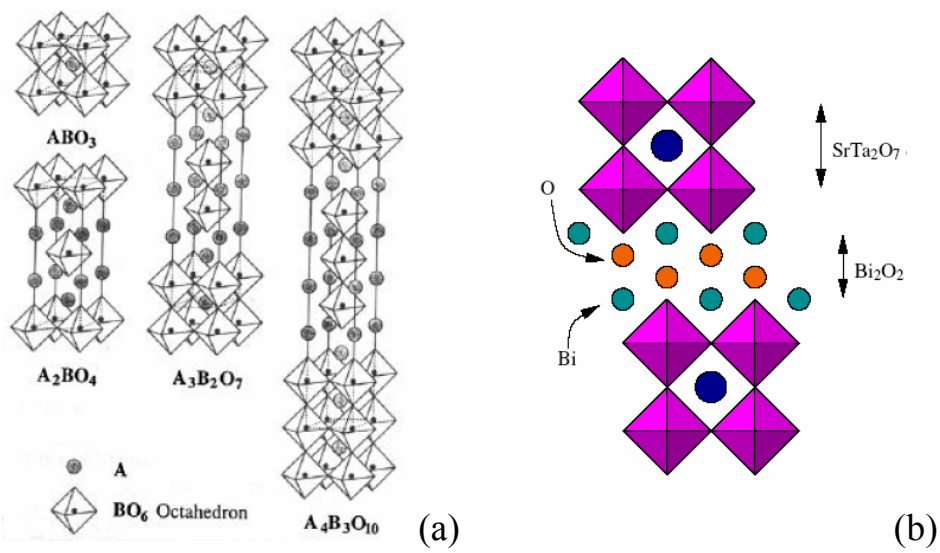

Figure 1.10 – *Representation of structures of (a) Ruddlesden-Popper oxide series with n=1,2,3 and (b) $(Bi_2O_2)SrTa_2O_7$ a n=2 compound of Aurivillium family.*

Starting from this background, Mitzi and IBM coworkers [20] have proposed the idea to spouse the perovskite structural variety and electron correlation properties with the properties of organic molecules as polymerization, polarizability and luminescent character in a single compound "*replacing the inorganic modulation layer with an organic layer*" [19].

1.4.b Organic molecules and the carbon chemistry

Organic molecules are classified as: alcohols, aldehides, amides, amines, carboxylic acid, ketones, esters, ethers, and anhydrides, but all the molecules of these classes are composed basically by four atoms: nitrogen, hydrogen, oxygen and carbon. From simple oligomers to polymers all the organics are composed by these atoms. In some cases, metals

and halogens are incorporated in the molecule with the function of intrinsic dopant, but carbon and its "chemistry" has the most important and basic role.

The carbon atom has six electrons occupying the atomic orbitals, as reported in **Table 1.1**.

Orbital:	**1s**	**2s**	**$2p_x$**	**$2p_y$**	**$2p_z$**
Valence 2	2	2	1	1	0
Valence 4	2	1	1	1	1

Table 1.1 – *Electronic configurations of carbon.*

It should form two bonds to add two electrons to complete the vacancies in the two incomplete p orbitals (p_x and p_y): in this case it is divalent (form 2 single bonds). In reality, the more stable configuration for carbon is the tetravalent one. In this case carbon forms four bonds. This is possible because in carbon (as in some other atoms), chemical bonding proceeds via intermediate steps: *Promotion* and *Hybridization***.** For hybridization, carbon 'promotes' one 2s electron into the empty p_z orbital and then it combines ('hybridizes') the remaining one with either p orbitals:

I. three 2p orbitals → sp^3 hybrids: *sp^3 hybridization* show a fully symmetric orbital configuration (tetrahedron) and C can form 4 σ bonds (e.g. methane CH_4, ethane $H_3C\text{-}CH_3$, single carbon-carbon bond (**Figure 1.11 (a)**)). Diamond consists of carbon atoms held together by σ bonds entirely and it is a large gap insulator;
II. two 2p orbitals → sp^2 hybrids: *sp^2 hybridization* produce 3 sp^2 hybrid orbitals in a plane and the remaining p orbital perpendicular to the plane. In this form, C bond with another sp^2 hybrid C to form a double carbon-carbon bond, (e.g. $H_2C{=}CH_2$ ethylene (**Figure 1.11 (b)**) or benzene C_6H_6) one σ-type and the other, from p orbitals overlap, to form the so-called *π bond*. This is a weaker bond, and the respective orbital is more '*delocalized*', i.e. occupies relatively large space rather far away from its original carbon. Graphite consists of sp^2 carbon atoms held together by σ and π bonds and it is a conductor;
III. one 2p orbital → sp hybrid: *sp hybridization* show two orthogonal p orbitals in yz plane and other two sp hybrid orbitals along the x axis. In this form, C can bond

with another sp hybrid C to form a triple bond (e.g. HC≡CH acetylene in **Figure 1.11 (c)**), one σ-type and two π-type.

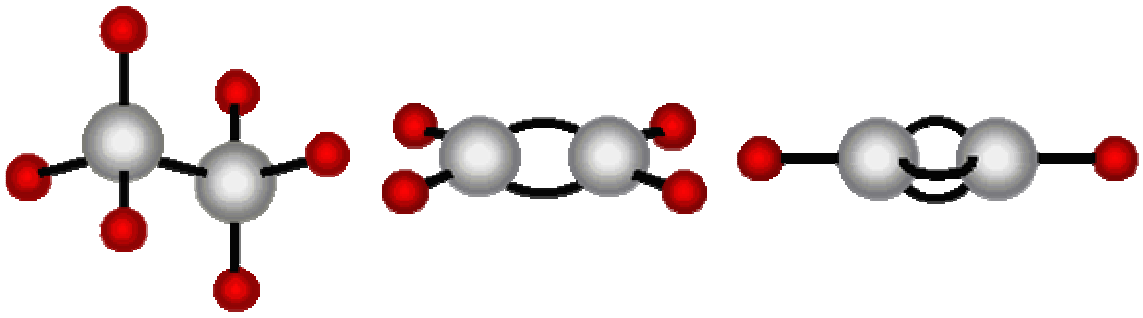

Figure 1.11 – *Ball stick representation of* (a) *single carbon-carbon bond in ethane (C_2H_6),* (b) *double carbon-carbon bond in* ethylene (C_2H_4), and (c) *triple carbon-carbon bond in acetylene (C_2H_2). In gray are carbon atoms and in red are hydrogen atoms, black stick are the bonds.*

In organic chemistry, a particular role is carried out by delocalized π bonds. Much of molecular physics, including organic semiconductor physics, is concerned with molecules containing sp^2 carbon rings and chains. These delocalized π electrons have remarkable properties with respect to their interaction with light and they have a crucial role in the charge transfer mechanism between donor and acceptor molecules. These molecules, characterized by delocalized π molecular orbital as a consequence of alternating single/double or single/triple carbon bonds, are the well known *conjugated* molecules (**Figure 1.12**). Conjugated molecules, generally, have semiconductive character. For polymers, it can be assumed that the states are close enough to be described by a band-structure. This assumption is not fully correct, but gives relatively accurate results. For oligomers this assumption cannot be valid, because they have distinct energy levels. In any case, the energy levels near the Fermi energy are described in terms of "conduction" and "valence" bands.

The levels that are similar to the valence band are defined as **H**ighest **O**ccupied **M**olecular **O**rbital (HOMO), and the ones similar to the conduction band as **L**owest **U**noccupied **M**olecular **O**rbital (LUMO). The levels below the HOMO are described as HOMO-1, HOMO-2, HOMO-3, etc. The levels above the LUMO are described as

LUMO+1, LUMO+2, etc. Note that a half-filled HOMO would imply an unpaired spin, i.e. the molecule would be a *radical* (*excited state*).

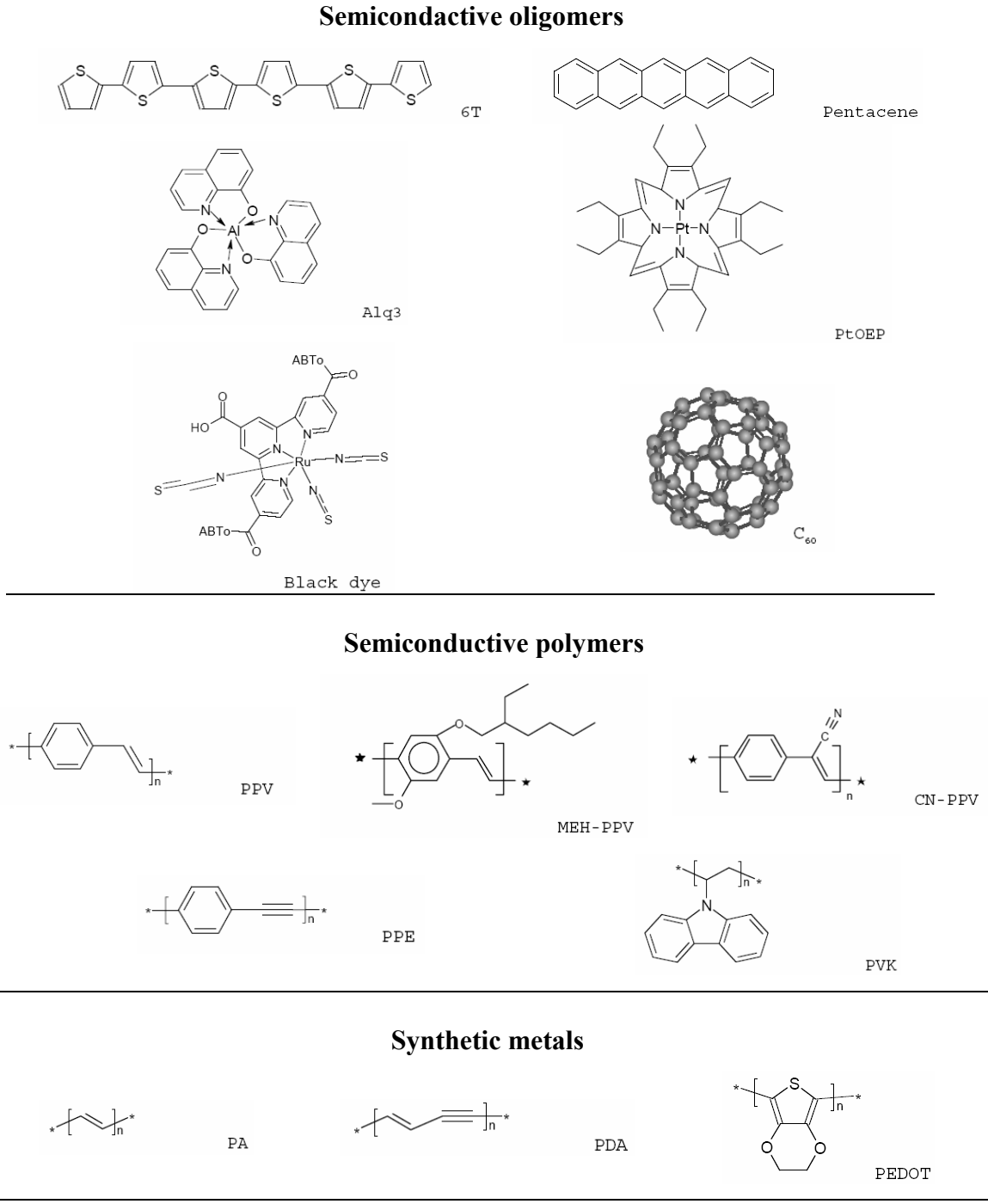

Figure 1.12 – *Foremost oligomers, polymers and synthetic metals used in electronics technologies. In semiconductive oligomers section, linear chain to three dimensional molecules are proposed. For synthetic metals it is shown only the polymeric units that have semiconductive character. The metallic character is related to the presence of a dopant (e.g. for PEDOT is typically used PSS molecule called ionomers).*

Because of this analogy the energy difference between LUMO and HOMO in a conjugated molecule is often called the *bandgap*. However, we will soon address the limits of the analogy between inorganic and organic semiconductors. There is also some ambiguity in giving a quantitative figure for an organic bandgap from experimental data. As an example the semiconductive distinction between direct and indirect bandgap makes no sense when k is not a good quantum number.

Beyond the single molecule electronic properties, it is needed for applications to consider the electronic transport properties of the molecular aggregates. The dominant interaction in a molecular aggregate are the weak interactions, as hydrogen type bonds and van der Waals interactions. These types of intermolecular bonds guarantee solubility and mechanical flexibility, but also thermal instability and reactivity with the external ambient (especially oxygen) that strongly limit the hole/electron transport. In molecular aggregates, in fact, charge transport is related to some non-conventional mechanisms (compared to the classical scheme of inorganic crystal semiconductors) such as donor-acceptor charge transfer, formation and propagation dynamics of interchain and intrachain polarons (**Figure 1.13**) [[40,41]], and protonic conduction.

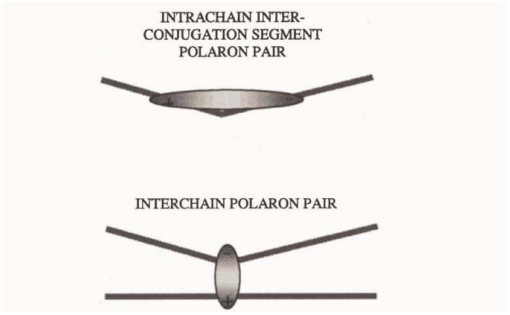

Figure 1.13 – *Schematic representation of intrachain and interchain polaron pairing.*

1.4.c Organic-inorganic perovskite: structures and properties

Since the first discovery of organic–inorganic perovskites over 100 years ago [[42]], hundreds of related structures have been reported and will be presented in this paragraph. Through the characterization of a sufficient number of compounds within a particular structural class, empirical rules can often be generated to aid in the design and control of

the structures and to get some understanding and guidelines for the construction of the hybrids. Organic molecules or polymers and inorganic perovskites can be bundled by different type of bonds. There are numerous reported compound with covalent bonding between organic and inorganic units as $C_nH_{2n+1}BiI_2$ [43]. This compound consists of extended BiI_2 chains with the alkyl groups bonded to one side of each chain. At present, this class of extended organometallic and other covalently interacting compounds, generally containing simple organic radicals, is somewhat limited. The degree of interaction between organic and inorganic species in van der Waals interacting system is relatively small. To have potentially useful physical properties, ionic interacting hybrid compounds have to be considered. In particular an increasing number of new structures have been initially reported in the perovskite hybrid class by Mitzi [19]. In particular in this class of materials the organic component is R-ammonium molecule connected to the anion in the inorganic perovskite through hydrogen/ionic bonds. Typically, halogen atoms are used as anions whereas oxide based compounds are much less studied. Some examples are $(C_nH_{2n+1}NH_3)_2Ti_4O_9$ [44] and $(H_3NC_2H_4NH_3)W_3O_{10}$ [45].

In this class of perovskite hybrid materials it is also possible to observe low dimensionality properties. In fact one can modulate dimensionality from 3D inorganic environment in which there are isolated molecules [46,47], to zero dimensionality ,where, inside a molecular matrix, inorganic clusters of nanometric dimension (quantum dots) are localized [48]. All the intermediate configurations (2D and 1D) are also possible [49,50].

Tree-dimensional systems consist of a cubic AMX_3 perovskite structure (see **Figure 1.8**) where the "A" cation is a ionic molecule (e.g. methylammonium). Obviously the choice of the organic cation is limited because of the restricted dimension of the cuboctahedral hole formed by the 12 nearest-neighbor X atoms. Based on this considerations, a methylammonium cation $CH_3NH_3^+$ (C–N length bond is 1.4 Å) or a formamidium cation $NH_2{=}CHNH_3^+$ are expected to be an appropriate choice for the 3D perovskite structure. In fact, the compounds $CH_3NH_3MX_3$ with M=Sn, Pb and X=Cl, Br, and I, have been successfully synthesized [46,47,51,52,53,54]. Each of these systems have a cubic structure, as the highest temperature phase. At high temperatures the organic cation shows orientational disorder. At lower temperatures the cubic phase, due to a tolerance factor smaller then unity, results to be unstable, leading to a structural transition. In fact, upon cooling, the structure distorts lowering its symmetry since the motion of the

methylammonium cation has more restrictions. This is confirmed by NMR (Nuclear Magnetic Resonance) and NQR (Nuclear Quadrupolar Resonance) measurements [47,55]. Therefore at higher temperature phase until performing cubic phase.

Two-dimensional systems are layered compounds where the organic layers and the inorganic ones alternate in the structure. The basic layered perovskite series structures [19], are schematically reported in **Figure 1.14,** together with the general chemical formula. The inorganic layer consists in a 2D network of corner-sharing metal halides (or oxides) octahedra in which the M cation must be a divalent atom to fit the charge requirements, that can adopt an octahedral coordination (transition metals and group IVA atoms). For certain systems a mixture of trivalent (M^{3+}) cations and vacancies can occupy the metal site, yielding to $M_{2/3}X_4^{2-}$ layers [56].

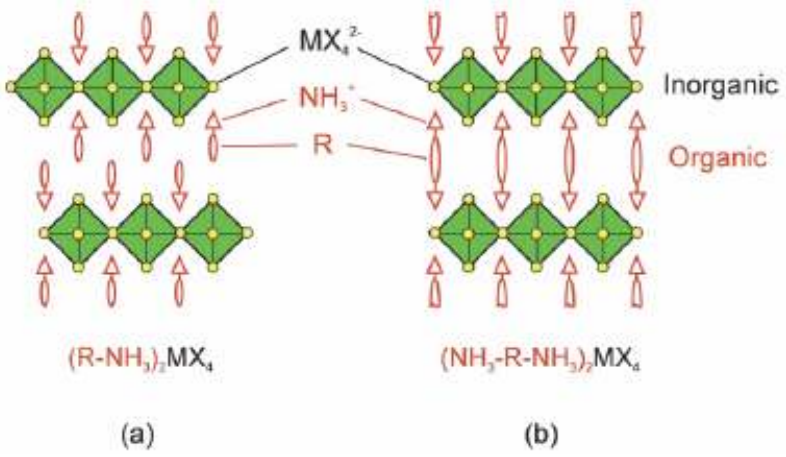

Figure 1.14 – *Schematic representation of single-layer (n = 1) <100> oriented perovskites called "staggered" configuration with* (a) *monoammonium* $(R\text{-}NH_3)_2MX_4$ *or* (b) *diammonium* $(NH_3\text{-}R\text{-}NH_3)MX_4$ *organic cations called "eclipsed" configuration* [57].

The organic layers consist of mono-ammonium ($R\text{-}NH_3$) or di-ammonium ($NH_3\text{-}R\text{-}NH_3$) molecules sheets where R is an organic radical. In monoammonium compounds two ammonium molecules bond ionically with the anion in the two perovskite layers, while the organic molecule is situated in a tail-to-tail arrangement with van der Waals interactions. This type of configuration generates a shift of the perovskite sheet in respect to the following one and is named *staggered*. In the case of diammonium organic cations, the single molecule can be bond with two adjacent perovskite layers, removing the van der Waals gap and the shift between the layers. This configuration is called *eclipsed*. The

inorganic layers are referred to as "perovskite sheets" because they have a great analogy with the inorganic layered perovskites (as the Ruddlesden-Popper series) and they are conceptually derivable from the three dimensional AMX_3 perovskite structure by taking a one-layer-thick cut along a crystallographic direction, as showed in **Figure 1.15**.

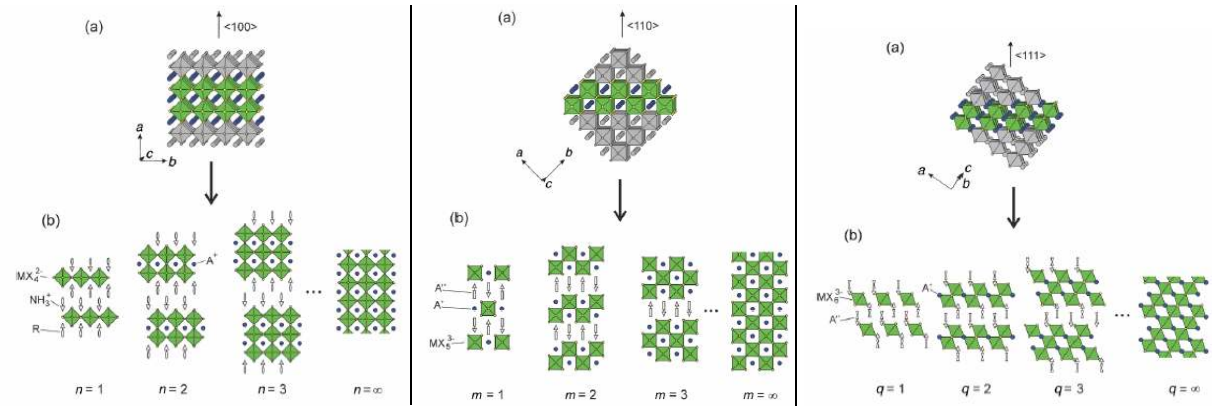

Figure 1.15 – On the left side: *family of intergrowth compounds formed from the parent AMX_3 (3D) and $(R\text{-}NH_3)_2MX_4$ (2D) perovskites. The <100> oriented layered perovskite series, $(R\text{-}NH_3)_2A_{n-1}M_nX_{3n-1}$, can also conceptually be derived by* (a) *taking n layers from along the <100> direction of the 3D perovskite structure and* (b) *alternating these layers with bilayers of organic cations.* In the center: *schematic representation of the <110> oriented family of layered hybrid perovskites, $A'_2A_mM_mX_{3m-2}$. The layered perovskite framework is derived from the 3D perovskite parent compound by* (a) *taking m layers from along the <110> direction of the 3D structure and* (b) *alternately stacking these layers with organic cations. Note that the specific choice of organic cations, A', can determine whether the <100> or <110> oriented perovskite family will form. One member of the <110> oriented family has $A' = NH_2C(I)=NH_2$, $A = CH_3NH_3$, $M = Sn^{2-}$, and $X = I^-$.* On the right side: *Schematic representation of the <111>-oriented family of layered hybrid perovskites, $A'_2A_{q-1}M_qX_{3q-3}$. The layered perovskite framework is derived from the 3D perovskite parent compound by* (a) *taking q layers from along the <111> direction of the 3D structure and* (b) *alternately stacking these layers with organic cations* [57].

Starting from this consideration, in addition to the single-layers perovskite sheets of **Figure 1.14 (a)**, the structures can also be conveniently synthesized with multiple <100>, <110> and <111> oriented sheets [58,59] enabling control over the dimensionality of the inorganic framework.

The choice of the hydrogen bonding scheme is important for determining the orientation and conformation of the organic molecule within the layered hybrid ammonium based structure. In principle, the ammonium "heads" of the organic cations can hydrogen bond to any of the eight halides within the holes formed by the corner-sharing MX_6 octahedra (**Figure 1.16**). In practice, due to the geometric constraints of the ammonium group and

the organic tail, the N–H---X interactions generally form either two bridging halides and one terminal halide ("bridging halide configuration") or two terminal halides and one bridging halide ("terminal halide configuration"). Note that some MX_4^{2-} frameworks are more flexible than others. In the copper(II) halide systems, as an example, the Jahn–Teller distortion of the CuX_6 octahedra enables a larger degree of flexibility in the hydrogen bonding between the organic cation and the inorganic sheets.

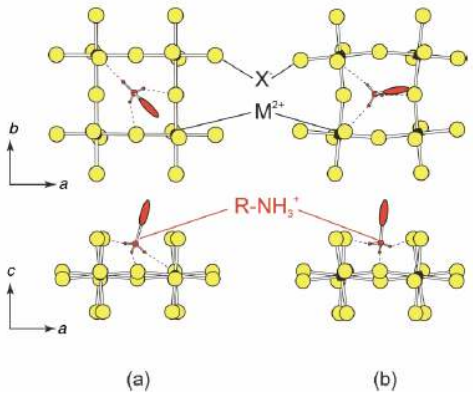

Figure 1.16 – *Two hydrogen-bonding schemes typically observed in the $(RNH_3)_2MX_4$ and $(NH_3RNH_3)MX_4$ type structures:* (a) *the bridging halide configuration and* (b) *the terminal halide configuration* [19].

These 2D layered materials can be assimilated to the artificial hetero-multilayer structures [60,61], an important class of conventional (inorganic semiconductive LED) and non conventional ($CuPc/TiO_x$ [26]) devices. Semiconductive inorganic sheets alternating with organic layers with a relatively large HOMO-LUMO energy gap can produce an energy structure analogous to multilayer quantum well structures. This is illustrated in **Figure 1.17**. The greatest advantage of these materials in respect to artificial multilayers is that these self-assembled hybrids have the same properties of artificial structure without the problem of interface roughness. Changing the inorganic perovskite composition or the number of sheets between two organic layers or changing the organic radical (e.g. introducing more complex conjugated molecules), it is possible to tune the energy band arrangement (**Figure 1.17**) and consequently the optical properties.

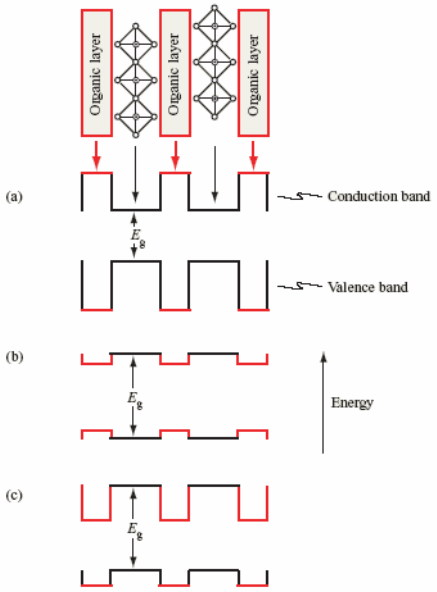

Figure 1.17 – *Schematic organic–inorganic perovskite structure and several possible energy-level schemes that can arise within these structures. The most common arrangement is shown in* (a), *where semiconducting inorganic sheets alternate with organic layers having much wider bandgaps, resulting in a type I quantum well structure. In* (b), *wider bandgap inorganic layers and organic cations with a smaller HOMO–LUMO gap result in the well/barrier roles of the organic and inorganic layers being switched. In* (c), *by shifting the electron affinity of the organic layers relative to the inorganic layers, a staggering of the energy levels leads to a type II quantum well structure* [20].

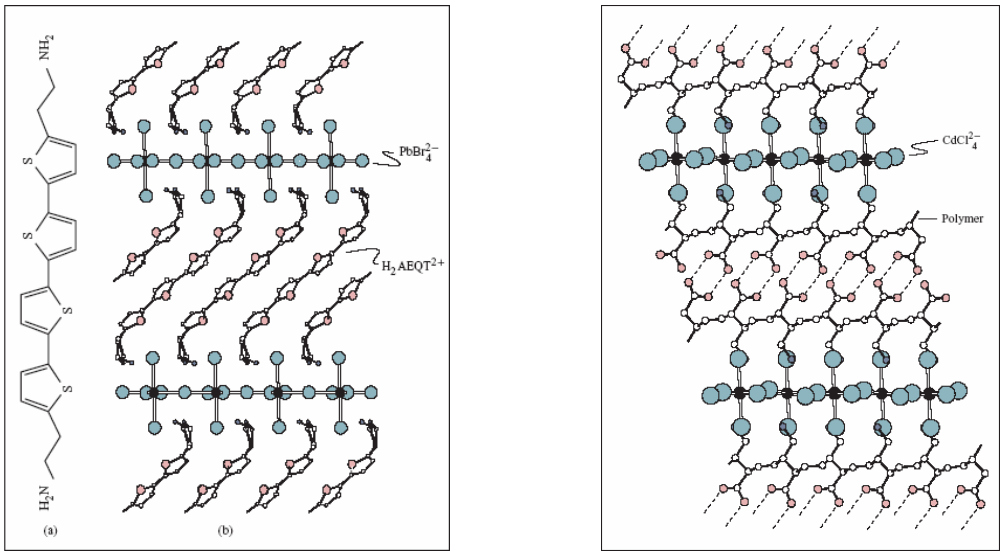

Figure 1.18 – *On the left: crystal structure of $(H_2AEQT)PbBr_4$, viewed down the b axis* [62]. *The compound crystallizes in a monoclinic subcell (C2/c space group). On the right: crystal structure of the polymerized product formed by subjecting $(HO_2CCH=CHCH=CHCH_2NH_3)_2CdCl_4$ to UV or γ irradiation* [63]. *Polymerization yields ordered 1,4-disubstituted trans-polybutadiene $[–CH(CO_2H)CH=CHCH(CH_2NH_2)–]_\infty$. Hydrogen bonding between CO_2H groups on adjacent layers is shown by dashed lines and helps to stabilize the structure.*

In the literature generally simple organic cations, as the alkyl chain, are bonded to the ammonium head. More complex cations can be chosen as organic components without renouncing to ammonium and its bonding role between the organic and inorganic

components (**Figure 1.18 (a)**). An interesting feature of the oligomeric or dye containing organic-inorganic perovskites is the fact that the orientation of the organic cation can be controlled properly designing the inorganic framework in respect to the ammonium head and the organic radical dimensions [19].

Another interesting possibility for the organic layer is the incorporation of an organic cation with one or more double or triple bonds [64]. In a suitably designed system, the inorganic perovskite sheet functions as a template, holding the organic molecules in a favorable orientation for a successive photo-polymerization process. An example is given by $(HO_2CCH{=}CHCH{=}CHCH_2NH_3)_2CdCl_4$, as reported in **Figure 1.18 (b)**. In a similar copper(II) chloride compound the same polymerization reaction does not occur because of the structural difference in the inorganic framework, induced by the Jahn-Teller distortion, that leads to an unfavorable configuration to obtain polymerization of the monomer within the organic layer [63].

2D systems, if composed of magnetic metallic cations as Mn or Cu, can be considered as quasi two dimensional Heisemberg antiferromagnets [65] and can act as the building blocks for magnetic nanocomposite materials incorporating these hybrid compounds in a polymeric matrix [24].

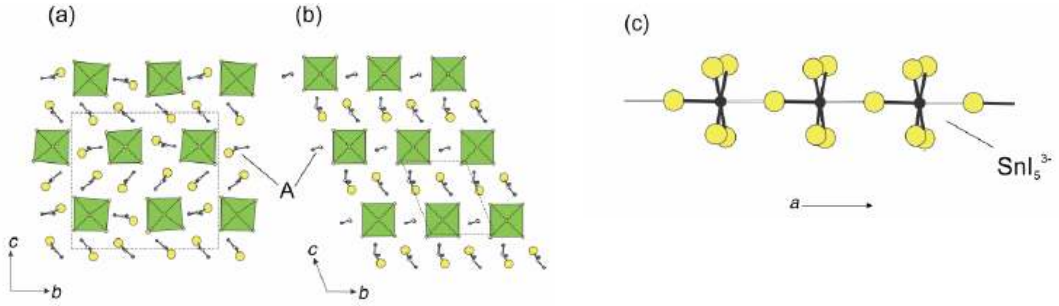

Figure 1.19 – *Comparison of two m = 1 structures, $[NH_2C(I){=}NH_2]_2ASnI_5$, viewed down the a axis (i.e. parallel to the SnI_5^{3-} chains)* [66]. *The A = iodoformamidinium structure* (a) *crystallizes in a monoclinic (P21/c) cell with a=6.4394(4), b= 20.069(2), c=18.722(1) Å, and β = 92.822(6). The corresponding material with A = formamidinium* (b) *adopts a triclinic cell with the lattice constants a = 6.3635(3), b=8.8737(5), c=10.8782(6) Å, α =111.616(5), β=92.938(4), and γ=95.358(4). In* (c) *the SnI_5^{3-} chain structure for the A = iodoformamidinium compound is shown extending along the a axis. The shorter Sn–I bonds are drawn as filled (or black), whereas the longer 3.484(1) Å Sn–I bonds are drawn as narrower and unfilled.*

An interesting feature of <110> oriented layered perovskites is that, for *m* =1, the structure reduces to a **one-dimensional system**, an array of perovskite chains that opens

the possibility of examining the structural and physical properties of a 1D extended network of corner-sharing MX_6 octahedra. Examples are $[NH_2C(I)=NH_2]_2ASnI_5$ where A = iodoformamidinium or formamidium (**Figure 1.19**) [66] and $[NH_2C(I)=NH_2]_3PbI_5$ [49] in which a strong one-dimensional Frenkel exciton has been observed.

Zero-dimensional systems, in analogy to the 3D, 2D, 1D arrays of corner-sharing MX_6 octahedra, can also be considered. This type of system consists in isolated octahedra in a molecular matrix. In particular, they can be seen as <111> oriented layered perovskites. In these type of systems, in fact, for q =1 the structure reduces to a zero-dimensional system. Some examples are the hydrated compound $(CH_3NH_3)_4PbI_6{\cdot}2H_2O$ [48], which consist of isolated PbI_6^{4-}, $CH_3NH_3^+$ and H_2O molecules, and $(C_4H_9NH_3)_2SnI_6$ [67] and $[(CH_3)_2NH_2]SnCl_6$ [68] (**Figure 1.20**) anhydrous compounds.

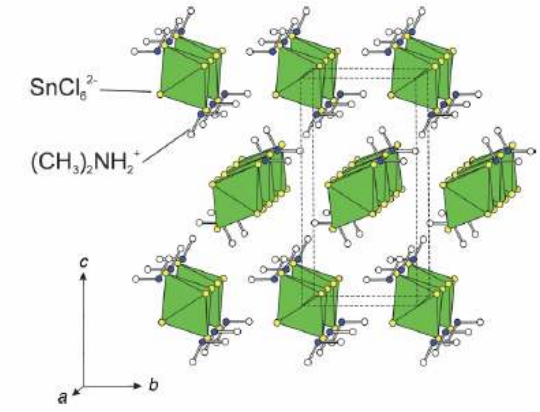

Figure 1.20 – *Crystal structure of the q = 1 <111> oriented system $[(CH_3)_2NH_2]SnCl_6$, viewed approximately down the a axis* [68]. *The structure adopts an orthorhombic (Pmnn) unit cell with the lattice parameters a = 7.220(1), b = 7.340(2), c = 14.446(3) Å.*

In conclusion, varying the organic and inorganic components and the stoichiometric ratio between them, it is possible to modulate the system dimensionality and electronic, magnetic and/or optical properties. An important step towards the technological application of these materials was taken in 2003 by Cheng et al. [69]. They proved the possibility to utilize soft lithographic techniques (MIMIC Micro Modulation In Capillaries), typically for organics, on the photoluminescent $(C_6H_5C_2H_4NH_3)_2PbI_4$ hybrid. Moreover, the presence of weak bonds in the proposed structures, guarantees flexibility and malleability that could allow the deposition of thin films on flexible substrates [70].

1.5 Selected materials:

In the proceeding of this thesis work, the attention will be focused on two series of hybrid compounds:

– **$(C_nH_{2n+1}NH_3)_2CuCl_4$** where ***n*** **=1,…,4** (**Figure 1.21**);

– **$CH_3NH_3SnX_3$** where **X =Cl and Br** (**Figure 1.22**).

These compounds belong to the classes discussed in the previous paragraph, where the alkylammonium chains are the organic components. The bonding between organic and inorganic components is realized by an ordinary ammine group ($–NH_3^+$) that realizes an hydrogen/ionic bond with the halogen atoms. Alkyl chains ($CH_3C_{(n-1)}H_{2(n-1)}–$) are simple organic cations composed by a number *n* of carbon atoms that are tied together by single bonds forming a zig-zag chain. The zig-zag spatial configuration of the carbon atoms is due to the sp^3 hybridization of carbon orbitals that produces a tetrahedral bond configuration. These covalent sigma bonds will energetically separate the HOMO and LUMO levels of the molecule very strongly, and all the electrons will sit in the bonding states.

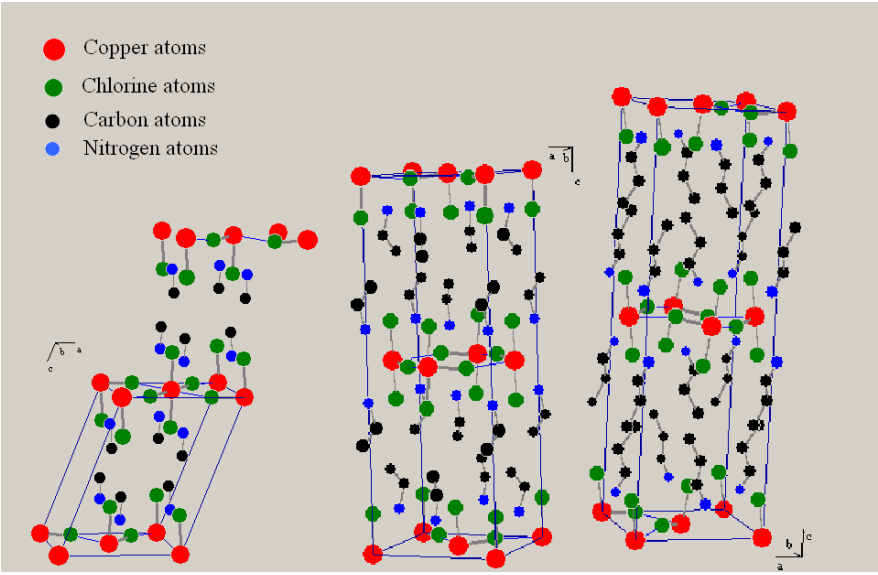

Figure 1.21 – *Representation of unit cell of layered $(C_nH_{2n+1}NH_3)_2CuCl_4$ from left to right: n =1 monoclinic cell of methyl-ammonium copper(II) tetrachloride; n =2 and 3 of orthorhombic del of ethyl-ammonium copper(II) tetrachloride and of propil-ammonium copper(II) tetrachloride.*

The choice of these two class of compound is related to the interesting electrical, magnetic and optical properties of relative isostructural compounds reported in literature.

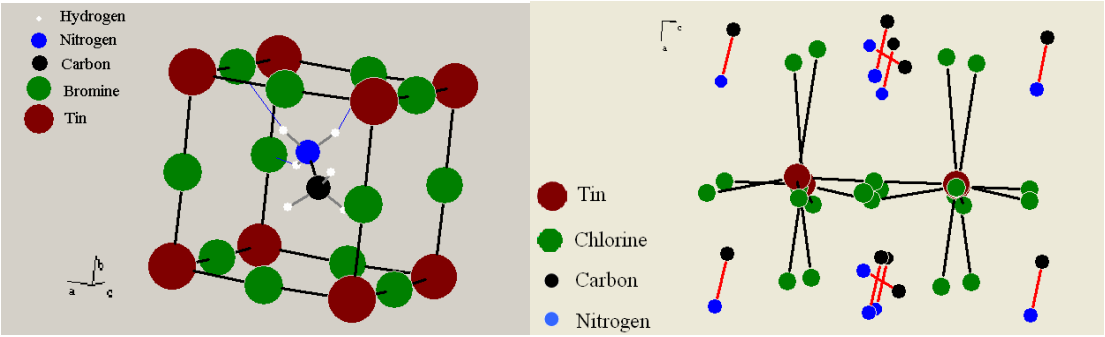

Figure 1.22 – *On the left side: the stick and ball picture of unit cell of $CH_3NH_3SnBr_3$ is shown as resulting from ab-initio calculations* [71]. *$CH_3NH_3^+$ cation (positioned along [111] direction in the figure) is free to rotate at room temperature.$CH_3NH_3SnBr_3$. On the right side:it is shown distorted triclinic pseudocubic cell of $CH_3NH_3SnCl_3$ compound* [76].

Crystal structures of these compounds are known by studies on powders and single crystals [72,73,74,75]. The 2D layered $(C_nH_{2n+1}NH_3)_2CuCl_4$ series literature data, indicate that the compounds with n>1 are orthorhombic, while the n =1 hybrid is better refined in the monoclinic system (monoclinic angle β=110.89). The 3D $CH_3NH_3SnX_3$ compound are referred in the literature as being cubic or pseudo-cubic at room temperature [76,77].

Compound	Cell symmetry (room temp.)	a (Å)	b (Å)	c (Å)
$(CH_3NH_3)_2CuCl_4$ [72]	*P*21/a monoclinic β=110.89°	7.268	7.367	9.971
$(C_2H_5NH_3)_2CuCl_4$ [73]	*P*cab orthorhombic	7.47	7.35	21.18
$(C_3H_7NH_3)_2CuCl_4$ [74]	*P*cab orthorhombic	7.33	7.65	24.66
$(C_4H_9NH_3)_2CuCl_4$ [75]	*P*cab orthorhombic	7.33	7.45	30.75
$CH_3NH_3SnCl_3$ [76]	*P*1 triclinic α=90.40° β=93.08° γ=90.15°	5.726	8.227	7.910
$CH_3NH_3SnBr_3$ [77]	*P*m3m cubic	5.89	5.89	5.89

Table 1.2 – *Summarizing of room temperature structural parameters of $(C_nH_{2n+1}NH_3)_2CuCl_4$ and $CH_3NH_3SnX_3$ series.*

In this thesis work, films of these materials have been realized by single source thermal ablation deposition technique.

Bibliography

[1] J. M. Show, and P. F. Seidler, *IBM J. Res. & Dev.*, **45**, 3 (2001).

[2] G. H. Gerlinck, H. E. A. Huitema, E. van Veenendaal, E. Cantatore, L. Schrijnemakers, J. B. P. H. van der Putten, T. C. T. Geuns, M. Beenhakkers, J. B. Giesberg, B. H. Huisman, E. J. Meijer, E. M. Benito, F. J. Touwslager, A. W. Marsman, B. J. E. van Rens, and D. M. De Leeuw, *Nature Materials*, **3**, 106 (2004).

[3] I. Mcculloch. *Nature Materials*, **4**, 583 (2005).

[4] N. F. Mott, "*Metal-Insulator Transitino"*, London : Taylor & Francis (1974).

[5] H. Shirakawa, E. J. Louis, A. G. MacDiarmid, C. K. Chiang, and A. J. Heeger, *Chem. Comm.*, **13**, 578 (1977).

[6] C. D. Dimitrakopoulos, A. R. Brown, and A. Pomp, *J. Appl. Phys.*, **80,** 2501 (1996).

[7] B. J. F. Bruet, H. J. Qi, M. C. Boyce, R. Panas, K. Tai, L. Frick, and C. Ortiz, *J. Mater. Res.*, **20**, 2400 (2005).

[8] E. P. Giannelis, *Adv. Mater.*, **8**, 29 (1996).

[9] S. S. Ray, and M. Okamoto, *REV. ART. Progr. Polym. Sci.*, **28**, 1539-1641 (2003); S. S. Ray, and M. Bousmina, *REV. ART. Progr. Mater. Sci.*, **50**, 962-1079 (2005).

[10] M. Zanetti, T. Kashiwagi, L. Falqui, G. Camino, *Chem. Mater.*, **14**, 881, (2002).

[11] J. Takada, H. Awaji, M. Koshioka, and W. A. Nevin, *Appl. Phys. Lett.*, **61**, 2184 (1992).

[12] S. Tokito, J. Sakata, and Y. Taga, *Appl. Phys. Lett.*, **64**, 1353 (1994).

[13] W. A. Little, *Phys. Rev.*, **134**, A1416 (1964).

[14] K. Beekgard, K. Carneiro, M. Olsen, and F. B. Rasmussen, *Phys. Rev. Lett.*, **46**, 852 (1980)

[15] H. Urayama, H. Yamochi, G. Saito, K. Nozawa, M. Kinoshita, S. Sato, K. Oshima, A. Kawamoto, and J. Tanaka, *Chem. Lett.*, **55** (1988).

[16] J. H. Schön, H. Merg, and Z. Bao, *Nature*, **413**, 713 (2001).

[17] C. M. Drain, *Proceedings of the National Academy of Sciences*, **99**, 5178 (2002).

[18] V. Balzani, A. Credi, and M. Venturi, *Proceedings of the National Academy of Sciences*, **99**, 4814 (2002).

[19] David B. Mitzi, *Progress in Inorganic Chemistry*, Vol **48**, Ed. by K. D. Karlin, Jonh Wiley & Sons, Inc. (1999).

[20] D. B. Mitzi, K. Chondroudis and C. R. Kagan, *IBM J. Res. & Dev.*, **45**, N°1 (2001).

[21] D.B. Mitzi, *Chem. Mater.*, **13**, 3283 (2001).

[22] R. Valiente, and F. Rodriguez, *Phys. Rev. B*, **60**, 9423 (1999).

[23] M. C. Marco de Luca, F. Rodriguez, and J. A. Aramburu, *J. Phys.: Condens. Mater*, **3**, 8945 (1991).

[24] E. Wortham, A. Zorko, D. Arcon, and A. Lappas, *Physica B*, **318**, 387 (2002).

[25] P. Zhou, J. E. Drumheller, B. Patyal, and R. D. Willet, *Phys. Rev. B*, **45**, 12365 (1992).

[26] X. Hong, T. Ishihara, and A. V. Nurmikko, *Phys. Rev. B*, **45**, 6961 (1992).

[27] M. Era, S. Morimoto, T. Tsutsui, and S. Saito, *Appl. Phys. Lett.*, **65**, 676 (1994).

[28] C. R. Kagan, D. B. Mitzi, and C. D. Dimitrakopoulos, *Science*, **286**, 945 (1999).

[29] F. S. Galasso, S*tructure, Properties and Preparation of Perovskite–Type Compounds*, Pergamon, New York, p. 4 (1969).

[30] A. Navrotsky, *"Perovskite: A structure of Great Interest to Geophysics and Materials Science"*, *Geophysics Monograph* **45**, ed. by A. Navrotsky and D. J. Weinder, a publication of the American Geophysical Union, Washington, D. C., (1989).

[31] S. Gopalan, and A. V. Virkar, *J. Electrochem. Soc.*, **140**, 1060 (1993).

[32] G. Shirane, H. Danner, and R. Pepinshi, *Phys. Rev.*, **105**, 856 (1957).

[33] A. M. Blazer, *Acta Crystallogr., Sect B*, **28**, 3384 (1972).

[34] R. W. G. Wyckoff, *Crystall Structures*, Vol **2**, Wiley, New York, p. 394 (1964).

[35] D. E. Scaife, P. F. Weller, and W. G. Fisher, *J. Solid State Chem.*, **9**, 308 (1974).

[36] S. N. Ruddlesden, and P.Popper, *Acta Crystallogr.*, **11**, 54 (1958); S. N. Ruddlesden, and P.Popper, *Acta Crystallogr.*, **10**, 538 (1957).

[37] B. Aurivillium, *Ark. Kemi.*, **1**, 463 (1949); B. Aurivillium, *Ark. Kemi.*, **1**, 499 (1949); B. Aurivillium, *Ark. Kemi.*, **2**, 519(1950).

[38] Y. Moritomo, A. Asamitsu, H. Kuwahara, and Y. Tokura, *Nature*, **380**, 141 (1996).

[39] A. A.-Paz de Araujo, J. D. Cuchiaro, L. D. McMillan, M. C. Scott, and J. F. Scott, *Nature*, **374**, 627 (1995).

[40] M. Wohlgenannt, X. M. Jiang, and Z. V. Vardeny, *Phys. Rev. B*, **69**, 241204 (2004).

[41] L. Yu, "*Solitons and Polarons in Conducting Polymers"*, Ed. by World Scientific.

[42] H. Topsöe, *Z. Kristallogr.*, **8**, 246 (1884).

[43] D. B. Mitzi, *Inorg. Chem.*, **35**, 7614 (1996).

[44] J.-H. Choy, Y.-S. Han, N.-G. Park, H. Kim, and S.-W. Kim, *Synth. Met.*, **71**, 2053 (1995).

[45] S. V. Chong, B. Ingham, and J. L. Tallon, *Curr. Appl. Phys.*, **4**, 197 (2004).

[46] D. B. Mitzi, C. A. Field, Z. Schlesinger, and R. B. Laibowitz, *J. Solid States Chem.*, **114**, 159 (1995).

[47] O. Knop, R. E. Wasylishen, M. A. White, T. S. Cameron, and M. J. M. van Oort, *Can. J. Chem.*, **68**, 412 (1990).

[48] B. R. Vincent, K. N. Robertson, T. S. Cameron, and O. Knop, *Can. J. Chem.*, **65**, 1042 (1987).

[49] K. Tanaka, R. Ozawa, T. Umebayashi, K. Asai, K. Ema, and T. Kondo, *Physica E*, **25**, 378 (2005).

[50] N. Mercier, A. Seyeux, C. Morel, and A. Riou, *Acta Crystallogr. C*, **58**, m127 (2002).

[51] K. Yamada, T. Matsui, T. Tsuritani, T. Okuda, and S. Ichiba, *Z. Naturforsch.*, **46a**, 307 (1990).

[52] A. Poglitsch, and D. Weber, *J. Chem. Phys.*, **87**, 6373 (1987).

[53] D. Weber, *Z. Naturforsch.*, **33b**, 862 (1978).

[54] K. Yamada, Y. Kuranaga, K. Ueda, S. Goto, T. Okuda, and Y. Furukawa, *Bull. Chem. Soc. Jpn.*, **71**, 127 (1998).

[55] Q. Xu, T. Educhi, H. Nakayama, N. Nakamura, andM. Kishita, *Z. Naturforsch.*, **46a**, 240 (1991).

[56] D. B. Mitzi, *Inorg. Chem.*, **39**, 6107 (2000).

[57] D. B. Mitzi, *J. Chem. Soc*., *Dalton Trans*., p.1 (2001).

[58] D. B. Mitzi, C. A. Field, W. T. A. Harrison, and A. M. Guloy, *Nature*, **369**, 467 (1994).

[59] D. B. Mitzi, S. Wang, C. A. Field, C. A. Chess, and A. M. Guloy, *Science*, **267**, 1473 (1995).

[60] T. Ishihara, J. Takahashi, and T. Goto, *Phys. Rev. B*, **42**, 11099 (1990).

[61] Ri-Zhu Yin, and Chul Hyun Yo, *Bull. Korean Chem. Soc.*, **19**, 947(1998).

[62] D. B. Mitzi, K. Chondroudis, and C. R. Kagan, *Inorg. Chem.*, **38**, 6246 (1999).

[63] B. Tieke and G. Chapuis, *Mol. Cryst. Liq. Cryst.*, **137**, 101 (1986) ;B. Tieke and G. Chapuis, *J. Polym. Sci. Polym. Chem. Ed.*, **22**, 2895 (1984).

[64] P. Dye, and T. A. Skotheim, *Hanbook of conductive polimers*, Vol **1**, Ed. Markel Dekker, New York, 117 (1986).

[65] G. Heger, E. Henrich, and B. Kanellakopulos, *Solid States Comm.*, **12**, 1157 (1973).

[66] D. B. Mitzi, K. Liang and S. Wang, *Inorg. Chem.*, **37**, 321 (1998).

[67] H. Elleuch, M. Kamoun, A. Daoud, and T. Jouni, *Phys. Sta. Sol. (a)*, **157**, 3 (1996).

[68] M. H. Ben Ghozlen, A. Daoud and J. W. Bats, *Acta Crystallogr. Sect. B*, **37**, 1415 (1981).

[69] Z.Y. Cheng, Z. Wang, R.B. Xing, Y.C. Han, and J. Lin, *Chem. Phys. Lett.*, **376**, 481 (2003).

[70] F. Chiarella, A. Zappettini, P. Ferro, T. Besagni, F. Licci, A. Cassinese, M. Barra, R. Vaglio, and C. Aruta, *Cryst. Res. Technol.*, **40**, 1028 (2005).

[71] G. Cantele, and D. Ninno, *unpublished*.

[72]I. Pabst, H. Fuess and J.W. Bats, Acta Crystallogr. C **43**, 413 (1987).

[73] J.P Steadman and R.D. Willett, Inor. Chim. Acta **4**, 367 (1970).

[74] F. Barendregt and H. Schenk, Physica **49**, 465 (1970).

[75] D. Abdellaziz, A. Thierr-Sorel, R. Perret, B. Chaillot and J.E. Guerchais, Bull. Soc. Chim. France **103**, 535 (1975).

[76] K. Yamada, Y. Kuranaga, K. Ueda, S. Goto, T. Okuda, and Y. Furukawa, *Bull. Chem. Soc. Jpn.*, **71**, 127 (1998).

[77] K. Yamada, H. Kawaguchi, T. Matsui, T. Okuda, and S. Ichiba, *Bull. Chem. Soc. Jpn.*, **63**, 2521-2525 (1990).

Chapter 2

Synthesis and film deposition techniques

2.1 Synthesis and crystal growth

The study of single crystals generally represents the best way to examine the structure and the intrinsic physical properties of a material. However useful information can be obtained by the study of polycrystalline bulk or powder compounds. This is also a fundamental step toward the knowledge of the properties of a material for thin film realization, as required for electronic and optical applications. In this thesis work we have concentrated ourselves on the synthesis of powders both as test and precursors for film deposition.

As reported by Mitzi et al. [1], generally, given the good solubility of many metal halides in polar organic and aqueous solvents, as well as the strong tendency to self-

assemble, single crystals of the organic–inorganic perovskites can be grown from near-ambient-temperature saturated solutions containing the relevant metal halide and the organic salts. However, occasionally situation arise where either the organic cation or the metal halide is not easily soluble or stable in common solvent or there can be problem of compatibility. The situation becomes more difficult for large and more complex organic cations, because of a possible incompatibility in the solubility requirements for the organic and inorganic component salts. In this case a possible answer can be to enhance the temperature solution to improve solubility. Alternative ways are sol-gel techniques or solid-state reactions, but in the latter case, given the low decomposition temperature of the organic salts (typically below 300° C), low temperature techniques are required. This is possible thanks to the self-assembled properties of this class of compounds and, in many cases, even room temperature processes can work well. Moreover, an important parameter to be taken into consideration is the stability of metal oxidation states. Octahedral coordination is not well accepted by some metals as Fe and Cr that tend to a 3+ oxidation state. In these cases, the compound need to be synthesized in an inert, oxygen free, atmosphere to avoid oxidation.

Arend et al. [2] have provided a through discussion of solution technique used for synthesizing a number of simple layered perovskites with general formula $(C_nH_{2n+1}NH_3)_2MX_4$ and $NH_3(CH_2)_nNH_3MX_4$, where M = Cd, Cu, Fe, Mn or Pd, X = Br or Cl and $n \geq 1$. The proposed technique, consists of a isothermal evaporation of a solution containing stoichiometric amounts of organic ammonium halide and bivalent metal salt melted into a suitable solvent. In these cases the solvents include n-methyl-2-pyrrolidone, water (very good), hydro-halogen acid, methanol, ethanol, acetone, glycol (good), isopropyl-alcohol and diethyl-ether (slightly soluble). All these solvents result to be efficient for solution synthesis of crystals or powders. In particular, as reported by Whealy [3], solubility of these class of compound seems to be directly proportional to the dielectric constant of the solvent. Besides these compounds results all very soluble in water, but when they are solved in its, the complex ion MX_4^{-2} is apparently always decomposed.

Powders of the layered copper compound series $(C_nH_{2n+1}NH_3)_2CuCl_4$ were synthesized following Arend indications. They were precipitated by evaporating a stoichiometric ethanol (or methanol) solution of $CuCl_2$ with the ammine halide salt until gold-yellow precipitate formed. The precipitate was filtered and washed with ether and finally dried in

air at 40°C [4].

To obtain $CH_3NH_3SnBr_3$ polycrystalline powders it was necessary to synthesize first a tin methyl-ammonium bromide salt. CH_3NH_3Br powders were obtained by mixing stoichiometric amounts of commercial aqueous solutions of CH_3NH_2 (41%) and HBr (48%). A white precipitate was formed by slowly evaporating the solvent. This was then filtered and washed with ether (P1). $CH_3NH_3SnBr_3$ polycrystalline powders were precipitated by adding solid P1 to $SnBr_2$ (Fluka 99%) saturated water solution. A red precipitated was formed, which was filtered and washed in ether (P2) [5]. The X-ray powder diffraction (**Figure 2.1**) showed that P2 was the single-phase $CH_3NH_3SnBr_3$ cubic perovskite by comparison with simulated spectra obtained from literature data ([6], [7] a = b = c = 5.90Å)

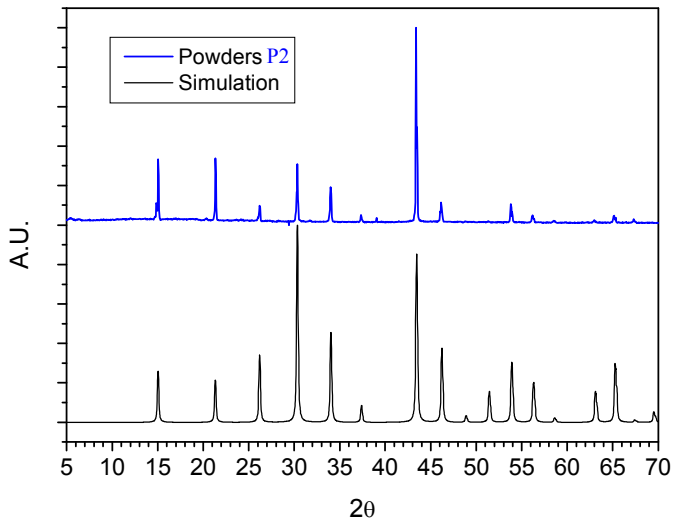

Figure 2.1 – *Comparison between powder of obtained by melt technique, with powderX 2.3 simulation program spectra settled from literature data of single crystal x-ray spectroscopy.*

For the $CH_3NH_3SnCl_3$ compound, instead, we have experienced strong difficulties to synthesize powders from solutions. In 1998 Yamada [8] has reported synthesis of powders by a solid-state reaction between alkylammonium chloride and $SnCl_2$ purified by a Bridgman or zone-melting technique before use.

2.2 Organic-inorganic thin film deposition techniques

Many potential applications involving the organic-inorganic hybrids depend on the availability of simple and reliable thin film deposition techniques. Deposition of hybrid materials, generally, results to be rather difficult, but it is certainly "challenging", to cite Mitzi in one of his reviews [9]. This is because of the distinct physical and chemical character of the organic and inorganic components. Organic materials, as an example, tend to be solved into different chemicals then those appropriate for the inorganic components and, even in the cases where the hybrid is soluble, adverse substrate wetting characteristics make "solution" deposition techniques inappropriate. The irregular surfaces obtained with solution techniques, make this technique inappropriate in many cases, since uniform coating is a typical request for most applications. On the other hand, for vacuum evaporation techniques, the gradual heating of organic-inorganic composites typically results in the decomposition or dissociation of the organic component at a lower temperature in respect to the ones required for the direct thermal evaporation of the inorganic components. However different routes for thin film deposition of organic-inorganic hybrids were recently successfully implemented.

2.2.a Film growth by solution-based techniques

Different solution-based techniques for organic film growth or, more appropriately, "substrate coating" have been tested in different frames and for different applications. Starting form the knowledge of these techniques, solution techniques were applied also to hybrid film realization [9].

Spin coating is a simple and (in principle) very cheap technique that enables thin film deposition of many organic-inorganic perovskites on a variety of substrates, including glass, quartz, sapphire and silicon. The relevant parameters for the deposition include the substrate, the substrate-solution interaction, the atmosphere condition during spinning, the solvent, the solute concentration and the spin speed. A balance between these parameters is

needed to achieve good film quality of desired thickness and uniformity. The choice of the type and size of the substrate to be coated depend, of course, on the particular use or applications under consideration, and an important element for the quality of the spin coated film is the substrate surface preparation. In general, standard cleaning techniques for each particular substrate type before thin film deposition should be followed to obtain high quality films. As an example, pre-treating the substrate with a cohesion promoter may improve the wetting properties of the solution. In the spin coated $(C_nH_{2n+1}NH_3)_2PbBr_4$ films it is preferable to clean the glass or quartz substrate with KOH in ethanol [10]. Furthermore, it is important to monitor and control particulates in the environment and to control the atmosphere quality in order to avoid water absorption or oxidation, especially in the case of instable metal halogen complexes or organic cations. Incorporation of particulates into the films (a typical problem of spin coating technology) could lead to electrical shorts or weak links that strongly degrade the film performances in the final application.

In conclusion, spin coating is a promising technique for many materials and applications, but there are several drawbacks, and first of all the problem of precise control of the film thickness, uniformity and morphology over large areas. In addiction, the necessity to individuate a liquid capable to dissolve both organic and inorganic component salts becomes a restrictive condition when complex organic cations are involved.

Other solution techniques for depositing the organic-inorganic hybrid include ink-jet printing, stamping and spry coating, thereby opening up the possibility of depositing these materials under a wide set of conditions and on many different types of substrates, including flexible plastic ones. For all these techniques, as for spin coating, the problem of the choice of a suitable solvent is a severe one. Also the sol-gel method has been taken into consideration for hybrid films. In this technique a solid phase forms through the "gelation" of a colloidal suspension, a chemical condensation reaction typically used to produce amorphous films [11]. For this method, generally, the tendency of wet gel layers to crack during drying processes, limits the thickness of the films to approximately 1 μm.

2.2.b Film growth by two-step process

Recently, a two step dip-processing technique has been developed [[12]], that potentially combines the advantages of a pure solution process, as spin coating, with those of evaporation techniques that will be discussed in the next section. The method consist in the pre-deposition of a metal halide film by vacuum evaporation (or in some case solution deposition) and then in a dipping process into a solution containing the organic cation (**Figure 2.2**). The solvent for the dipping solution is selected in such a way that the organic salt is soluble, but the starting metal and the final hybrid compound are not very soluble.

In the case of perovskite organic-inorganic hybrids, for which there is a strong chemical affinity between the organic and inorganic component salts, a strong thermodynamic driving force leads to the formation of the final structure. Thanks to the self-assembly properties of this class of materials, the organic cation dispersed in a solution intercalates into the film and reacts with the metal halide to form a crystalline film of the desired compound. An analogous version of the two-step dipping process has been reported in the literature [[13]], providing further support for this mechanism in which the hybrid perovskite film forms through the vapor phase intercalation of alkylammonium halide (bromine in the reference) into a pre-deposited metal halide film (lead(II) bromide in the reference).

Good results with dipping techniques were obtained in growing films of the complex family $(R{-}NH_3)_2(CH_3NH_3)_{n-1}M_nI_{3n+1}$ (where R=butyl or phenethyl; M=Sn or Pb; n=1,2,…,∞) composed by two different organic cations [[12]]. A special feature of the dipping technique is that in this case it is necessary to simply mix the two organic cations in the same dipping solution. A film of $(C_4H_9NH_3)_2PbI_4$, for example, was formed from 200 *nm* thick vacuum deposited film of PbI_2 by dipping it into a butylammonium iodine solution for 1-3 minutes (**Figure 2.2**). After that, the film was immediately washed with the same solvent of organic salt solution and then dried in vacuum. For the three-dimensional $CH_3NH_3PbI_3$ film the amount of time required to complete the reaction is much longer than that for the layered compounds (1-3 hours), presumably because of the lack of van der Waals bonding in the 3-D structure. In fact these bondings, when present, enable an easy path for unreacted organic ammonium and iodine ions to diffuse to the interface with the unreacted PbI_2. The obtained films result of good crystalline quality and surface morphology [[9]]. The dip-processing technique offers an useful combination of dry

and solution technique and it is expected to find application for those system in which thin films are difficult to prepare because of solubility problems or instability of either the organic and/or inorganic components.

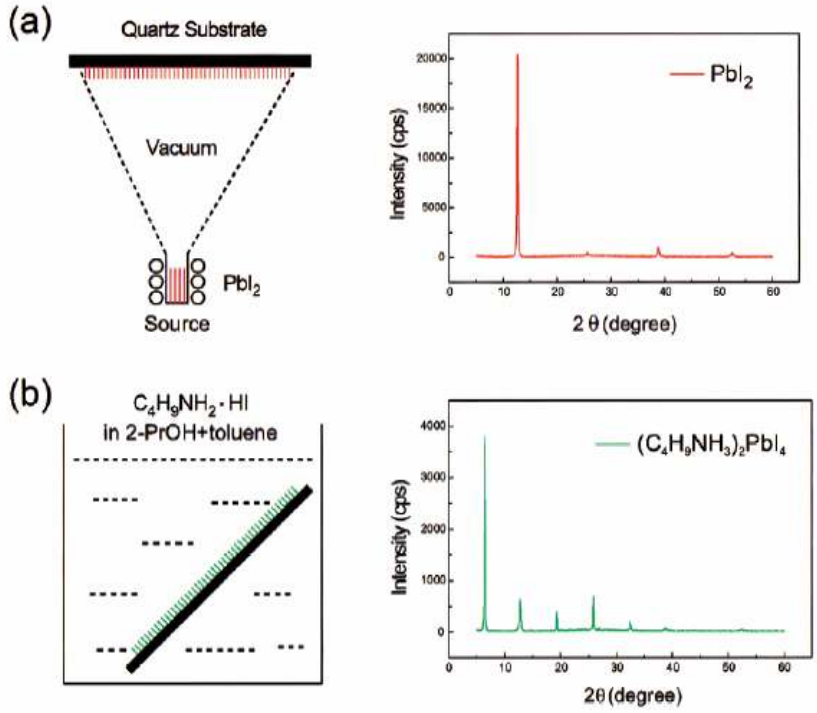

Figure 2.2 – *Schematic representation of the two-step dipping technique. In* (a)*, a film of the metal halide (in this case PbI_2) is deposited onto a substrate using vacuum evaporation, yielding to an ordered film with the characteristic X-ray pattern. The metal halide film is then* (b) *dipped into a solution containing the organic cation (in this case $C_4H_9NH_3^+$). The solvent (e.g., a mixture of 2-propanol and toluene) is a good solvent for the organic cation but not for the metal halide or the resulting hybrid. The resulting film after dipping has the characteristic X-ray pattern of the hybrid perovskite* [9].

Thermal evaporation of the inorganic component provides control over the film thickness and uniformity over reasonable large areas. However, during the reaction of the organic cation with the inorganic film, there is often a substantial grain growth with high local roughness, potentially leading to bad film morphology.

2.2.c Film growth by evaporation techniques

Solvent techniques are not always appropriate for the deposition of hybrid materials

and, for some applications or studies, vacuum-compatible thin film techniques have to be considered. The problem with direct evaporation of this class of compounds is that the organic component of the structure will generally dissociate or decompose from the material at substantially lower temperature in respect to the inorganic one, or in a shorter time. This implies that a conventional evaporation process can produce an alteration of the stoichiometric ratio or an undesired modification of the deposited materials. The use of vacuum techniques, on the other hand, can be important to obtain good interface quality between different functional layers by performing full in-situ device processing steps.
Two approaches have been considered to overcome the cited temperature and time incompatibility between the organic and inorganic components during evaporation:

Multiple source thermal evaporation technique is an interesting technique for the evaporation of organic and inorganic components, in which a separate source is utilized for each component. Obviously this enables the use of different power conditions for the evaporation sources.

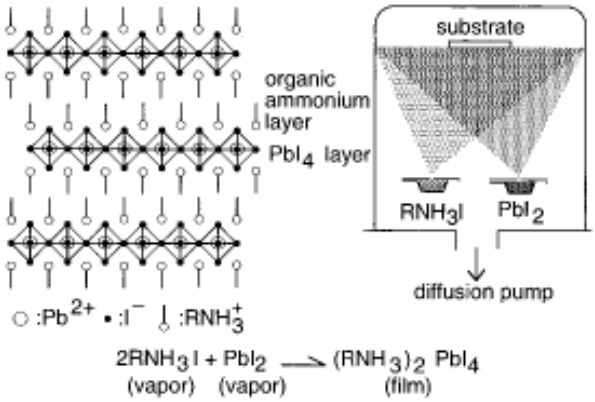

Figure 2.3 – *Schematic representation of the structure of the layered perovskites $(R\text{-}NH_3)_2PbI_4$ and preparation process of the material using a dual-source vapor deposition* [14].

Era et al. [14] have described in 1997 a dual source vapor deposition technique that allows the production of thin films without the use of solvents, in witch organic-inorganic perovskite films are grown by a simultaneous and independent deposition of the metal halide and organic ammonium halide components (**Figure 2.3**). In particular, lead(II) iodine and phenethylammonium iodine was evaporated from two different crucibles onto a quartz substrate at room temperature, under 10^{-6} *torr* pressure, to form the layered

perovskite $(C_6H_5C_2H_4NH_3)_2PbI_4$. The crucible temperature were respectively 570 *K* for PbI_2 and 520 *K* for $C_6H_5C_2H_4NH_2{\cdot}HI$, while rate deposition, controlled by a quartz oscillator balance, were 7.1 and 21 $ng\ cm^{-2}\ s^{-1}$. In this case, as for dipping technique, room temperature intercalation reaction in the layered structure was achieved, demonstrating the existence of a strong self-assembling force favoring the formation of the perovskite hybrid compound.

The dual source technique has the advantage of being a vacuum compatible technique and also offers, in principle, the possibility of a very good control of the film thickness. However, for practical device preparation, the set of organic cations that can be consistently evaporated is limited. In fact, the control of the organic salt evaporation rate and of the balance of the two deposition rates are difficult results to achieve simultaneously. This is because the organic salt typically decomposes into the free organic cation and the hydrogen halide that both are gaseous or have a high vapor pressure at room temperature, and evaporate as separated molecular species, not allowing the correct growth of the compound resulting in multiphase or disordered growth. Another disadvantage for traditional evaporation, is that high vacuum conditions are required during deposition in order to minimize the contamination, given the relatively long times required. Besides, the thermal evaporation of the organic salt typically occurs at much higher partial pressures in respect to the evaporation of the inorganic component alone. This high rate process tends to contaminate the vacuum chamber, with the need of extensive cleaning any time the organic component is changed. Finally, some organic species are not thermally stable up to the temperature required for thermal evaporation (e.g., iodoformamidinium cation $NH_2CH{=}NH_2{\cdot}HI$ [15]), making this technique impractical for these materials.

Single source techniques, on the other hand, would present difficulties as well, since the gradual heating of the organic-inorganic composites typically yields to a decomposition or a dissociation of the organic component at a lower temperature than that required for the evaporation of the inorganic component [16].

However, in 1999, a single source vacuum evaporation technique was been proposed by Mitzi et al. [17]. They have observed that when sealing hybrid crystals within an evacuated quartz tube, traces of the material evaporated from the heated tube walls, reassembled as a film of the original hybrid (as determined by optical analysis) on a cool section of the tube. This observation suggested the possibility to perform a controlled organic-inorganic hybrid

film deposition in vacuum using a single source evaporation technique, if the hybrid materials were heated fast enough (ablated). This technique was defined by its proposers as "Single Source Thermal Ablation" or "SSTA".

2.3 Single Source Thermal Ablation technique and deposition chamber

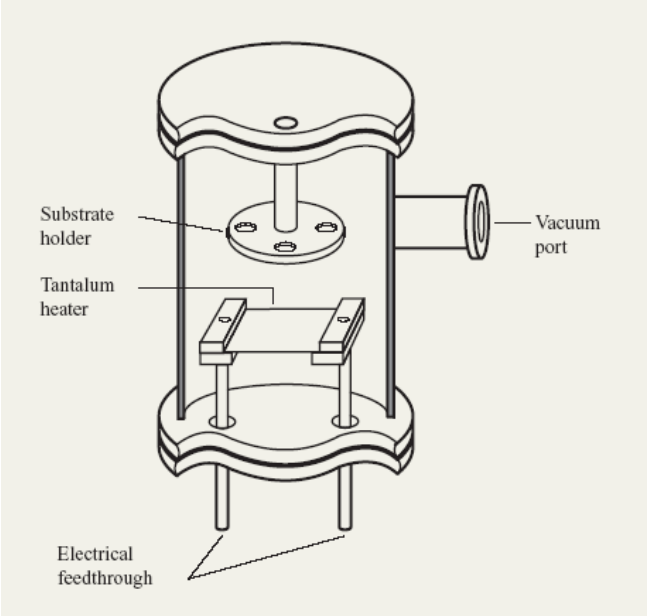

Figure 2.4 – *Cross-sectional view of a scheme of a single-source thermal ablation (SSTA) chamber* [17].

As already mentioned, the single source thermal ablation deposition process consists in placing the organic–inorganic hybrid on a thin tantalum heater within a vacuum chamber (**Figure 2.4**) and, when a large current is passed through the heater, the hybrid ablates from the source over a very short interval (<1 s) and deposits on the substrate positioned above the heater. Since the ablation process is essentially instantaneous, both the organic and inorganic components evaporate from the heater simultaneously and, in general, without

significant decomposition of the organic component. In many cases (especially with relatively simple organic cations), the as-deposited films are single-phase and crystalline, indicating that the organic–inorganic hybrids can reassemble on the substrate, even at room temperature [[17]]. For more complex organic cations, a short (20 min), low-temperature (200°C) anneal is sometime required to improve the film crystalline degree [[18]].

Starting from Mitzi design [[1,17]] an home-made deposition system to perform single source thermal ablation technique was set up at the CNR (National Research Council) Institute "IMEM" (Institute of Materials for Electronics and Magnetism) in Parma (Italy) **Figure 2.5**) [[4]].

All of the samples of this thesis were been made by SSTA technique into this deposition system. The system consists of a stainless steel chamber that can be pumped down to low pressures (10^{-7} *torr*) by a turbo-molecular pump in succession with a rotary pump, and in a power supply with the relative control unit.

Figure 2.5 – *Picture of the home-made single source thermal ablation deposition apparatus sited in Parma c/o IMEM-CNR.*

Inside the chamber, on the bottom, there are two high power feedthroughs that support a 1/16" thick tantalum foil that function as an evaporation crucible. On the top is located the

sample holder that can allocate up to four substrates. The distance between holder and crucible can be easily changed depending of the specific needs. The chamber is also equipped with a gas to feel it with inert gas (Ar) to open the chamber and store the deposited films in a controlled atmosphere. In order to heat the substrates up to 300 °C, the chamber has been equipped with an internal halogen lamp and a focusing system.

The deposition process consists of three main steps:

1. the precursor is placed onto the tantalum crucible and then the deposition chamber is evacuated;
2. when the pressure inside the vacuum chamber reaches a value of the order 10^{-6} *torr,* the ablation of precursor is accomplished passing through the crucible an high current (of the order of 150 Amps) for few seconds (an annealing process is also performed in some cases after deposition)
3. the deposited films, are taken out opening the chamber whilst flowing argon gas.

For layered $(C_nH_{2n+1}NH_3)_2CuCl_4$ films, the precursor was a methanol solution of single-phase powders of the same composition. 20-30 *mg* of the powders were dissolved in 0.2-0.3 *ml* of alcohol and the solution was transferred onto the crucible in the vacuum chamber. The concentration and the volume of the precursor solution were optimized for each compound, depending on the different solubility of the powders and on the required thickness and roughness [19].

For $CH_3NH_3SnBr_3$ film deposition, we used as film precursor either solid P2 (see paragraph 2.1) or stoichiometric mechanically ground mixtures of P1 and $SnBr_2$ (≈0.03 *g*, in total) with or without dissolving powders in the solvent.. Similar results were obtained in both cases, with respect to the deposition process and film quality [5]. The same procedure was been performed for $CH_3NH_3SnCl_3$ films. In this last case, because of difficulty in synthesising powders of the compound through simple solution techniques, the film was deposited using as precursor a mixture of the component salts.

All this demonstrates the high versatility and flexibility of SSTA. In fact the presence of solvent in the SSTA technique does not have a substantial role, but only the function to obtain a spatial uniformity of the precursor on the crucible. On the other hand one does not necessarily needed to start from powders of the compound.

The deposition parameters are quite similar for all the compounds. In particular the crucible-substrates distance is about 7-9 *cm*, the electrical power ≈ 200 *W*, and the crucible current is about 150 *A*. All the films are deposited on the substrate at room temperature.

Proportionality between the amount of material and film thickness (typically 100÷500 *nm*) and good reproducibility was systematically observed. Different substrates were used, including glass, quartz, Mylar, teflon, alumina, and $SrTiO_3$, Al_2O_3, MgO and Si crystals. No relevant change in the crystalline quality of the deposited films was observed changing the substrate type for all the different film compositions.

A relevant problem noticed, however, was the contamination of the deposition chamber. Therefore it has been necessary to make periodic cleaning cycles especially when changing the deposited compound. In fact, in many cases, if cleaning procedures were not adopted, the first attempts to deposit films with a new composition produced low quality results.

2.4 Structural and morphological characterization of deposited films

2.4.a X-ray analysis

The obtained film were primarily investigated and optimized in respect to the crystallographic quality. The technique used for the investigation of the structural properties of the films realized for SSTA is X-rays diffraction. This type of analysis allows to determine the crystal structure, the crystalline degree, or the distribution of the grain orientations [20]. The oriented structure of a crystal behaves like a diffraction reticulum for X-ray radiation and the interference spectrum that is generated contains a large amount of information on the crystal itself. In particular the *Bragg law* holds "reticular spacing" information:

$$2d\sin\theta = n\lambda \qquad (2.1),$$

where λ is the X-ray radiation wavelength, n is an integer number, θ is the reflection angle set equal to the incidence angle, d is the distance between two reticular planes and depends on the particular set of planes considered, as classified according to the Miller scheme (Miller indices [20]). From relation (2.1) it is possible to measure the crystal lattice parameters.

Measurements on both films and powders, were been realized by a standard Siemens D-500 diffractometer with a Cu K_α source radiation (a schematic apparatus representation in **Figure 2.6**). In particular, samples were measured using the so called ω–2θ (or θ–2θ) *scan* diffraction measurement technique.

In this technique the incidence and reflection angle ω and θ are changed simultaneously so that the condition $\omega = 2\theta / 2$ is always satisfied (symmetrical configuration: here 2θ is the angle between the incident source ray and emerging ray, while ω is the angle between the sample surface and the incident ray). When the reflection angle catches up the value for which the relation of constructive interference, given by the Bragg law, holds, a strong signal is observed at the detector corresponding to a peak in the intensity vs. 2θ spectrum.

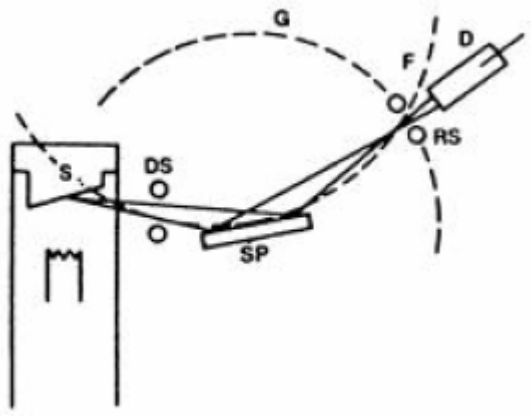

Figure 2.6 – *Schematic representation of an automatic diffractometer Bragg-Brentan geometry type.S is the X-ray source, D the detector of diffracted ray, SP the sample holder, and G is 2θ goniometer.*

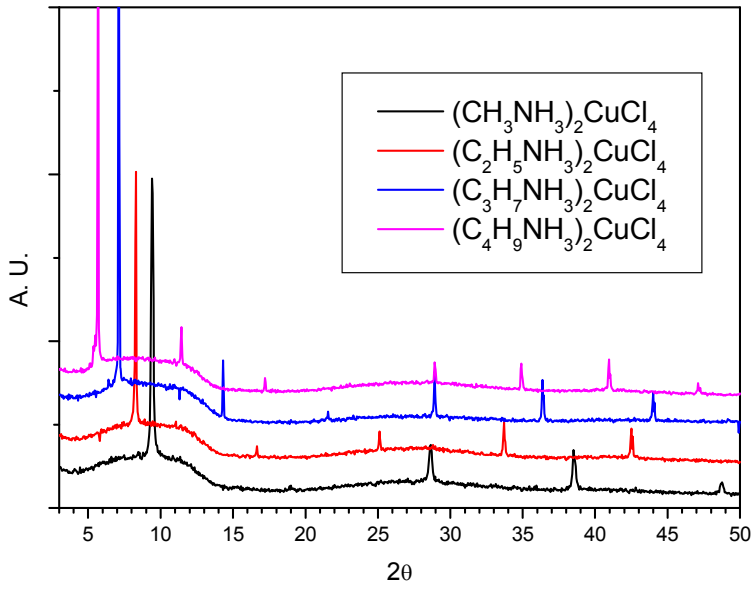

Figure 2.7 – *θ-2θ diffractogram of the $(C_nH_{2n+1}NH_3)_2CuCl_4$.series of compound. The different curve are vertically shifted to a greater clarity.*

When the measurement is carried out on a randomly oriented powder, the peak intensity depends on the intrinsic details of the crystal structure. If the measurement is carried on films, by comparing the results with the corresponding powder spectrum, it is possible to get information also on the possible preferential orientation of the film grains. As an example, the presence in the spectrum of intense peaks corresponding to the Miller indices (0 0 l), indicates that film has grown orienting crystallographic axis c in the direction normal to the substrate plane. In this case from the width of the diffraction peak it is possible estimate the degree of preferential orientation.

For $(C_nH_{2n+1}NH_3)_2CuCl_4$ compounds, their crystal structures were reported in **Chapter 1**. Literature data [21,22,23,24] indicate that the compounds with $n>1$ are orthorhombic, while the $n=1$ hybrid was better refined in the monoclinic system (monoclinic angle β=110.1). **Figure 2.7** shows the $\theta-2\theta$ X-ray diffraction patterns of optimised films of $(C_nH_{2n+1}NH_3)_2CuCl_4$, grown on glass. No significant differences were detectable in the X-ray patterns when changing the substrate. The exclusive presence of (0 0 l) sharp reflection peaks indicates that the films are single phase, well crystallized, and with a dominant c-axis orientation of the grains, where the c-axis is the direction orthogonal to the perovskite

sheets. By assuming that the films have the same crystal structure as the corresponding powder, from these measurements the "c" parameter values turn out to increase with increasing the length of the ammine chains (*n* in the chemical formula).

n	**c film (Å)**	**d (Å)**	**c powders (Å)**	**c literature (Å)**
1	10.07±0.05	9.41	9.90±0.05	9.971 [21] (bulk)
2	21.33±0.01	10.75	20.91±0.05	21.18 [22] (bulk)
3	24.90±0.05	12.45	24.71±0.05	24.66 [23] (bulk)
4	31.00±0.05	15.50	30.85±0.05	30.75 [24] (bulk)

Table 2.2 – *"c" parameter of the $(C_nH_{2n+1}NH_3)_2CuCl_4$ film and bulk compounds, distance between the perovskite sheets (d) in the films Vs number of carbon atoms* [19].

The measured "c" parameters of the films and of the corresponding bulk compounds are reported in **Table 2.2** as a function of *n*. In the same table also the distances between the perovskite sheets, d, are shown. They were calculated from the structural parameters and were defined as $d = c/2$ (orthorhombic structure, $2 \leq n \leq 4$) and $d = c \cdot \sin(\pi - \beta)$ (monoclinic structure, $n=1$). In **Figure 2.8** it is shown the correlation between the perovskite sheet distance (*d*) and the number of carbon atoms in the alkyl chain. Data are well fitted by a parabolic correlation function.

The values of the c-axis in **Table 2.2** for $n=2$, were measured using a different, more accurate, diffractometer as a test. In this case a more accurate sample alignment significantly reduces measurement errors. In any case consistent results were found with the two different diffractometers.

The c parameters of the films deposited on glass were found to be systematically larger than those of the corresponding powders (**Table 2.2**). Since there cannot be any reticular matching between the amorphous substrate and the crystalline films, we tentatively attribute the effect to the weak Van der Waals forces on the ammine chains. This seems insufficient to counteract the effect of the reduced pressure along the c direction in the film in respect to the bulk. As a consequence the structure relaxes (c parameter lengthens) in the same direction [19].

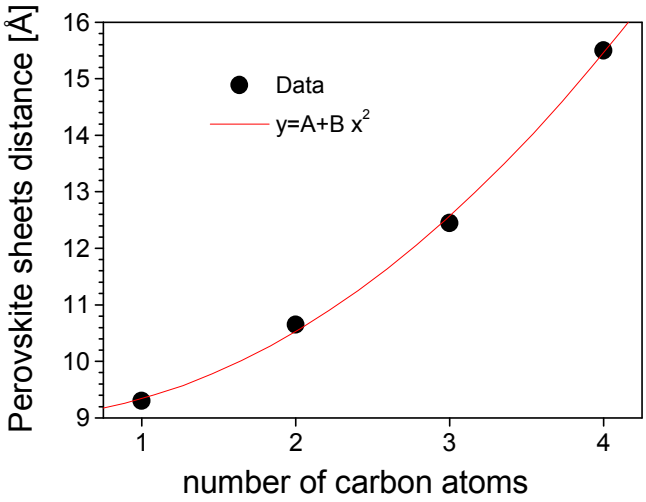

Figure 2.8 – *Correlation between perovskite sheets distance of hybrid structure with different organic chain length (in red the fit curve).*

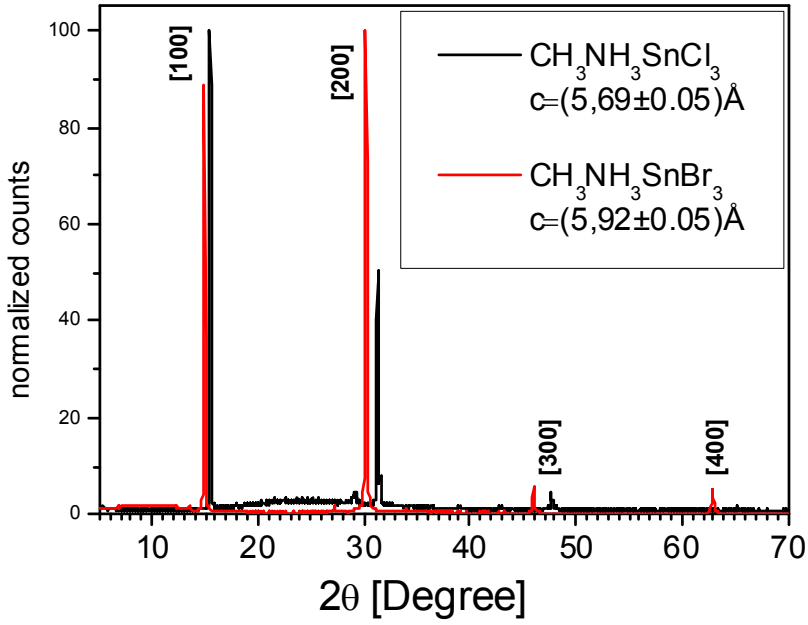

Figure 2.9 – *Comparison between X-ray diffraction spectra of $CH_3NH_3SnBr_3$ (red line) and $CH_3NH_3SnCl_3$ (black line). In the square bracket, reflection Miller index have been indicated.*

The X-ray diffraction pattern of $CH_3NH_3SnX_3$ glass deposited films, where X= Cl and Br, is shown in **Figure 2.9**. As for the copper layered films, only the (0 0 l) set of reflection planes are present, indicating that the films are well crystallized and c-axis oriented. Obviously changing the halogen atom in the structure from bromine to chlorine, the cell parameter decreases because of the smaller ionic radius of the chlorine atom.

X	c film (Å)	c powders (Å)	c literature (Å)
Cl	5.69±0.05	##	5.726* [8] (bulk)
Br	5.92±0.05	5.88±0.05	5.90 [6,7] (bulk)

Table 2.3– *c-axis parameter of $CH_3NH_3SnX_3$ films obtained with SSTA technique in comparison with powders and literature reported values.* c-axis parameter of chlorine compound was one of the three cell parameters reported for the room temperature triclinic phase.*

In particular methyl-ammonium chlorostannate must deserve special attention for its complex structural transition around room temperature [8]. In fact from 478 K to 297 K the structure of the compound changes from an high temperature cubic phase to a room temperature triclinic phase. To better understand the $CH_3NH_3SnCl_3$ film reticular structure, a more careful X-ray diffraction analysis was executed on films deposited on different substrates as glass, MgO [100] and MgO [111]. By this analysis $CH_3NH_3SnCl_3$ films results multiphase with the stabilization of high temperature phase on the substrate surface.

2.4.b Surface and morphology

Thickness and roughness of the deposited films were studied by standard profilometer analysis. The film thickness typically ranged from 100 to 800 nm and could be controlled qualitatively by varying the precursor mass (either the concentration or the volume of the solution or the amount of the starting salts). Both thickness and roughness were measured systematically on deposited films. The roughness was estimated to be not higher than 5% for all the films. Optical microscope observation also revealed the presence of sufficiently homogeneous surfaces. By this systematic analysis no differences were observed on changing substrate type or film composition.

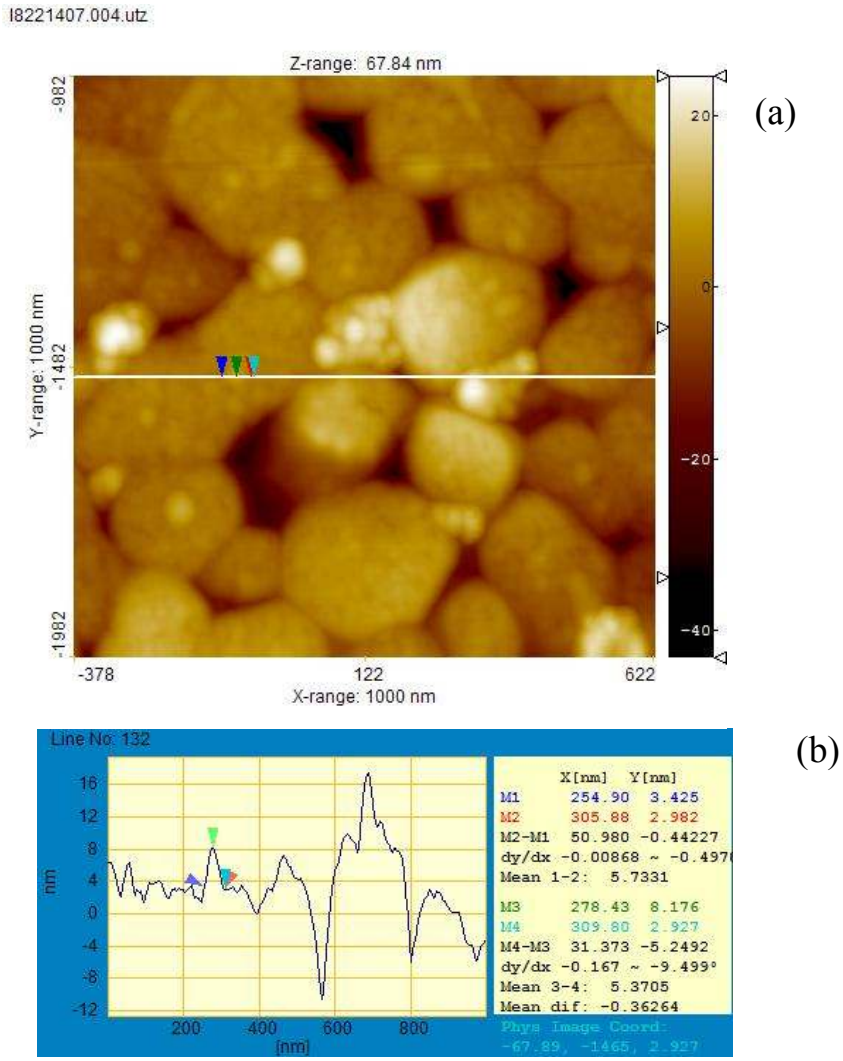

Figure 2.10 – (a) *AFM image of a $CH_3NH_3SnCl_3$ film of 1μm x 1μm. White line indicate the investigated zone for transversal analysis shown in picture* (b).

$CH_3NH_3SnCl_3$ is the more complex compound to realize in thin film form. Its surface was observed by AFM (Atomic Force Microscope) and SEM (Scanning electron Microscope) analysis. A commercial AFM of Parker Scientific Instruments, Autoprobe model, was been used to acquire room temperature surface images.

The AFM image of a $CH_3NH_3SnCl_3$ film, 810 nm on MgO substrate, showed a granular morphology, typical of a three dimensional growth (**Figure 2.10 (a)**). The grains are not well-packed and have not a well defined form at submicrometric size (100÷500 *nm*). In **Figure 2.10 (b)** the transversal profile of the AFM measurements related to the

white mark line on **Figure 2.10 (a)** is reported. From this, the average roughness results to be about 20 *nm* and 1 *nm* on the single grain. A twin film of that used for AFM, was also characterized by SEM analysis.

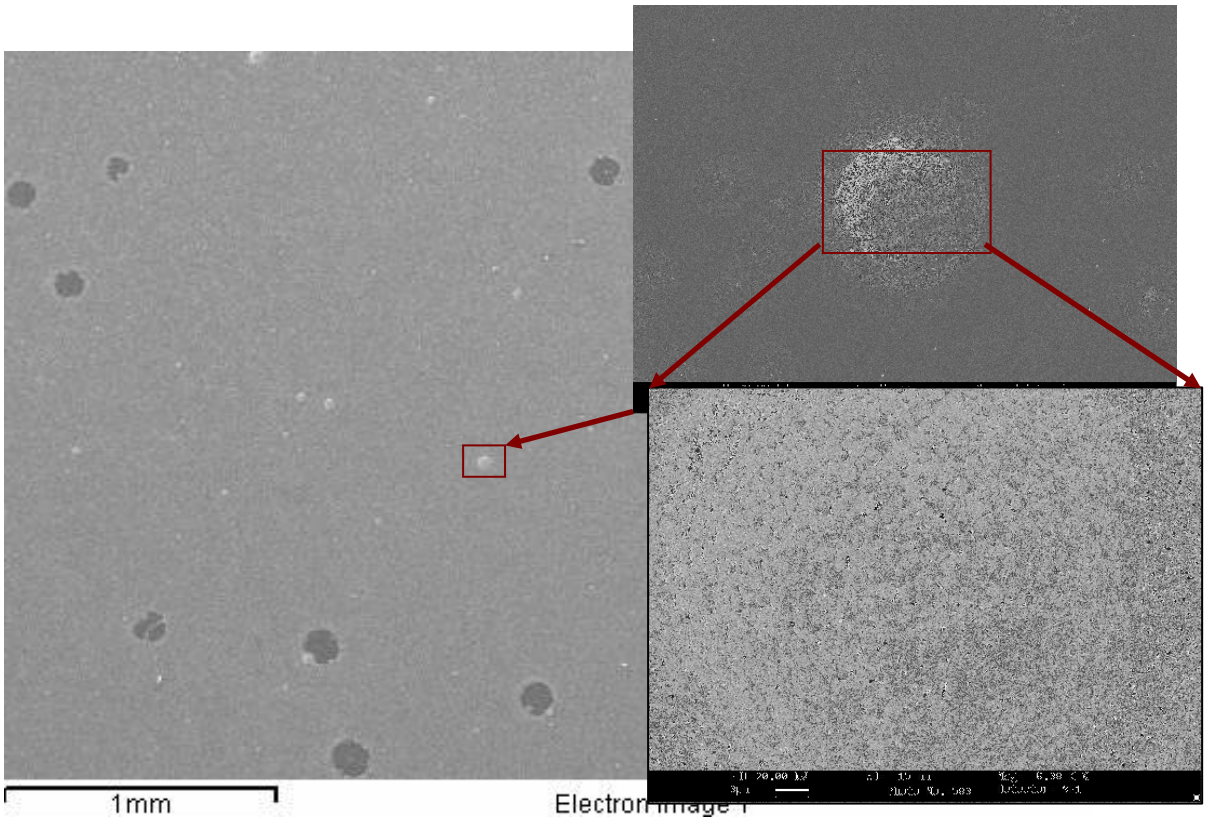

Figure 2.11– *Large area SEM image (3 mm x 4,5 mm) of a $CH_3NH_3SnCl_3$ film. The red rectangle is related to the first zoom (150 μm x 200 μm) (up-right side). This window was been further zoomed. This zoom (30 μm x 45 μm) is reported in the down-right side of the picture.*

The large area image shows an homogeneous surface, with some little bright spots and large dark zones. Typically the SEM brightness depends on the distance between the observed zone and the focal plane of the microscope, as well as on the surface chemical composition. In particular, the last feature is at the base of the so called Energy Dispersive Spectrometer (EDS) analysis.

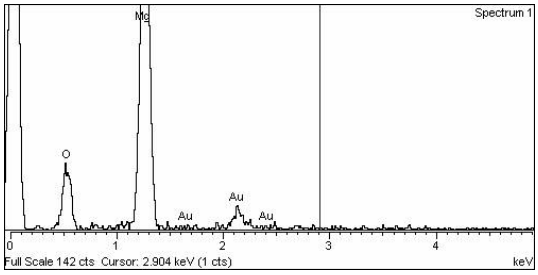

Dark zone:

Element	Weight%	Atomic%
O	39. 94	50.26
Mg	60. 06	49.74
Totals	100.00	

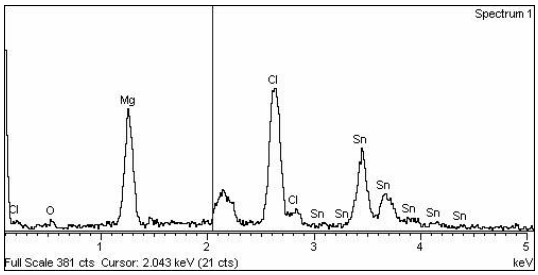

Large Areas:

Element	Weight%	Atomic%
O	14. 16	31.46
Mg	21. 67	31.68
Cl	25. 09	25.15
Sn	39. 08	11.70
Totals	100.00	

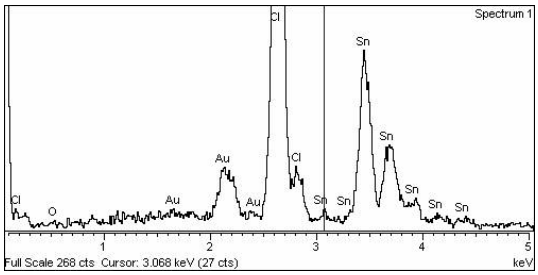

Bright Zone:

Element	Weight%	Atomic%
O	6.10	18.44
Cl	45.24	61.73
Sn	48.66	19.83
Totals	100.00	

Figure 2.12 – *EDS results of a $CH_3NH_3SnCl_3$ film on MgO substrate. On the left side there are spectra acquired from the image shown in* ***Figure 2.10****. On the right it is proposed a schematic resume of chemical elements percent obtained by an appropriate data conversion form the related spectrum.*

Two step zooms were made on one of the bright spots (red rectangle) (**Figure 2.11**) where it was observed a drop-shaped crystallized outgrowth (probably a condensed drop). It is interesting to observe that by EDS analysis of this image (**Figure 2.12**) we find a strong presence of oxygen not related to the MgO substrate since there is not any magnesium trace. This type of defect is probably associated to the fast deposition process, in which some precursor material clusters can be expelled and splash onto the substrate by thermal excitation and mechanical vibration of the heated tantalum foil. On the other side EDS analysis shows that the dark zones are substrate areas not covered by the film. Anyway, as shown in **Figure 2.13**, the films result to be well structured and uniform with submicrometric well packed and flat grains. The presence of bright areas along the grain boundary could indicate the presence of an excess of tin probably due to segregation of unreacted $SnCl_2$.

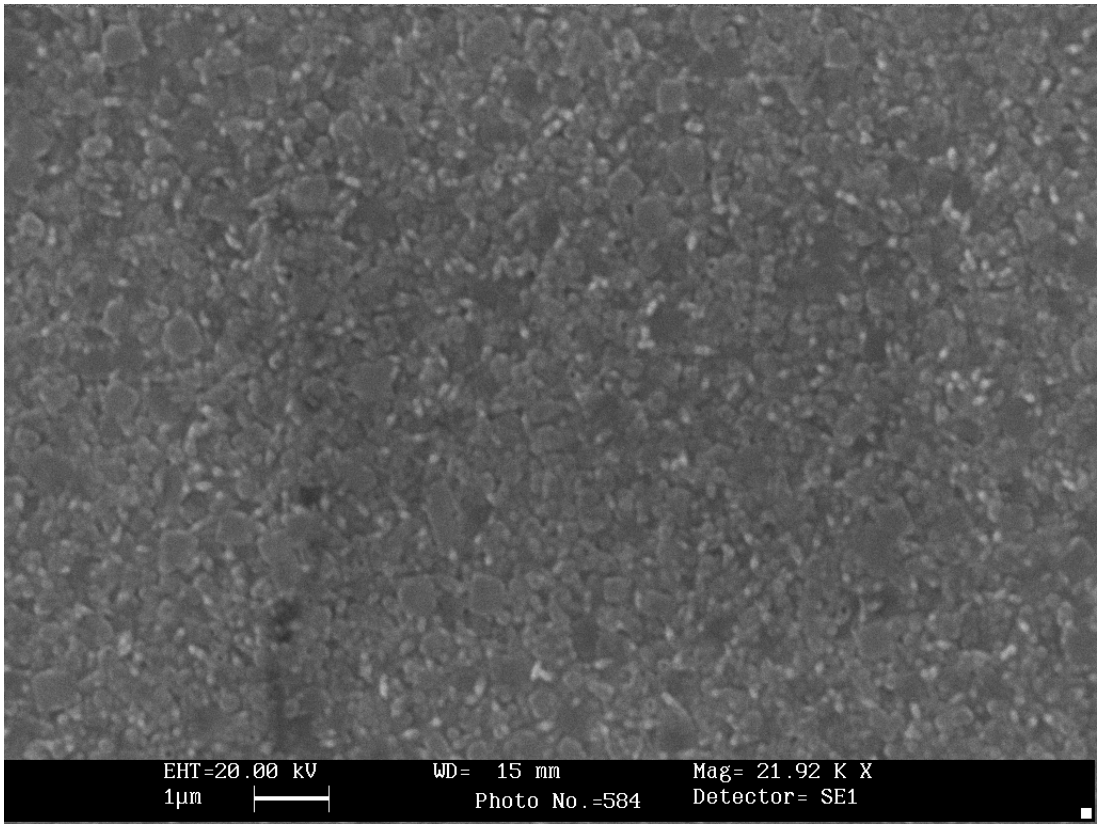

Figure 2.13 – Scanning Electron Microscope image of a film *of $CH_3NH_3SnCl_3$ on MgO substrates. Window size: 15 µm* x *10 µm*

Bibliography

[1] David B. Mitzi, *Progress in Inorganic Chemistry*, Vol **48**, Ed. by K. D. Karlin, Jonh Wiley & Sons, Inc. (1999)

[2] H. Arend, W. Huber, F.H. Mischgofsky, and G.K. Richter-van Leeuwen, *J. Crystal. Growth.*, **43**, 213 (1978).

[3] R. D. Whealy, D.H. Bier, and B.J. McCormick, *J. Am. Chem. Soc.*, **81**, 5900 (1959).

[4] C. Aruta, F. Licci, A. Zappettini, F. Bolzoni, F. Rastelli, P. Ferro, and T. Besagni, *Appl. Phys. A*, **81**, 963-968 (2005).

[5] F. Chiarella, P. Ferro, F. Licci, M. Barra, M. Biasiucci, A. Cassinese, and R. Vaglio, *submitted on Appl. Phys. A*.

[6] K. Yamada, H. Kawaguchi, T. Matsui, T. Okuda, and S. Ichiba, *Bull. Chem. Soc. Jpn.*, **63**, 2521-2525 (1990).

[7] N. Onoda-Yamamura, T. Matsuo, and H. Suga, *J. Chem. Thermodynamics* , **23**, 987 (1991).

[8] K. Yamada, Y. Kuranaga, K. Ueda, S. Goto, T. Okuda, and Y. Furukawa, *Bull. Chem. Soc. Jpn.*, **71**, 127 (1998).

[9] D. B. Mitzi, *Chem. Mater.*, **13**, 3283-3298 (2001).

[10] T. Ishihara, T. Ogawa, and Y. Kanemitsu, *Optical Properties of Low-Dimensional materials*, Eds., World Scientific, Singapore, p. 4 (1995).

[11] R. W. Jones, *Fundamental Principles of Sol-Gel Technology*, The Institute of Metals: London (1989).

[12] K. Liang, D. B. Mitzi, and M. T. Prikas, *Chem. Mater.*, **10**, 403 (1998).

[13] M. Era, N. Kakiyama, T. Ano, and M. Nagano, *Trans. Mater. Res. Soc. Jpn.*, **24**, 509 (1999).

[14] M. Era, T. Hattori, T. Taira, and T. Tsutsui, *Chem. Mater.*, **9**, 8 (1997).

[15] D. B. Mitzi, and K. Liang, *J. Solid State Chem.*, **134**, 376 (1997).

[16] M. J. Tello, E. H. Bocanegra, M. A. Arrandiaga, and H. Arend, *Thermochim. Acta*, **10**, 403 (1975).

[17] D.B. Mitzi, M. T. Prikas, and K. Chondroudis, *Chem. Mater.*, **11**, 542 (1999).

[18] K. Chondroudis, and D.B. Mitzi, *Chem. Mater.*, **12**, 169 (2000).

[19] F. Chiarella, A. Zappettini, P. Ferro, T. Besagni, F. Licci, A. Cassinese, M. Barra, R. Vaglio, and C. Aruta, *Cryst. Res. Technol.*, **40**, 1028 (2005).

[20] N.W. Ashcroft, and N.D. Mermin, *Solid States Physics*, Saunders College, Philadelphia (1985).

[21] I. Pabst, H. Fuess and J.W. Bats, *Acta Crystallogr. C*, **43**, 413 (1987).

[22] J.P Steadman and R.D. Willett, *Inor. Chim. Acta*, **4**, 367 (1970).

[23] F. Barendregt and H. Schenk, *Physica*, **49**, 465 (1970).

[24] D. Abdellaziz, A. Thierr-Sorel, R. Perret, B. Chaillot and J.E. Guerchais, *Bull. Soc. Chim. France*, **103**, 535 (1975).

Chapter 3

Optical properties and technological impact

3.1 Optical properties

As mentioned in the first chapter, hybrid perovskite based compounds exhibit very interesting optical properties such as photoluminescence and non-linear optical effects. In particular the 2D layered hybrid structures have attracted the scientists' interest. These systems can be indeed considered as a multi-quantum well structures (**Figure 1.17**) with the metal halide sheet acting as the well and the much wider bandgap organic layers acting as the barrier. In principle in this type of structure it is possible to obtain excitonic states by quantum confinement effects and photoluminescence, as well as electroluminescence, can be produced by radiative decay.

	Photoluminescence Excitonic Peak	Excitonic Absorption	Ref.
$(C_4H_9NH_3)_2GeI_4$	690 [(b)] *nm* (1.8 *eV*)		[11]
$(C_4H_9NH_3)_2SnI_4$	625 *nm* (2.0 *eV*)		[11]
$(C_6H_5C_2H_4NH_3)_2SnI_4$		608 *nm* (2.0 *eV*)	[1]
$(C_nH_{2n+1}NH_3)_2SnCl_4$ n =6,8	600 *nm* (2.06 *eV*)		[2]
$(C_6H_5C_2H_4NH_3)_2SnI_4 \cdot C_6F_6$		595 *nm* (2.1 *eV*)	[1]
$(C_nH_{2n+1}NH_3)_2MnCl_4$ n=1,2,3	588-602 *nm* (2.1 *eV*)		[3]
$(C_6H_5C_2H_4NH_3)_2(CH_3NH_3)Pb_2I_7$		563 *nm* (2.2 *eV*)	[8]
$(C_9H_{19}NH_3)_2(CH_3NH_3)Pb_2I_7$		562 *nm* (2.21 *eV*)	[17]
$(AEQT)PbBr_4$	540*nm* (2.3 *eV*)		[40]
$(CH_3NH_3)PbBr_3$		530 *nm* (2.34 *eV*)	[17]
$(AEQT)PbI_4$	520*nm* (2.4 *eV*)		[40]
$(C_4H_9NH_3)_2SnCl_4$	520 [(b)] *nm* (2.4 *eV*)		[25]
$(C_6H_5C_2H_4NH_3)_2PbI_4$	520*nm* (2.4 *eV*)	510*nm* (2.43 *eV*)	[8,38]
$(C_nH_{2n+1}NH_3)_2PbI_4$ n=4,6,8,9,10,12	485 *nm* (2.56 *eV*) LTP 520-5*nm*(2.4 *eV*) HTP	511-504 *nm* (2.43 *eV*)	[5,11] [17,8]
$(C_4H_9NH_3)_2EuI_4$	460*nm* (2.7 *eV*)		[4]
$(C_4H_9NH_3)_2(CH_3NH_3)_2Eu_2I_7$	455 *nm* (2.72 *eV*)		[4]
$(C_9H_{19}NH_3)_2(CH_3NH_3)_2Pb_3Br_{10}$		450 *nm* (2.76 *eV*)	[17]
$CH_3NH_3EuI_3$	449 *nm* (2.8 *eV*)		[4]
$(C_9H_{19}NH_3)_2(CH_3NH_3)Pb_2Br_7$		430 *nm* (2.9 *eV*)	[17]
$(C_4H_9NH_3)_2PbBr_4$		405 *nm* (3.1 *eV*)	[10]
$(C_9H_{19}NH_3)_2PbBr_4$		393 *nm* (3.15 *eV*)	[17]
$(C_nH_{2n+1}NH_3)_2CuCl_4$ n=1,2,3,4		375 *nm* (3.3 *eV*)	[30]
$(C_6H_5C_2H_4NH_3)_2PbCl_4$		330 *nm* (3.76 *eV*)	[17]
$(C_nH_{2n+1}NH_3)_2PbCl_4$		330 *nm* (3.76 *eV*)	[17,10]

Table 3.1 – *Summary of excitonic peaks reported in the literature for* $(R\text{-}NH_3)_2(CH_3NH_3)_{n-1}M_nX_{3n+1}$ *family where the group R is typically an alkyl- or phenyl- group, M is a metal of group 14 or, more rarely, a transition metal or a rare earth metal, and X is an halogen atom (I, Br, Cl). Wavelength are referred to the photoemission excitonic peak (second column) or to the related absorption one (first column) and are ordered from lower to higher energies.* LTP *and* HTP *in the table indicate respectively Low and High Temperature Phases while* [(b)] *indicates a broad band.*

In these materials, of general formula $(R\text{-}NH_3)_2(CH_3NH_3)_{n-1}M_nX_{3n+1}$, there is the possibility to tune the excitonic emission wavelength by changing the well width (controlled by the *n* and M-X bond length), the well separation (controlled by the organic radical R), and even the well depth (controlled by M and R). Given its spacing function, the organic radical can also play an active optical role in the structure and the choice of this component is essential to build up a suitable band alignment. In the **Table 3.1** emission and absorption excitonic wavelength, are reported from literature data.

Inside this class, the group 14 (IVA) metal compounds that have recently attracted a wide interest because of their strong room temperature photoluminescence. The remarkable feature of the exciton states in these systems is the exceptionally large binding energy and oscillator strength. In the alkylammonum lead(II) iodine system $(C_nH_{2n+1}NH_3)_2PbI_4$ (with n = 4, 6, 8, 9, 10, and 12), the exciton has a binding energy of 320 *meV* and an oscillator strength of 0.7 per formula unit enabling the observation of a strong room temperature photoluminescence [5]. These value is indeed very large, 8 times more in respect to the three dimensional similar compound $CH_3NH_3PbI_3$ [6]. This big difference is essentially related to the two-dimensionality of the exciton, somewhat "squeezed" in the inorganic perovskite layers. This is certainly one of the most interesting features of these self-assembled nanostructures. In the case of lead compounds, however, this effect is even stronger and somewhat unexpected. For typical layered system two-dimensionality can yield up to a fourfold enhancement of the binding energy [7]. In these compounds the enhancement effect of exciton binding energy is related to a "dielectric confinement" [8]. In $(C_nH_{2n+1}NH_3)_2PbI_4$ compounds, in fact, the dielectric constant of the well is $\varepsilon_w \approx 6.1$, whereas for the barrier layers it is $\varepsilon_b \approx 2.1$. The lower dielectric constant of the organic component leads to a reduced screening for carriers in the perovskite layers by "image charge effect". This produces an enhancement of the electron/hole Coulomb interaction and increases e^-/h^+ pairing in the exciton [9].

The most straightforward mean to test the dielectric modulation effect is to observe the change in the excitonic properties by varying the organic barrier material into the layered structure. In the family $(C_nH_{2n+1}NH_3)_2PbI_4$, just a little variation of the exciton luminescence peak, or exciton binding energy, has been observed [5], indicating that the wells are essentially isolated. This is due to the fact that the dielectric constants of the different alkyl chains are pretty much the same. In contrast, substituting the

alkylammonium cation (ε ≈ 2.1) with a phenethylammonium one (ε≈ 2.3), a 20% reduction in the exciton binding energy has been observed. This is predictable in the thin-well limit where the binding energy is expected to be inversely proportional to the square of the dielectric constant.

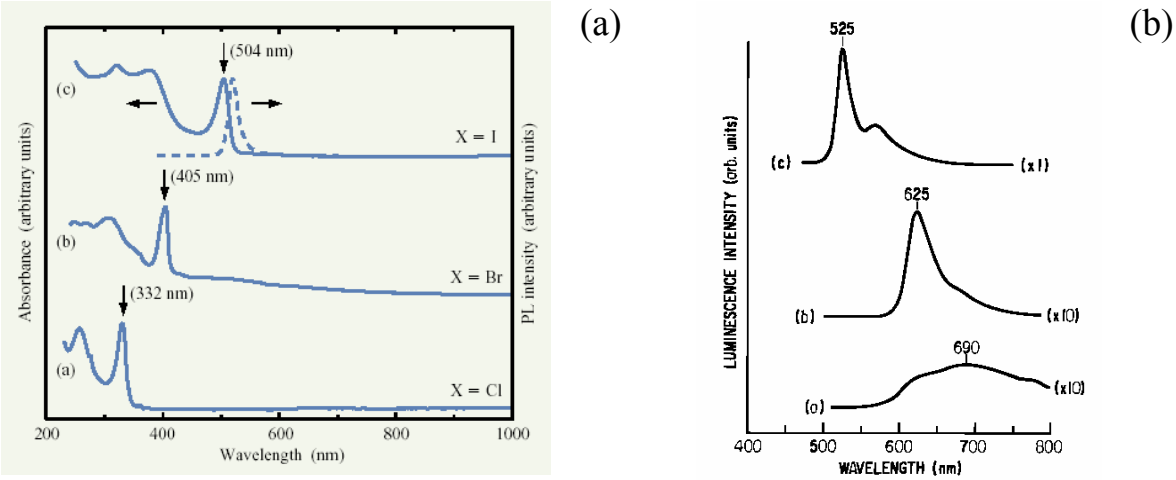

Figure 3.1 – (a) *Room-temperature UV–vis absorption spectra for thin films of* $(C_4H_9NH_3)_2PbX_4$ *with* (a) *X = Cl,* (b) *X = Br,* (c) *X = I. In each spectrum, the arrow indicates the position of the exciton absorption peak (with the wavelength in parentheses). In* (c)*, the corresponding photoluminescence (PL) spectrum* (λ_{ex} *= 370 nm) is indicated by the dashed curve. Note the small (~15 nm) Stokes shift between the absorption and emission peaks for the excitonic transition* [10]. **(b)** *Room temperature photoluminescence spectra for crystals of* $(C_4H_9NH_3)_2MI_4$ *with* (a) *M = Ge,* (b) *M = Sn, and* (c) *M = Pb, demonstrating a shift in the photoluminescence peak as a function of group IVB element. Intensities for the M = Ge and Sn spectra have multiplied by 10. The photoluminescence spectra were excited by 457.9 nm light from an argon ion laser* [11].

The sensitivity of the system to perovskite sheet thickness (see **Table 3.1**), or effective dimensionality, indicates that the excitons are sampling the extended perovskite sheets (i.e., they are reasonably mobile at room temperature and are basically Wannier-like in the plane of the inorganic sheets). Otherwise, as the halogen atom in the structure changes from I to Br or Cl, the band gap increases and the exciton states, that typically live near to the conduction band, undergo a "blue shift" (**Figure 3.1 (a)**). The change in the electronic transition related to the choice of the halogen in the structure, indicates that the valence band of the underlying electronic structure correspond to a hybridization of metal and halogen states. For example in $(C_nH_{2n+1}NH_3)_2PbI_4$ tight binding calculations demonstrate that the top of the valence band consists of 72% I(5p) states and 28% Pb(6p) states [12].

These results highlight the charge-transfer (rather than cationic) nature of the optical excitation process in these materials. Finally the same result can be obtained along group 14 (Ge → Sn → Pb) as showed in **Figure 3.1 (b)** and summarized in **Table 3.1**.

An exception is the europium series (see **Table 3.1)**. $(C_4H_9NH_3)_2EuI_4$, $(C_4H_9NH_3)_2(CH_3NH_3)_2Eu_2I_7$, and $CH_3NH_3EuI_3$ compounds were synthesized and for all them a strong blue photoluminescence was obtained. In contrast to the lead(II) iodides, for which there is a large red shift and intensity decrease of the room temperature luminescence going from two-dimensional to three-dimensional compounds, for europium(II) halides there is less difference in the intensity of the peaks and only a slight blue shift in going from 2D to 3D systems. This indicates a different exciton mechanism, the emission in europium compounds being related to more localized cationic excitations, that are relatively insensitive to the global structural details and dimensionality. The small blue shift in emission wavelength is expected to arise from the subtle differences in local coordination of the Eu^{2+} ions [13].

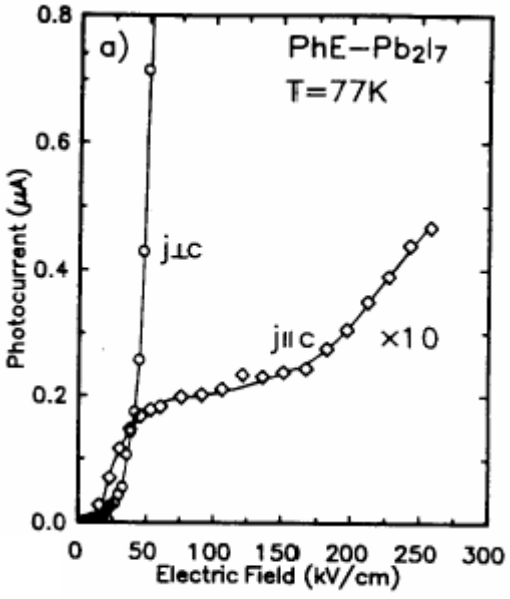

Figure 3.2 – *Photocurrent as a function of electric field with $j \parallel c$ and $j \perp c$ at 77K for $(C_6H_5C_2H_4NH_3)_2(CH_3NH_3)Pb_2I_7$* [14].

The strong photoluminescence in these metal halide systems accompanied with a substantial mobility of the carrier in the perovskite planes, suggest the possibility of electroluminescence. Early studies on electroluminescence in single crystals of $(C_6H_5C_2H_4NH_3)_2(CH_3NH_3)Pb_2I_7$ (i.e. two perovskite sheet in a layer) have been reported [14] (**Figure 3.2**). In this case pure silver paint electrical contacts were used on the sample. The photocurrent along the c-axis is much smaller than that along the well plane,

confirming the large anisotropy of the electronic band structure. Orange electroluminescence has been observed below 200 *K* with an applied electric field larger than 10 $kV \cdot cm^{-1}$ along the wells. This relative low value for the luminescence threshold field reflects the large electronic bandwidth in the plane of the perovskite sheets.

Other interesting optical properties of hybrid perovskite compounds are thermochromism [15] due to structural transitions, dielectric properties [16], and nonlinear optical effects. The sharp exciton state in the layered materials suggests the potentiality for strong optical nonlinearity, very important for applications in optical signal processing, when the frequencies of the pumping beam approaches the exciton energy [17]. The measured third order optical susceptibility $\chi^{(3)}$ for $(C_{10}H_{21}NH_3)_2PbI_4$ exhibits a large three-photon resonance [18]. The magnitude of the produced $\chi^{(3)}$ results comparable well with the reported values for conjugated organic molecules (such as polyacetylene [19]). A transient non-degenerate four-wave mixing was performed in the femtosecond domain in a stable exciton-biexciton regime on the $(C_6H_{13}NH_3)_2PbI_4$ compound demonstrating a strong exciton-exciton interaction in this type of systems [20].

In this thesis it is analyzed the change in optical properties with the change of one component in the 2D $[(C_nH_{2n+1}NH_3)_2CuCl_4]$ and 3D $[CH_3NH_3SnX_3]$ series structure to understand the possible correlations between structure and optical properties. Besides, the possibility to synthesize and study optical properties of transition metal halide compounds is explored, in view of exploiting such a potentiality and to find new materials for UV-LED applications. Indeed not much is reported in the literature on the absorption and photoemission in the UV range, as clear from **Table 3.1**.

3.2 Absorption measurements on films of the $(C_nH_{2n+1}NH_3)_2CuCl_4$ and $CH_3NH_3SnX_3$ series

Analysis of the absorption data was carried out to test the optical quality of SSTA deposited films as well as to determine the predominant optical transition and electronic configuration (presence of excitonic states transition) of the $(C_nH_{2n+1}NH_3)_2CuCl_4$ and $CH_3NH_3SnX_3$ series.

The optical transmittance of the films was recorded using the unpolarized light generated by a set of lamps, by a JASCO V-530 dual beam scanning spectrophotometer in the energy range 1.1–6.5 *eV*. The surrounding medium was air and all the measurements were performed at room temperature. Transmittance is related to the absorption coefficient α by the relation:

$$T = \frac{(1-R)^2}{1-R^2} e^{-\alpha d} \tag{3.1},$$

where d is the thickness of the sample, T is the transmittance, and R is the reflectance.

From (3.1), α was estimated in low reflection approximation R ≈ 0 using the formula:

$$\alpha = \frac{1}{d} \ln(1/T) \tag{3.2},$$

where the quantity $\ln(1/T)$ is called "absorbance".

The absorption coefficient of a crystalline solid obeys the following relationship [21]:

$$(\alpha \cdot h\nu) \propto (h\nu - E_g)^r \tag{3.3},$$

where E_g is the optical energy gap, and r is an exponent that characterizes the optical absorption process. For direct allowed transition, $r = 1/2$; for direct forbidden transition $r = 3/2$; for indirect allowed transition $r = 2$; and finally for indirect forbidden transition $r = 3$.

The temperature dependence of the absorption coefficient has been measured installing a cool finger onto the spectrophotometer that allows, in vacuum, cooling of the sample down to 10 K.

3.2.a 3D systems

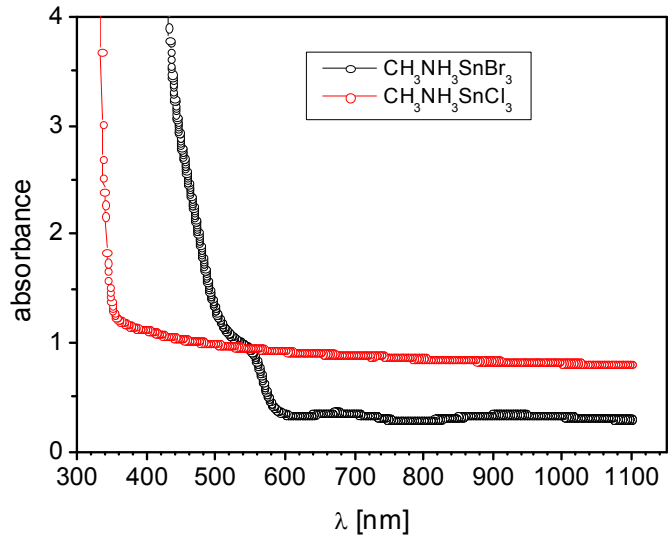

Figure 3.3 – *Room temperature absorption measurements of $CH_3NH_3SnX_3$ (with X = Cl and Br) films deposited on quartz substrates.*

Room temperature absorption spectra of $CH_3NH_3SnX_3$ (with X = Cl and Br) films are shown in **Figure 3.3**. Films of both compounds are deposited on quartz substrates by the SSTA technique. The spectra do not show evident excitonic resonances and the samples result to be transparent in the visible wavelength range with a sharp absorption edge in the UV for the chlorine compound and in the blue-green for the bromine compound.

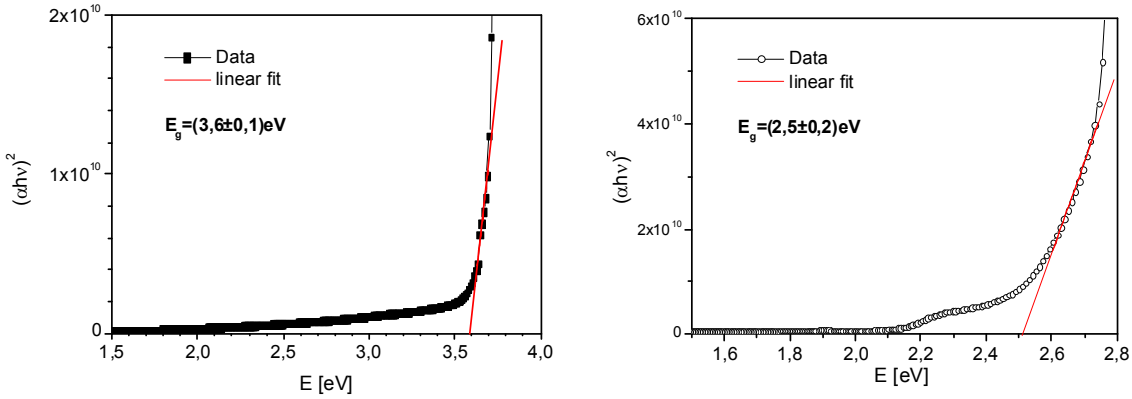

(a) **(b)**

Figure 3.4 – *Plots of $(\alpha \cdot h\nu)^{1/2}$ Vs. the energy E of* (a) *$CH_3NH_3SnCl_3$ and* (b) *$CH_3NH_3SnBr_3$ films. The linear fit in the more linear region of the absorption edge are in red.*

In $CH_3NH_3SnBr_3$ films spectra, a shoulder on the absorption edge was observed that indicates the presence of localized states into the gap, near to the valence band, probably due to defects or to excitonic charge transfer states. This effect was also present, though less pronounced, in $CH_3NH_3SnCl_3$.

The absorption coefficient has been estimated from the measurements using (3.2). Expression (3.3), for direct allowed transitions (exponent r = ½), can be written as:

$$y(E) = (\alpha \cdot E)^{1/2} = E - E_g \qquad (3.4).$$

In the region of the spectrum where $(\alpha \cdot E)^{1/2}$ is proportional to the energy E, a linear fit of the experimental data has been performed. In this way the values of the direct gap E_g = (2.5±0.2) eV for $CH_3NH_3SnBr_3$ and E_g = (3.6±0.1) eV for $CH_3NH_3SnCl_3$ films were estimated (**Figure 3.4**). It is interesting to observe that the direct gap decreases along the $CH_3NH_3SnX_3$ series Cl → Br → I, i.e. with the increase of the halogen ionic radii in the structure (**Figure 3.5**).

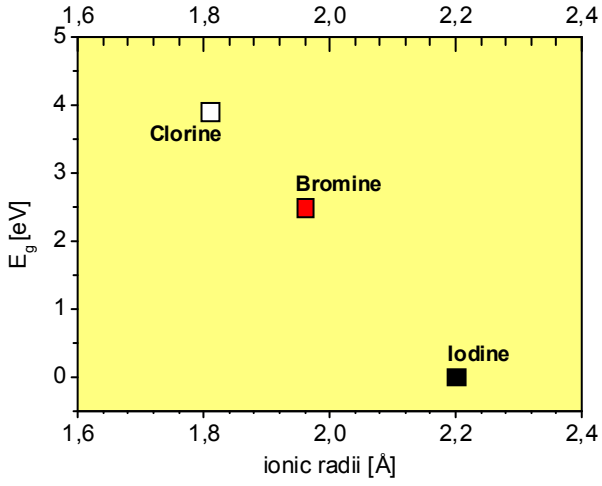

Figure 3.5 – *Correlation between direct energy gap (E_g) and ionic radii of halogen atoms in the structure of $CH_3NH_3SnCl_3$, $CH_3NH_3SnBr_3$, and $CH_3NH_3SnI_3$ films. For iodine compound that have metallic temperature behavior* [22] *it has been assigned E_g=0.*

3.2.b Layered systems

Absorption spectra and electronic configurations in the range of visible and UV wavelength have been studied in the SSTA deposited films of the 2D layered series compounds $(C_nH_{2n+1}NH_3)_2CuCl_4$ with n = 1,2,3,4. All the measured films were deposited on quartz substrates that result to be transparent in the optical range (190-1100 *nm*). Room temperature absorption spectra of the series are shown in **Figure 3.5**. All the films were transparent in the visible range and exhibited two absorption peaks in the near the UV region (at approximately 380 and 280 *nm*) and one in the near IR region (at approximately 730 *nm*) (**Figure 3.5 (b)**). These absorptions were extensively studied in powders [23] and in single crystals [24], and were recently confirmed in $(C_4H_9NH_3)_2CuCl_4$ films [25].

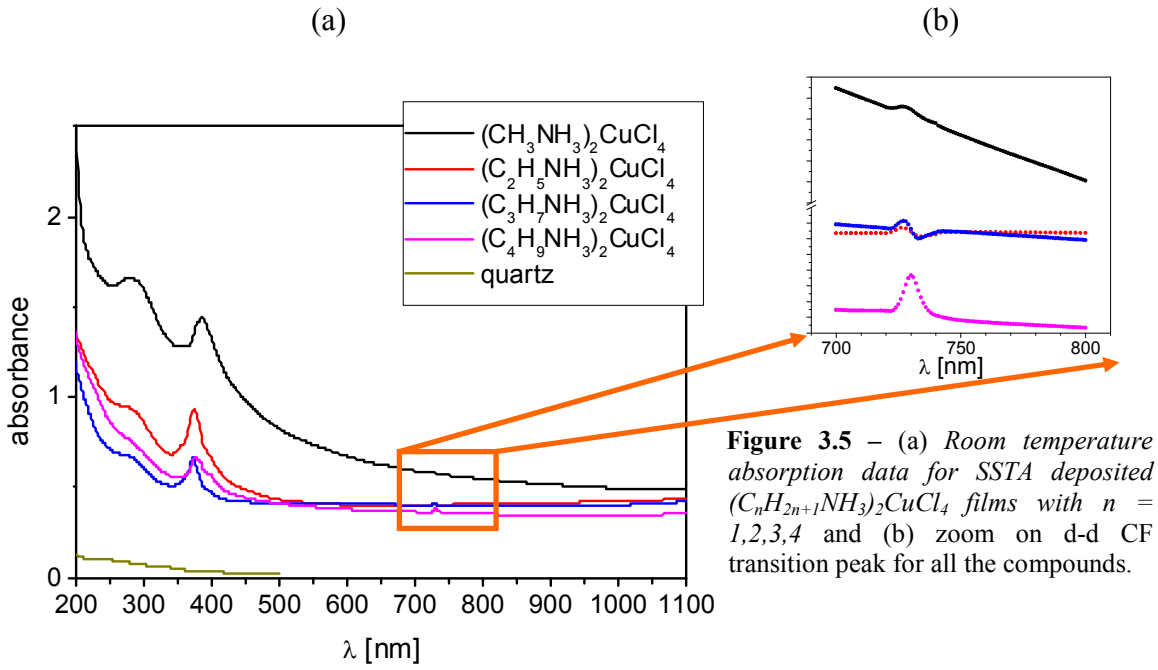

Figure 3.5 – (a) *Room temperature absorption data for SSTA deposited* $(C_nH_{2n+1}NH_3)_2CuCl_4$ *films with n = 1,2,3,4* and (b) zoom on d-d CF transition peak for all the compounds.

Typically in octahedral complexes the HOMO and LUMO levels are separated by crystal field effect. In the case of a Cu^{2+} complex, another splitting of degenerate electronic levels occurs due to strong Jahn-Teller effect (**Figure 3.6**). Transitions between *d* metal levels are called *d-d* crystal field (CF) transitions, while transition between ligants and *d* metal levels are called charge transfer (CT) transitions. In the case of figure 3.6 the IR band was attributed to the electronic $d_{xy} \rightarrow d_{x^2-y^2}$ transition [26]. The two UV bands were assigned to charge transfer (CT) transitions occurring in the axially elongated $CuCl_6^{4-}$

octahedron. In particular, the 380 *nm* band was claimed to correspond to the $\pi \rightarrow d_{x^2-y^2}$ ($e_u \rightarrow b_{1g}$) transition and the 280 *nm* one to the $\sigma \rightarrow d_{x^2-y^2}$ transition [26,27]. In previous reports [24,25,26,28] the UV transitions were described as "broad", with typical half-width at middle height of 40 *nm* [28], probably containing more than one transition [26].

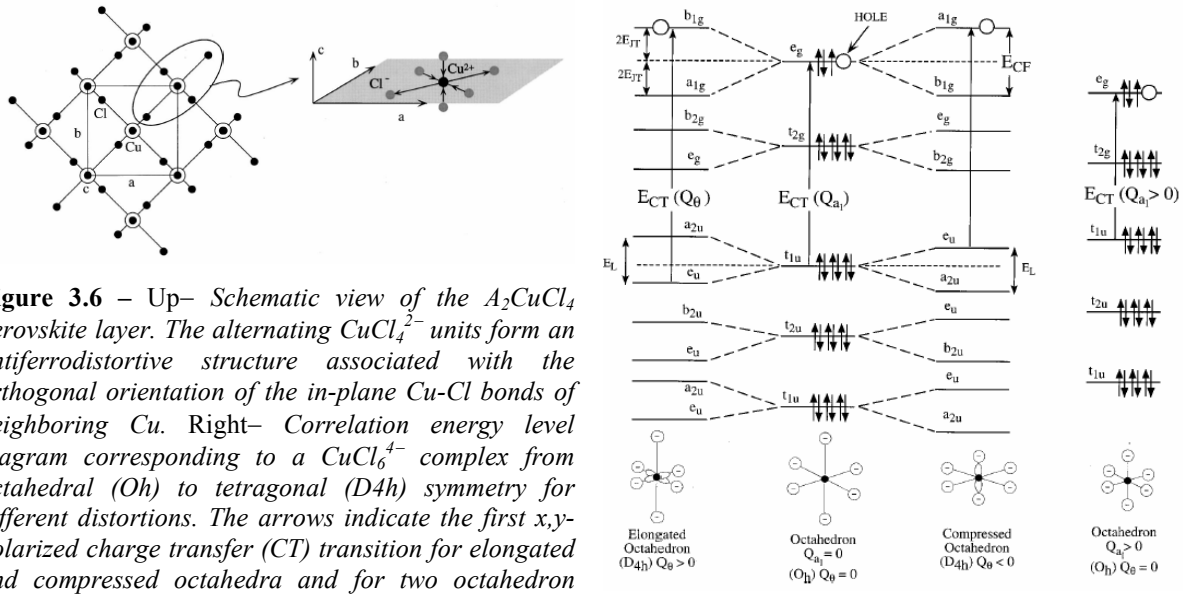

Figure 3.6 – Up– *Schematic view of the A_2CuCl_4 perovskite layer. The alternating $CuCl_4^{2-}$ units form an antiferrodistortive structure associated with the orthogonal orientation of the in-plane Cu-Cl bonds of neighboring Cu.* Right– *Correlation energy level diagram corresponding to a $CuCl_6^{4-}$ complex from octahedral (Oh) to tetragonal (D4h) symmetry for different distortions. The arrows indicate the first x,y-polarized charge transfer (CT) transition for elongated and compressed octahedra and for two octahedron geometries. The $4E_{JT}$ and E_L energies correspond to the splitting of the octahedral mainly Cu^{2+} a_g (x^2-y^2, $3z^2-r^2$) orbitals and the mainly Cl^- t_{1u} orbitals.*

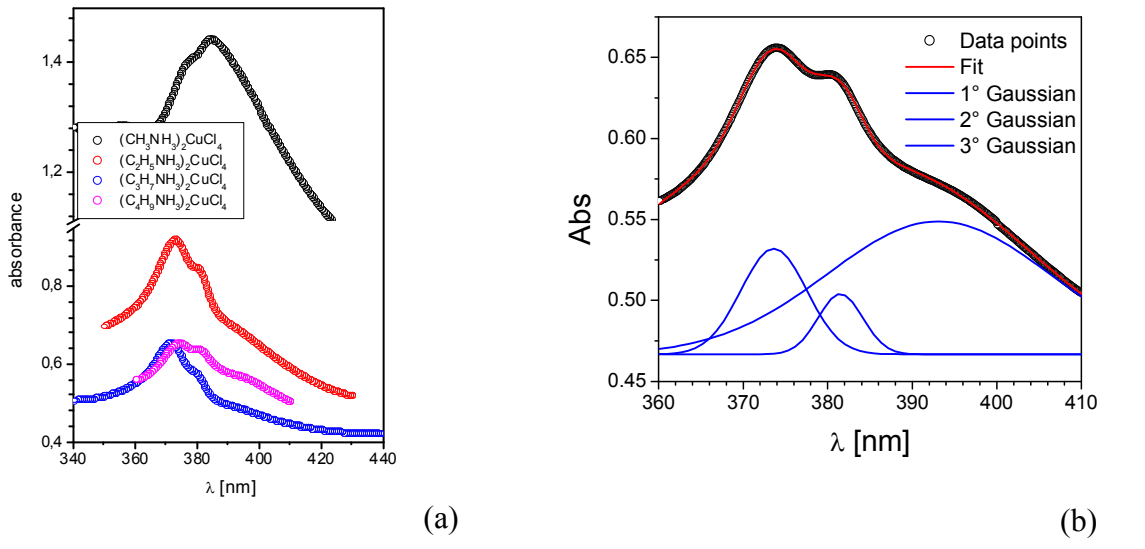

(a) (b)

Figure 3.7 – (a) *Enlargement of 380 nm band that correspond to the $\sigma \rightarrow d_{x^2-y^2}$ CT transition for all the compounds of $(C_nH_{2n+1}NH_3)_2CuCl_4$ series.* (b) *$(C_4H_9NH_3)_2CuCl_4$ data have been well fitted by multiple Gaussians (two peaks and a shoulder are evident).*

We observed that the absorption $\pi \rightarrow d_{x^2-y^2}$ transition contains more superimposed peaks (**Figure 3.7**) and results to be more narrow and defined in respect to previous works on powders or single crystal [24,25,26,29]. The improved resolution of the absorbance spectra in respect to the literature ones is due to the higher quality of the films obtained by single source thermal ablation deposition technique [30].

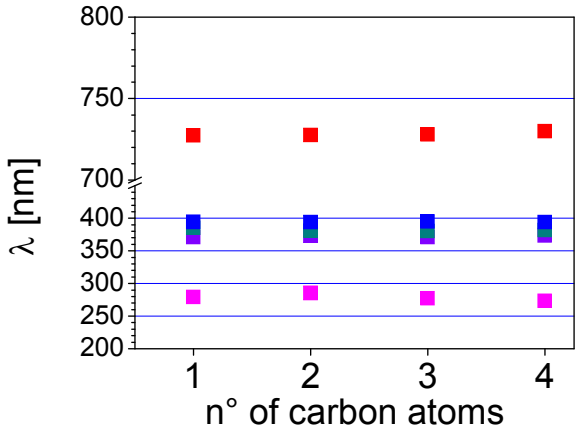

Figure 3.8 – *Wavelength of UV and NIR absorption peaks Vs. content of carbon atoms, from room temperature absorption analysis of* $(C_nH_{2n+1}NH_3)_2CuCl_4$ *films.*

The presence of more than one peak in the CT band is consistent with the fact that the hybrid compounds are orthorhombic, with D_{2h} symmetry [31,23]. The two-fold degeneracy of the e_u level is resolved in the D_{2h} geometry and three absorption peaks are expected. The absorbance spectra are consistent with literature results, confirming that the films have good structural and optical quality. The complex shape of the bands makes difficult to precisely determine the position and the relative intensity of each peak. However the fitting of the data indicates that their position is independent of the ammine chain length (**Figure 3.8)**.

To clarify this point, absorption measurements at different temperature were carried out. In fact at low temperatures it is possible to observe absorption spectra features without thermal broadening. Two sharp (375 *nm* and 383 *nm*) and one broad (≈ 365 *nm*) absorption peaks have been observed (**Figure 3.9**). Differently from the already discussed lead(II) compounds, in the case of copper(II) chloride hybrid materials, there is no evidence of structural transitions from room temperature to low temperature, as reported in the

literature [32]. Only a typical Stokes red shift of the peaks of the $\pi \rightarrow d_{x^2-y^2}$ transition complex is observed by cooling the sample (**Figure 3.9**). The splitting energy of the doublet structure in CT ($\pi \rightarrow d_{x^2-y^2}$) complex is 0.08 *eV*, which is the same magnitude as the spin-orbit splitting of a chlorine atom.

At low temperature it is confirmed the substantial independence of the position of the peaks changing the alkyl chain length. This is due to decoupling between the perovskite layers due to the larger HOMO-LUMO bandgap of the inorganic layers in respect to the perovskite ones.

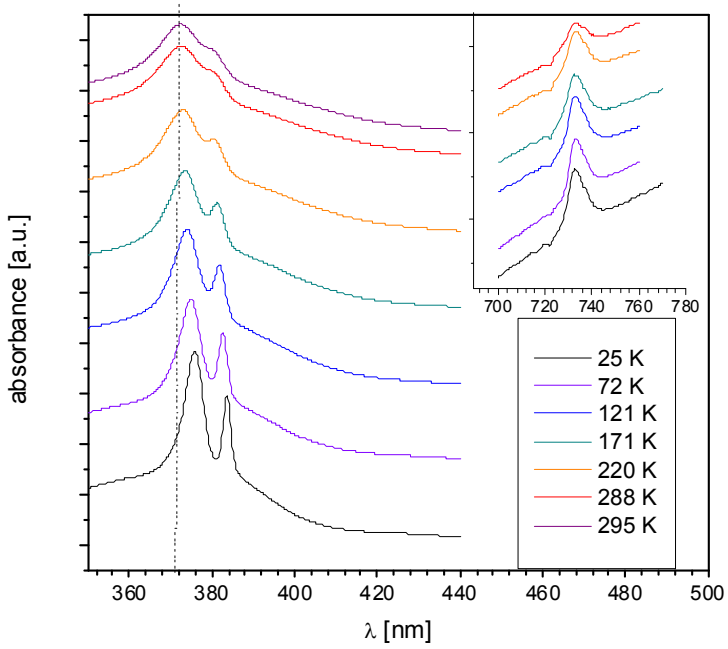

Figure 3.9 – *Temperature behavior of the absorption spectra of $(C_3H_7NH_3)_2CuCl_4$ film. Around 380 nm where are located the band that correspond to the $\sigma \rightarrow d_{x^2-y^2}$ CT transition. At low temperature the spectra show two narrow peaks and a broad one. In the inset it is shown the d-d transition peak for the different temperatures. Dashed line is only a guide for the eye, to highlight the shift in the spectral feature positions.*

3.3 Photoluminescence measurements on films of the $(C_nH_{2n+1}NH_3)_2CuCl_4$ and $CH_3NH_3SnX_3$ series

Photoluminescence measurements have been performed on films of the $(C_nH_{2n+1}NH_3)_2CuCl_4$ and $CH_3NH_3SnX_3$ series, to confirm that the observed resonance in the absorption spectrum was to be related to excitonic states. The photoluminescence was stimulated by a He-Cd laser with an excitation wavelength λ_{ex}=326 *nm* and the emission spectra were analyzed in the UV-visible wavelength range with a monochromator and a photomultiplier. Temperature was controlled by mounting the sample onto a cryocooler system equipped with quartz windows. The measurement temperature range was 10-350 *K*.

3.2.a 3D systems

Low temperature photoluminescence measurements on $CH_3NH_3SnBr_3$ films have not shown any relevant emission in the UV visible spectrum.

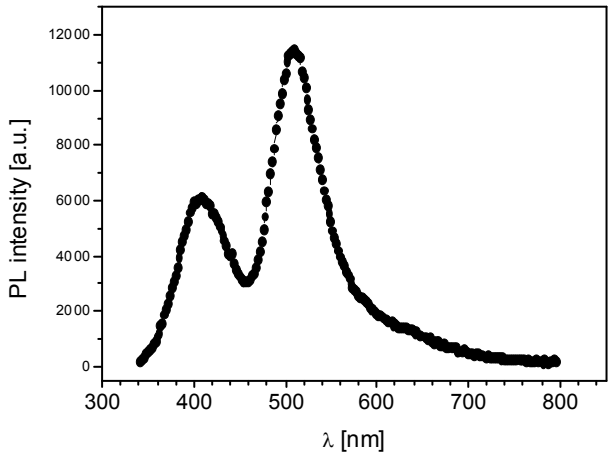

Figure 3.10 – *Photoemission spectra at 10 K of a film of $CH_3NH_3SnCl_3$ compound. Two intense and broad peaks (100 nm large) are observed.*

Absorption and photoluminescence spectra were measured by varying the sample temperature in the 10-300 K range. A strong luminescence emission was observed at low

temperature in $CH_3NH_3SnCl_3$. The emission spectrum presents two peaks at 400 nm and 520 nm (**Figure 3.10**). At these wavelengths the absorption spectra do not show any relevant feature. The emission peaks are intense and broad and the presence of similar features in the photoluminescence spectra of layered $(C_4H_9NH_3)_2SnCl_4$ compounds [25], probably indicates that they do not have an excitonic nature, but that are possibly due to defects acting as emitting centers.

3.2.b Layered systems

The possibility that the strong peaks in the absorption spectra can be due to excitonic states with strong binding energy, as for hybrid lead(II) compounds, has been tested by photoluminescence measurements.

Sharp and symmetric excitonic emission peaks (**Figure 3.11**) were found at about 384 *nm* for all the films of the $(C_nH_{2n+1}NH_3)_2CuCl_4$ family. As shown in the inset of **Figure 3.11**, the emission wavelength does not change along the series. The slight difference between absorption and photoemission wavelength may be ascribed to the re-adsorption of light corresponding to the higher-energy-side in the luminescence band. However which is the absorption peak of the $\pi \rightarrow d_{x^2-y^2}$ CT transition complex, responsible for photoluminescence is still debated. As in absorption measurements, a strong emission has been obtained for the ethyl-compound $(C_2H_5NH_3)_2CuCl_4$. This is probably due to a greater stability of this compound in respect to the others of the family that are typically hygroscopic [31]. The temperature behavior of a sample of the ethyl-compound is shown in **Figure 3.12 (a)**. The emission is present up to room temperature. It is important also to consider that in this measurements the deterioration of the film due to irradiation is not negligible in the analyzed temperature range. The little red-shift of about 4 *nm* is due to Stokes shift in the absorption spectra.

In **Figure 3.12 (b)** the logarithm of the photoluminescence peak intensity is plotted as a function of the inverse of the temperature. The photoluminescence efficiency remains almost constant up to 80 *K* and at temperatures higher than 120 *K* it decrease as $\exp(E_a/k_BT)$ with an activation energy $E_a = (530 \pm 80)\ meV$. As reported by Ishihara et al.

[5,8] on lead(II) hybrid compound family, this activation energy could be regarded as the exciton binding energy.

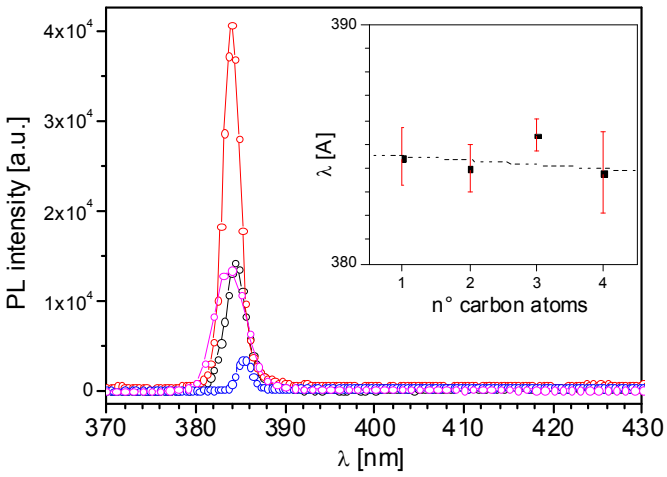

Figure 3.11 – *Photoluminescence intensity at 10 K of $(C_nH_{2n+1}NH_3)_2CuCl_4$ films with n=1 (black), 2 (red), 3 (blue), and 4 (magenta).In the inset is plotted the emission wavelength of the PL peaks for the different n value, where n is the number of carbon atoms that compose the alkyl chain in the structure. Dot line is only a guide for the eye.*

(a) (b)

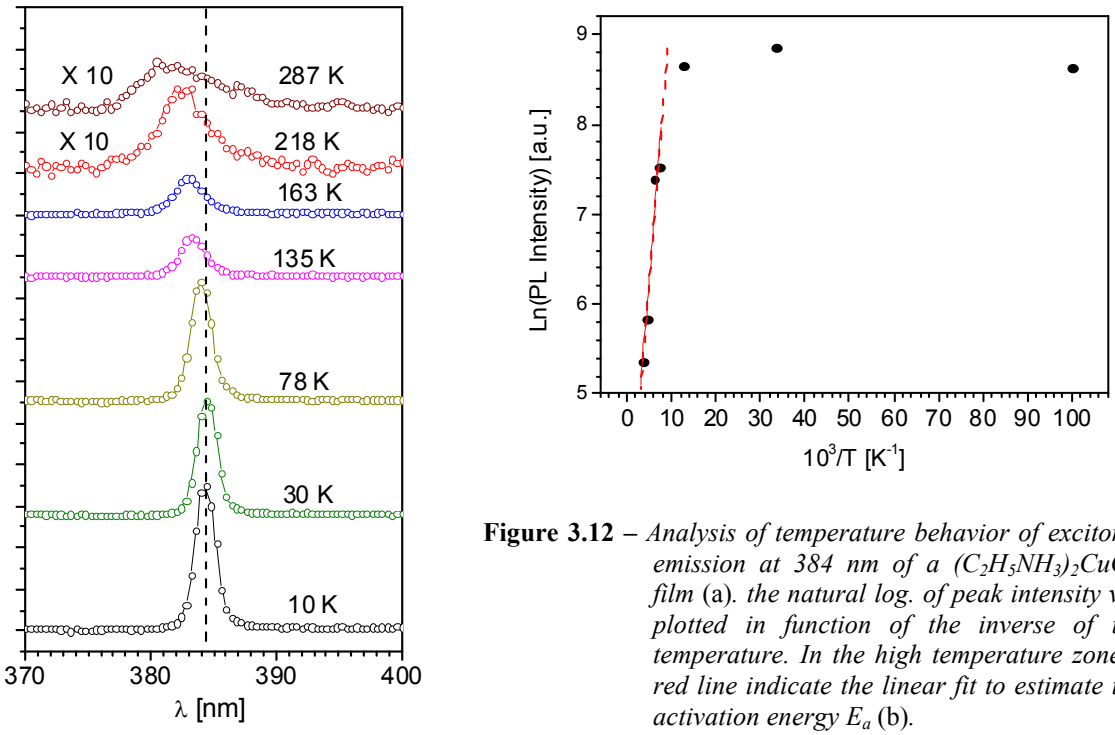

Figure 3.12 – *Analysis of temperature behavior of excitonic emission at 384 nm of a $(C_2H_5NH_3)_2CuCl_4$ film* (a). *the natural log. of peak intensity vas plotted in function of the inverse of the temperature. In the high temperature zone a red line indicate the linear fit to estimate the activation energy E_a* (b).

3.4 Organic-Inorganic Light Emitting Diode (OILED)

A great interest exists in the world of electro-optic technologies (solar cells, active displays, semiconductive LASER, optical-electronic signal transducers and so on) on new organic semiconducting materials. In particular, an increasing research effort has followed the discovery of efficient electroluminescence in organic and conjugated polymer thin films [33]. **Figure 3.13** shows the dramatic increase in luminescence efficiency of light-emitting molecular solids and polymers compared to typical inorganic LEDs over a 15-year time scale (blue, yellow, and green lines in **Figure 3.13**). Pioneering work was done at Eastman Kodak in 1987 on evaporated small molecules [33] and at Cambridge University in 1990 on solution-processed semiconductive polymers [34]. Currently, the highest observed luminous efficiencies of derivatives of these materials exceed that of incandescent light-bulbs, thus eliminating the need for the backlight that is used in AMLCDs. Reviews of different aspects of the field of OLEDs are available, including studies on electroluminescent materials [35] and device physics and engineering [36].

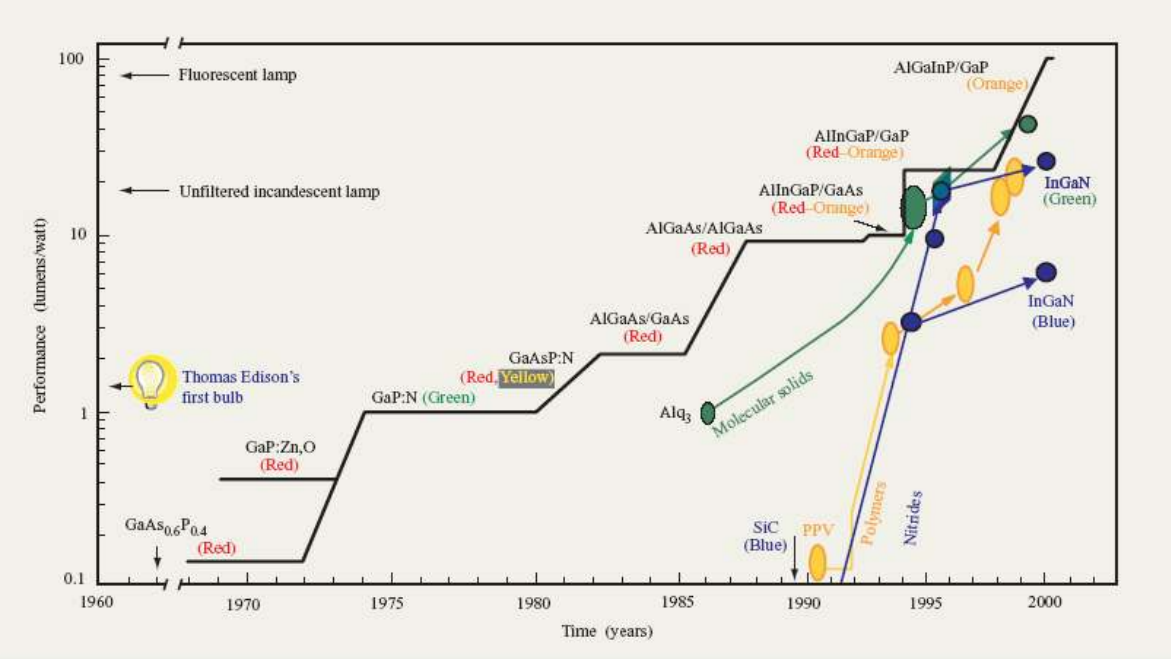

Figure 3.13 – *Evolution of LED/OLED performance* [36].

Evidence of the considerable progress that has been made in the field is that flat-panel displays based on OLEDs are appearing on the market. Major challenge remain, however, including the necessity to significantly improve the performance and lifetime of OLEDs. In fact they are double charge injection devices, requiring the simultaneous supply of both electrons and holes to the electroluminescent (EL) material sandwiched between two electrodes (**Figure 3.14**). To achieve an efficient OLED with the single-layer configuration the organic EL material would ideally have a high luminescence quantum yield and should be able to facilitate injection and transport of electrons and holes. This demand of multifunctional capabilities from a single organic material is a very difficult one to achieve by most current materials.

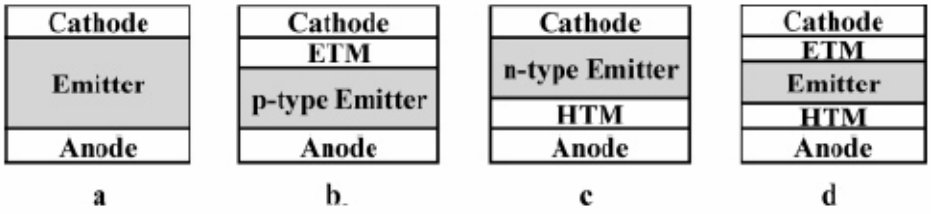

Figure 3.14 – *Common OLED architectures with a hole-transport material (HTM) and an electron-transport material (ETM).*

Organic materials with good emitting properties are in fact typically "one carrier" type semiconductors. In order to improve device performance, generally it is required the use of two or more different materials to perform the functions of efficient light emission and good electron- and hole-injection and transport properties in OLEDs. This requires in turn a more complex architecture as the multilayered device structure shown in **Figure 3.14 (b)-(d)**.

The possibility to utilize a single compound as emitter and charge transport material can also make possible to realize a LET (Light Emitting Transistor) device that dramatically simplifies the driving circuitry of active displays [37].

The good optical properties of organic-inorganic perovskite based compounds make them interesting and competitive as alternative materials to organic molecular solids and polymers in LED device technology. In this framework Era et al. [38] have created a first organic-inorganic electroluminescent device (OILED), with architecture typical of standard OLEDs (**Figure 3.15**).

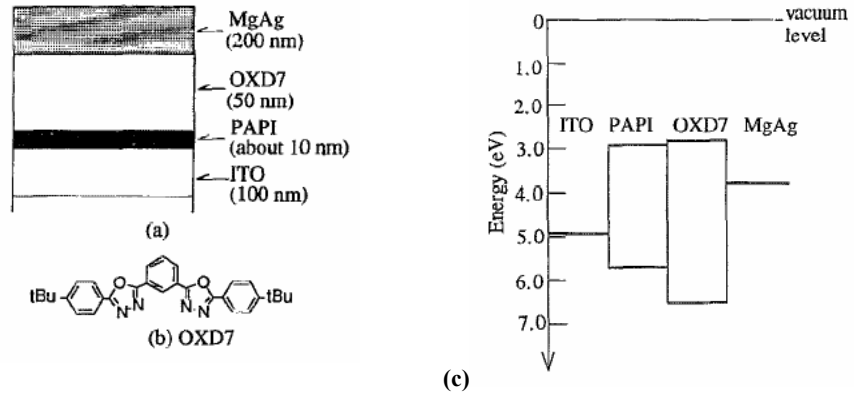

Figure 3.15 – *Era organic-inorganic heterostructure EL device using a $(C_6H_5C_2H_4NH_3)_2PbI_4$ (colled PAPI by authors) spin-coated film* (a)*, molecular structure of an oxadiazole derivative OXD7* (b) *and energy diagram of ITO/PAPI/OXD7/MgAg device* (c)*.*

This device consists of an indium tin oxide (ITO) anode, a $(C_6H_5C_2H_4NH_3)_2PbI_4$ emitter layer, an oxadiazole derivate (OXD7) as electron transport (hole blocking) layer, and a MgAl cathode. The latter two layers are vacuum evaporated. Recombination is expected to take place when the injected electrons encounter the confined holes in the $(C_6H_5C_2H_4NH_3)_2PbI_4$ layer. At low temperature (77 K) an intense (15.7 *lumens/watt*) green luminescence occurs, comparable with that reported for organic and inorganic based devices (see **Figure 3.13**). Device electroluminescence shows a spectrum very similar to the photoluminescence spectrum of $(C_6H_5C_2H_4NH_3)_2PbI_4$, but as for photoluminescence, emission quenches with temperature increase. To bolster luminescence efficiency up to room temperature, one needs to stabilize the exciton in the structure. To make that, several organic cations have been examined within the lead(II)-iodine framework since the dielectric constant of the organic layer influences the thermal stability of the exciton [39].

Recently Mitzi et al. have incorporated a oligothiophene derivative molecule [5,5"'-bis(aminoethyl)-2,2':5',2":5",2"'-quaterthiophene (AEQT)], within a layered perovskite framework of PbX_6^{4-} octahedral (with X= Cl, Br, and I) (see **Figure 1.18 (a)**) to form the new hybrid series of compound $C_{20}H_{22}S_4N_2PbX_4$ [40]. This molecule acts as a chromophore and the material shows the characteristic exciton absorption resonance associated with the inorganic perovskite sheets, superimposed to the absorption spectrum of the chromophore. In contrast, the photoluminescence spectrum exhibits no emission from the inorganic exciton state but only from AEQT one. In particular, for X = Cl, a strong photoluminescence is observed. The AEQT luminescence is progressively quenched across

the X = Cl → Br → I series, as the bandgap of the inorganic framework decreases in energy compared to the HOMO–LUMO gap of the chromophore molecule. This quenching is associated with energy transfer and/or charge separation between the organic and inorganic components of the structure [40]. $C_{20}H_{22}S_4N_2PbCl_4$ has been utilized as emitter material in a LED device [41] (**Figure 3.16**). Also in this case, OXD7 has been employed as electron transport (hole blocking) layer. Bright green-yellow light (λ_{max} 530 *nm*) was observed in a well-lit room when the devices were forward-biased under ambient conditions. A low turn-on voltage of about 5.5 *V* was observed. The maximum efficiency was 0.1 *lumens/watt* at 8 *V* and 0.24 *mA* (power conversion efficiency 0.11%). Interestingly, even with the thicker films, the turn-on voltage remained relatively low.

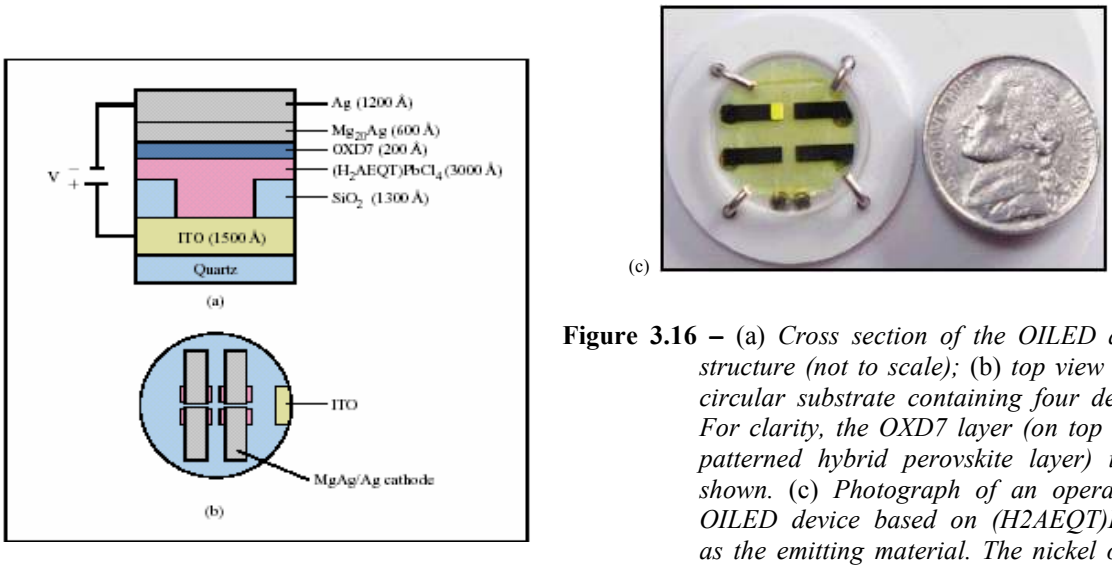

Figure 3.16 – (a) *Cross section of the OILED device structure (not to scale);* (b) *top view of the circular substrate containing four devices. For clarity, the OXD7 layer (on top of the patterned hybrid perovskite layer) is not shown.* (c) *Photograph of an operational OILED device based on (H2AEQT)PbCl4 as the emitting material. The nickel on the right provides a scale for size comparison .*

The devices discussed above are based on the concept of simple substitution of organic emitter material with the hybrid ones, while hybrid materials can perform new functionalities as proposed by Takada with his CuPc/TiO_x heteromultilayer compound [42]. In principle however, the intrinsic layered structure of 2D hybrids, added to self-assembling properties, can lead to the possibility to design and synthesize an emitter material with the capability to control electron/hole drain and separation.

Bibliography

[1] D. B. Mitzi, D. R. Medeiros, and P. R. L. Malenfant, *Inorg. Chem.*, **41**, 2134 (2002).

[2] Ri-Zhu Yin and Chul Hyun Yo, *Bull. Korean Chem. Soc.*, **19**, 947 (1998).

[3] T. Tsuboi, A. Matsubara, K. Koto, K. Iio, and B. Henderson, *Phys. Status Solidi B*, **188**, K35 (1995).

[4] D. B. Mitzi and K. Liang, *Chem. Mater.*, **9**, 2990 (1997).

[5] T. Ishihara, J. Takahashi, and T. Goto, *Phys. Rev. B*, **42**, 11099 (1990).

[6] T. Ishihara, T. Ogawa, and Y. Kanemutsu, *Optical Properties in Low-Dimensional Materials*, Eds. World Scientific, Singapore, p. 228 (1995).

[7] M Shinada, and S. Sugano, *J. Phys. Soc. Jpn.*, **21**, 1936 (1966).

[8] X. Hong, T. Ishihara, and A. V. Nurmikko, *Phys. Rev. B*, **45**, 6961 (1992).

[9] E. Hanamura, N. Nagaosa, M. Kumagai, and T. Takagahara, *Mater. Sci. Eng. B*, **1**, 255 (1988).

[10] D. B. Mitzi, K. Chondroudis and C. R. Kagan, *IBM J. Res. & Dev.*, **45**, N°1 (2001).

[11] D. B. Mitzi, *Chem. Mater.*, **8***,* 791 (1996).

[12] T. Ishihara, M. Hirasawa, and T. Goto, *Jpn. J. Appl. Phys. Suppl.*, **34-1**, 71 (1995).

[13] S. Wang, D. B. Mitzi, C. A. Feild, and A. Guloy, *J. Am. Chem. Soc.*, **117**, 5297 (1995).

[14] X. Hong, T. Ishihara, and A. V. Nurmikko, *Solid State Comm.*, **84**, 657 (1992).

[15] R. D. Willett, J. A. Haugen, J. Lebsack, and J. Morrey, *Inorg. Chem.*, **13**, 2510 (1974).

[16] R. Kind, S. Plesko, P. Günter, J. Roos, and J. Fousek, *Phys. Rev. B: Condens. Matter*, **23**, 5301 (1981).

[17] J. Calabrese, N. L. Jones, R. L. Harlow, N. Herron, D. L: Thorn, and Y. Wang, *J. Am. Chem. Soc.*, **113**, 2328 (1991).

[18] C. Xu, T. Kondo, H. Sakakura, K. Kumata, Y. Takahashi, and R. Ito, *Solid State Comm.*, **79**, 245 (1991).

[19] W.-S. Fann, S. Benson, J. M. J. Madey, S. Etemad, G. L. Baker, and F. Kajzar, *Phys. Rev. Lett.*, **62**, 1492 (1989).

[20] J. Ishi, H. Kunugita, K. Ema, T. Ban, and T. Kondo, *Phys. Rev. B*, **63**, 073303 (2001).

[21] I. Watanbe, and T. Okumura, *Jpn. J. Appl. Phys.*, **25**, 1851 (1986).

[22] D. B. Mitzi, C. A. Feild, Z. Schlesinger, and R. B. Laibowitz, *J. Solid States Chem.*, **114**, 159 (1995).

[23] D. Abdellaziz, A. Thierr-Sorel, R. Perret, B. Chaillot, and J. E. Guerchais, *Bull. Soc. Chim. France*, **103**, 535 (1975).

[24] R. Valiente, and F. Rodriguez, *Phys. Rev. B*, **60**, 9423 (1999).

[25] C. Aruta, F. Licci, A. Zappettini, F. Bolzoni, F. Rastelli, P. Ferro, and T. Besagni, *Appl. Phys. A*, **81**, 963 (2005).

[26] R. D.Willett, O. L. Liles Jr., and C. Michelson, *Inorg.Chem.*, **6**, 1885 (1967).

[27] S. R. Desjardins, K. W. Penfield, S. L. Cohen, R. L. Musselman, and E. L. Solomon, *J. Am. Chem. Soc.*, **105**, 4590 (1983).

[28] L. L. Lohr Jr., and W. N. Lipscomb, *Inorg. Chem.*, **2**, 911 (1963).

[29] L. L. Lohr Jr., and W. N. Lipscomb, *Inorg. Chem.*, **2**, 911 (1963).

[30] F. Chiarella, A. Zappettino, P. Ferro, T. Besagni, F. Licci, A. Cassinese, M. Barra, R. Vaglio, and C. Aruta, *Cryst. Res. Technol.*, **40**, 1028 (2005)

[31] J. P. Steadman, and R. D. Willett, *Inor. Chim. Acta*, **4**, 367 (1970).

[32] I. R. Jahn, K. Knorr, and J. Ihringer, *J. Phys.: Condens. Matter.*, **1**, 6005 (1989).

[33] C. W. Tang, and S. A. Van Slyke, *Appl. Phys. Lett.*, **51**, 913 (1987).

[34] J. H. Burroughes, D. D. C. Bradley, A. R. Brown, R. N. Marks, K. Mackay, R. H. Friend, P. L. Burns, and A. B. Holmes, *Nature*, **347**, 539 (1990).

[35] M. T. Bernius, M.Inbasekaran, J. O'Brien, and W. Wu, *Adv. Mater.*, **12**, 1737 (2000). D. Y. Kim, H. N. Cho, and C. Y. Kim, *Prog. Polym. Sci.*, **25**, 1089 (2000).

[36] J. R. Sheats, H. Antoniadis, M. Hueschen, W. Leonard, J. Miller, R. Moon, D. Roitman, and A. Stocking, *Science*, **273**, 884 (1996).

[37] A. Hepp, H. Heil, W. Weise, M. Ahles, R. Schmechel, and H. von Seggern, *Phys. Rev. Lett.*, **91**, 157406 (2003).

[38] M. Era, S. Morimoto, T. Tsutsui, and S. Saito, *Appl. Phys. Lett.*, **65**, 676 (1994).

[39] T. Hattori, T. Taira, M. Era, S. Morimoto, T. Tsutsui, and S. Saito, *Chem. Phys. Lett.*, **254**, 103 (1996).

[40] D. B. Mitzi, K. Chondroudis, and C. R. Kagan, *Inorg. Chem.*, **38**, 6246 (1999).

[41] K. Chondroudis, and D. B. Mitzi, *Chem. Matter.*, **11**, 3028 (1999).

[42] J. Takada, H. Awaji, M. Koshioka, A. Nakajima, and W. A. Nevin, *Appl. Phys. Lett.*, **61**, 2184 (1992).

Chapter 4

Transport properties and applications

4.1 Transport properties

In the last 15 years the interest in the organic-inorganic perovskite structures extended to the study of electronic and transport properties. Initially the interest was mostly addressed to insulating systems which exhibited interesting structural transitions, low dimensional magnetism, and luminescence properties. Measurement on single crystals of $(NH_3C_2H_4NH_3)_2CuX_4$ (X=Cl and Br) and $(C_2H_5NH_3)_2CdCl_4$ indicated that these salts are good magnetic insulators ($\rho = 10^{12}\ \Omega \cdot cm$) at low temperature and, as the temperature increases, they behave as ionic (probably protonic) semiconductors [1].

The possibility of substantial electronic conductivity in organic-inorganic perovskites was first realized in the 3D system $CH_3NH_3SnX_3$ that belong to the cubic perovskite organic-inorganic class with the generic formula $CH_3NH_3MX_3$.

Lately, it was found that the iodine compound (X = I) exhibits a black coloration and a metallic character over the entire range 1.8-325 *K* , while the bromine compound (X = Br) exhibit red coloration and semiconducting character [2,3,4,5]. Electrical transport analysis of the metallic hybrid methylammonium tin(II) iodine compound demonstrates that it is a low carrier density *p*-type metal with a room temperature resistivity of 3 $m\Omega \cdot cm$ and a quite large Hall mobility, 50 $cm^2 V^{-1} s^{-1}$ (at room temperature) [3]. Moreover the compounds with $NH_2CH{=}NH_2SnI_3$ were also synthesized, where the organic component (formamidinium cation) in the structure has a larger dimension in respect to the methylammonium one. The $NH_2CH{=}NH_2SnI_3$ has a 1,2% larger cubic lattice parameter and a higher semimetallic resistivity temperature profile than that of the isostructural methylammonium analogous compound [6] with an increase of room temperature resistivity probably due to the increase in the Sn–I bond length.

A band structure calculation for these systems has been proposed by Mitzi et al. to explain why these unusual halide are good electrical conductors [7]. The metallic character results from the large dispersion of the Sn(5s) orbitals hybridized with I(5p) orbitals along the <111> direction of the cubic Brillouin zone (R-point), leading to a marginal crossing of Sn(5s) and Sn(5p) bands.

If the cubic symmetry is broken, for example by cutting a 2D sheet from the 3D structure, a progressively larger band gap between the Sn(5s) and Sn(5p) bands would be expected. This has been experimentally observed by Mitzi and reported in his works [7,8]. As for the analogous inorganic oxide-based perovskite layered family, metal-semiconductor transition have been observed as a function of the perovskite layer thickness. The <100> and <110> oriented perovskite families, $(C_4H_9NH_3)_2(CH_3NH_3)_{n-1}Sn_nI_{3n+1}$ and $[NH_2C(I){=}NH_2]_2(CH3NH_3)_nSn_nI_{3n+2}$ are the first examples of conducting layered organic-inorganic halides that enable an examination of the electrical transport properties as a function of the dimensionality of the metal halide framework (**Figure 4.1**) [6,7,8]. In these series of compounds the room temperature resistivity increases dramatically with decrease of the perovskite sheet thickness. For example in the $(C_4H_9NH_3)_2(CH_3NH_3)_{n-1}Sn_nI_{3n+1}$ series, the resistivity changes with

continuity from 10^{-2} Ω ·*cm* in $CH_3NH_3SnI_3$ ($n \rightarrow \infty$), to 10^5 Ω ·*cm* in $(C_4H_9NH_3)_2SnI_4$ (n = 1) [8]. It is interesting to node the correlation between the structural properties of the perovskite layers and the electrical transport properties in these layered hybrids. In particular the trend observed in tin(II) iodide series, is that the resistivity increases with the decrease of the number of perovskite sheets in the inorganic layer, corresponding to an increased distortion of the SnI_6^{4-} octahedra and of the average Sn–I bond length [9].

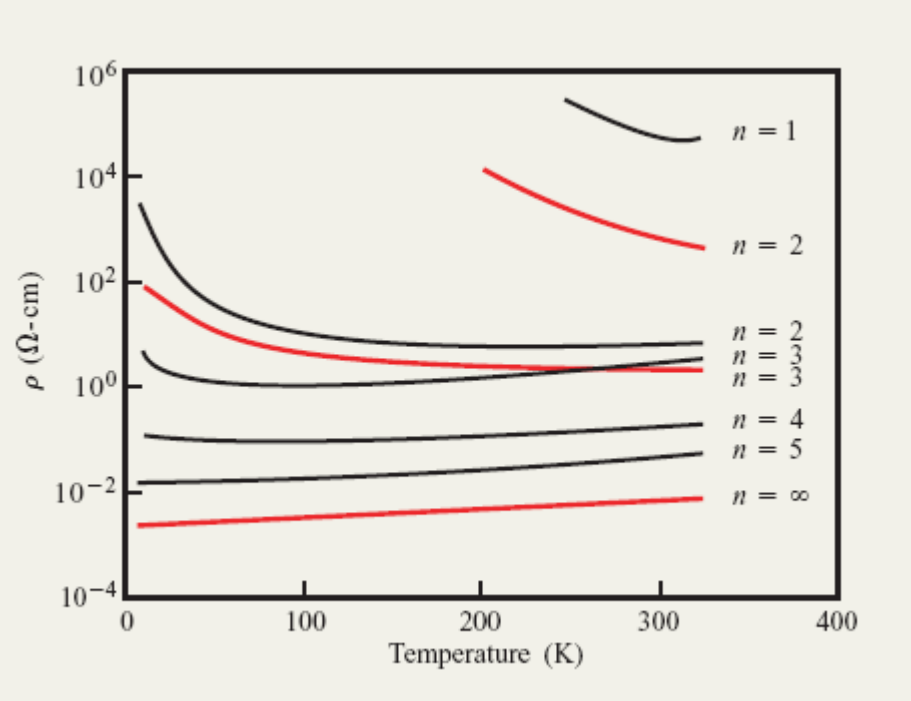

Figure 4.1 – *Resistivity (ρ) as a function of temperature for pressed pellet of the layered perovskite families $(C_4H_9NH_3)_2(CH_3NH_3)_{n-1}Sn_nI_{3n+1}$ (black curves) and $[NH_2C(I)=NH_2]_2(CH3NH_3)_nSn_nI_{3n+2}$ (red curves), as well as for the n → ∞ end-member of both families ($CH_3NH_3SnI_3$)* [10].

This correlation between structural and transport properties can be explained in terms of the Sn(5s) non-bonding electrons. In fact in the less conductive system, increasing the structural distortion corresponds to a growing of the stereochemical activity of the Sn(5s) lone pair that act as a new bond that breaks the conduction efficiency of the I–Sn–I bridges.

In the pseudo-cubic structure of the class $CH_3NH_3MX_3$, the negative charge is localized on the halogen atoms, and the $CH_3NH_3^+$ cation occupies the center of the cubic cell. In the lead compound $CH_3NH_3PbX_3$ (X=Cl, Br, I), as an example, nuclear magnetic resonance (NMR) and nuclear quadrupolar resonance (NQR) demonstrate that the $CH_3NH_3^+$ cations

at room temperature undergo a fast isotropic reorientation [11]. A similar situation is expected for metilammonum tin(II) halides. The X–Sn–X–Sn bonding configuration of the linear chain that composes the cubic perovskite structure is symmetric in the high temperature cubic phase (like in the $KSnBr_3 \cdot H_2O$ and $CsSnI_3$ compounds), but becomes asymmetric (X····Sn-X····Sn) with decreasing temperature, causing several phase transitions [5] and favoring electron localization and the formation of a large gap in the band structure. However, this deformation due to the frozen of the rotational degree of freedom of the molecular cation, may give raise to some interesting phenomena, such as piezoelectric or ferroelectric behavior. Furthermore, it is interesting that two different types of conductivity can occur in these perovskites, that is: the electronic and the ionic one.

The organic components of the hybrid compounds were initially considered to have only a structural role. The organic cations were considered to function as structural stabilizers in the perovskite and, thanks to the weak π–π bond, hydrogen or van der Waals interactions between the molecules, they guarantee mechanical flexibility to the structure. In respect to the transport properties, they had the role of spacers, to electronically decouple the inorganic perovskite layers. Obviously these concepts could be completely reversed considering the inorganic cage as a rigid, ordered and thermally stable structure in which to locate the organic cations. In this way it would be possible to tune the coupling between conjugated oligomers, for example, by the change of some component in the inorganic structure.

These two visions can be mixed up to design new functions in more complex materials.

4.2 Resistivity and temperature behaviour

The resistance as a function of temperature and I-V current-voltage characteristics of the SSTA deposited films of both the $(C_nH_{2n+1}NH_3)_2CuCl_4$ and $CH_3NH_3SnX_3$ series, were measured by a standard two probes technique. Both the applied voltage and the current

were controlled by a Keithley 487 picoammeter. The electrical gold contacts (9 *mm* wide and 0.1 *mm* distant) were deposited by evaporating the metal through appropriate stencil-steel masks. A cryocooler system was used to change sample temperature from 320 *K* to low temperatures (10 *K*).

Room temperature resistivity values have been measured in air with a four contact van der Pauw configuration [12] using a Keithley 487 picoammeter to measure the current and a Keithley 7065 Hall card switching set in high resistivity mode.

For layered $(C_nH_{2n+1}NH_3)_2CuCl_4$ films, a systematic decay in the measured conductivity has been observed as a function of time. This may be caused by an irreversible change in the samples related to the charge flow as reported for analogous halide compounds $NH_3(CH)_2NH_3CuX_4$ [1]. This decay was observed in all the samples when exposed to air, with a significant decomposition at the anode. All this suggest that the conductivity is ionic and, considered the chemical composition of these compounds, most probably protonic. The strong activation of the degradation phenomena occurs when the samples are exposed to air, probably the degradation effect being accelerated by humidity. This is also consistent with the report by Glasser [13] on many similar compounds. Therefore the measurements are interpreted from the general Arrhenius law relevant to the diffusion in ionic crystals given by:

$$\rho(T) = AT\exp\left(\frac{\Delta E}{k_B T}\right) \qquad (4.1),$$

where A is a constant, ΔE is the activation or "hopping" energy, k_B the Boltzmann's constant and T the temperature.

3.2.a 3D systems

In **Figure 4.2** the resistance vs. temperature of $CH_3NH_3SnBr_3$ and $CH_3NH_3SnCl_3$ films is reported. The data were obtained by applying a 20 *V* voltage and the measurements were performed under vacuum ($P < 10^{-3}$ *mBar*). An accurate data acquisition was attained whilst slowly cooling the sample. Room temperature resistivity has been estimated under vacuum conditions to be $\rho = 0.52$ *MΩ·cm* and $\rho = 3$ *MΩ·cm*, for $CH_3NH_3SnBr_3$ and $CH_3NH_3SnCl_3$

films respectively. The obtained values are about ten times higher than the previously reported values (0.05 $M\Omega \cdot cm$ [14,2] and 0.4 $M\Omega \cdot cm$ [15]), which refer to DC measurements taken on pressed powders. Resistive data show an exponential dependence on temperature.

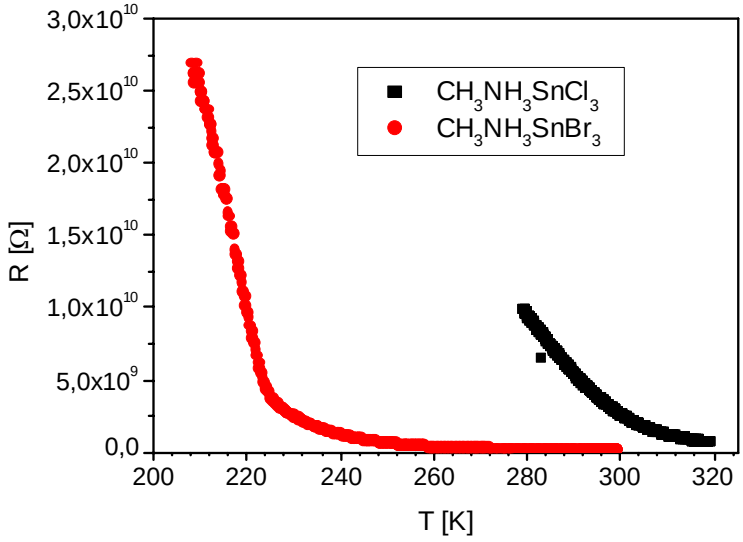

Figure 4.2 – *Resistance as a function of temperature for films of $CH_3NH_3SnCl_3$ (black points) and $CH_3NH_3SnBr_3$ (red points).*

In **Figure 4.3**, the resistivity data are reported in the Arrhenius plot form and the linear zones are fitted by applying relation (4.1). The presence of "knees" has been observed in both samples. In **Figure 4.3 (a)** is reported the Arrhenius plot in the 280-320 *K* temperature range for a $CH_3NH_3SnCl_3$ sample. The activation energy results to be of about 0.56 *eV*. In this temperature range it was observed a non-linear $\ln(\rho)$ increase with decreasing the temperature down to the instrumental limit. This non-linear temperature behaviour indicates, as proposed by Yamada [15], the presence of a continuous structural transition with order-disorder character around room temperature. Following Yamada indications, the different phases are indicatively reported in the plot. These phases (indicated as III, IV, and V) are referred to be non-cubic distorted perovskite phases. This compound, in fact, result to be cubic only above 450 *K*. In **Figure 4.3 (b)** is reported the Arrhenius plot in the 200-300 *K* temperature range for a $CH_3NH_3SnBr_3$ sample. The fitting in the 260-230 *K* interval gives an activation energy $\Delta E = (0.30 \pm 0.01)$ *eV*. Such a value is consistent with the activation energy reported in literature [14,2]. Two significant variations of slope are observed at about 225 and at 260 *K*. It seems reasonable to correlate the

discontinuity at 225 K to the structural transition at 229.4 *K* reported by Onoda-Yamamuro et al. on the basis of calorimetric analysis. This was described as an order-disorder transition and attributed to the orientational disorder of the $CH_3NH_3^+$ ion [2]. In this case, the phases indicated in the plot as I and II are the cubic phase and a strongly distorted perovskite phase, with to a drastic color change (red → yellow) [14].

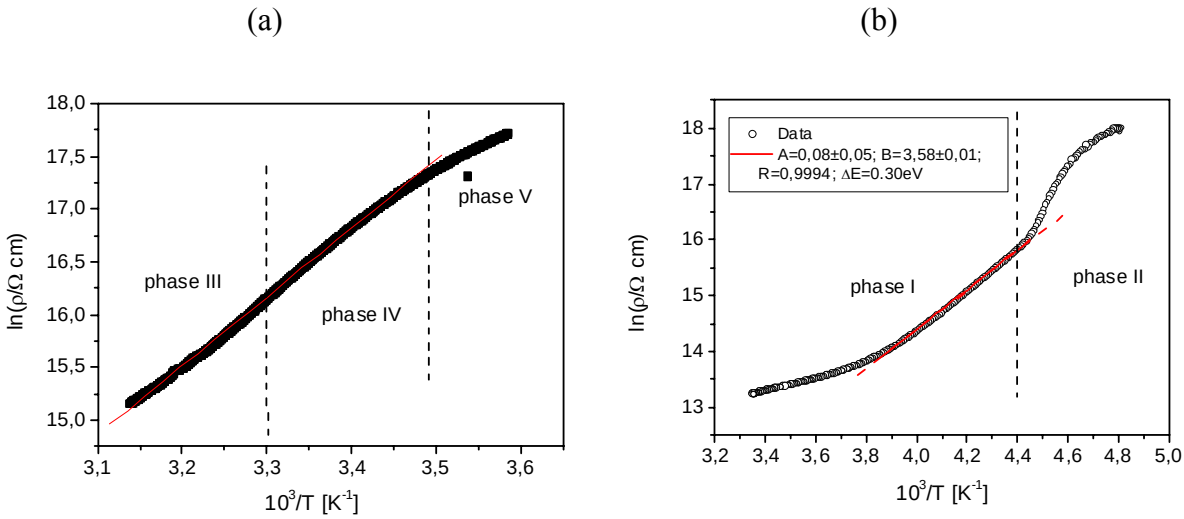

Figure 4.3 – *Arrhenius plot for $CH_3NH_3SnCl_3$* (a) *and $CH_3NH_3SnBr_3$* (b) *films. Vertical dashed lines indicate the transition temperatures between the different structural phases. The phase are pointed with Roman numbers starting from high temperature cubic phase (I) to more and more distorted phase (II, III, IV, V). The red (continuous) lines are the fitting curve of the data.*

On the other hand, one could also take into account the occurrence of two different bonding schemes of the Sn–Br–Sn bridges, the symmetric and the asymmetric one [14]. The symmetric configuration can be described as a typical "three-centers-four-electrons" bond (3c-4e) mainly using the p orbital of the central atoms. The asymmetric configuration, instead, can be described as a normal 2c-2e bond with an inter-anion interaction. The Sn–Br bond in the symmetric bridge has a higher ionic character than the (2c-2e) Sn–Br bond, where the charges are strongly localized. As a consequence the charge transfer mechanism is expected to be more efficient when symmetric bonds are present (higher temperature) in respect of the case of asymmetric ones (lower temperature). In this frame it should be not surprising to observe this strong increase of resistivity with decreasing temperature.

However, around 260 *K,* no structural transition are reported in the literature. Therefore the observed change in the slope cannot be related to any structural deformation. This type of "knee" in the conductivity is usually interpreted as a crossover between two independent conduction mechanisms. At higher temperatures the slope of resistivity (corresponding to ΔE = (0.10±0.01) *eV*) could indicate a transport mechanism dominated by defect trapping states in the film or by injection resistance at the gold contacts. This last type of problem cannot be excluded in any measurement because no analysis has been carried out on the compatibility between the contact work-function and the material band structure. As previously exposed, the greater band-gap and the depressed transport properties of chloride compound in respect to bromide and iodide ones (**Table 4.1**), are probably related to the large distortion of the perovskite octahedra connected to an enhanced stereochemical activity of Sn(5s) lone pair, when the halogen changes along the group 17 (VII A) (I → Br → Cl) in the structure.

	ρ_{300} ($\Omega \cdot cm$)	ΔE (eV)	E_g (eV)
$CH_3NH_3SnI_3$	3 x10^{-3}	Metal-like	0
$CH_2CH{=}NH_2SnI_3$	7 x10^{-3}	Metal-like	0
$CH_3NH_3SnBr_3$ *	0.52 x10^{6}	0.30	2.5
$CH_3NH_3SnCl_3$ *	3 x10^{6}	0.56	3.6

Table 4.1 – *Comparison between room temperature resistivity (ρ_{300}), activation energy (ΔE), and optical direct gap (E_g) of perovskite hybrid tin(II) compounds. (*) indicates measure on films.*

3.2.b Layered systems

In order to the realize electroluminescent devices, a deep understanding of the transport mechanisms and electrical properties of layered $(C_nH_{2n+1}NH_3)_2CuCl_4$ compounds is required.

The resistivity of the films at room temperature and in air is calculated from the DC resistance and the film thickness, by using the van der Pauw formula [[12]]. Resistivity are estimated to range between 10^3-10^4 $\Omega \cdot cm$, as reported in the **Table 4.2**. The main

contribution to the measurement error comes from the uncertainty in the thickness measurement that increases with increasing sample roughness and granularity. The resistivity is found to increase by increasing the organic layer thickness (increasing *n* of carbon atoms) and, thereby, by increasing the distance *d* between the perovskite layers (decoupling effect).

A systematic increase of the resistivity of all samples has been observed when the environmental humidity is eliminated, related to the strong hygroscopic nature of the films.

n	d (*Å*)	ρ_{300K} ($k\Omega \cdot cm$)
1	9.41	0.62±0.03
2	10.75	1.54±0.07
3	12.45	2.0±0.5
4	15.50	13±1

Table 4.2 – *Room temperature resistivity values measured on $(C_nH_{2n+1}NH_3)_2CuCl_4$ compound series where n= 1, 2, 3, and 4 are the number of carbon atoms in the alkyl chain. In the column d, the distances between the perovskite sheets in the different structures are reposted.*

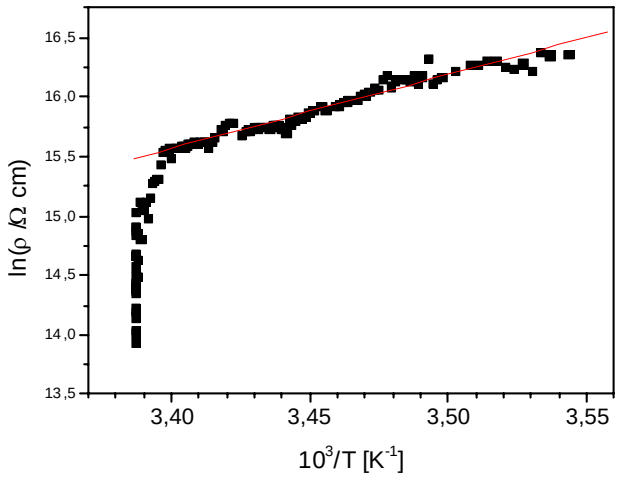

Figure 4.4 – *Arrhenius plot for $(CH_3NH_3)_2CuCl_4$ film. It is clear the two order of magnitude drop in the resistivity when the sample are sealed in helium atmosphere environment. The red line is the fitting curve of the data cooling the sample in cold helium vapours.*

The $(C_3H_7NH_3)_2CuCl_4$ films show a change to higher value (two-three order of magnitude) when the sample is sealed in helium atmosphere or in a vacuum environment,

as reported in the log-plot of resistivity in **Figure 4.4**. This occurs in a very short time interval. The temperature behavior of the resistivity of the films under vacuum (or inert atmosphere) follows a linear dependence in the Arrhenius plot with an activation energy $\Delta E = 0.54\ eV$.

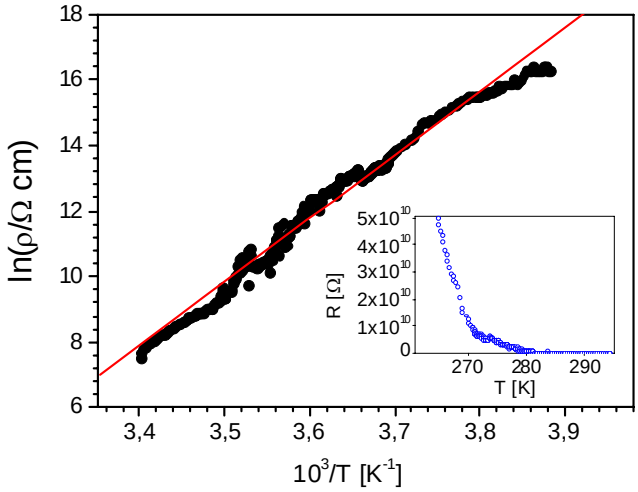

Figure 4.5 – *Arrhenius plot for a film of the layered perovskite compound $(C_2H_5NH_3)_2CuCl_4$ and the relative linear fit (red line) In the inset resistivity vs. temperature are presented* [16].

In literature [17] $(C_2H_5NH_3)_2CuCl_4$ is reported to be the more stable and the less hygroscopic compound of the copper(II) chloride series. The Arrhenius plot of the resistivity of the $(C_2H_5NH_3)_2CuCl_4$ film as a function of temperature is shown in **Figure 4.5**. In this case resistivity change with humidity is very small and the resistivity follows an exponential type behavior as a function of the temperature. These copper(II) halide systems are classified as charge-transfer (CT) insulators rather than Mott insulator accordingly to the Zaanen-Sawasky-Allen scheme [18], because the electronic gap is characterized by the CT excitation from ligand (Cl3$p\sigma$) to metal (Cu3d $_{x^2-y^2}$ upper Hubbard band) sites [19]. Nevertheless the data shown in **Figure 4.5** were fitted by the Mott insulator law, i.e.: $\rho = A\exp(E_g/2k_BT)$, where A is a constant, E_g is the band gap energy, k_B the Boltzmann's constant and T the temperature. By fitting of the experimental data, the gap energy, E_g, of the $(C_2H_5NH_3)_2CuCl_4$ film was estimated to be 3.32±0.02 eV. Such value is consistent with the CT $e_u \rightarrow b_{1g}$ energy transition resulting from the optical absorption measurement reported in Chapter 3 for the same compound at room temperature

(3.25±0.11 *eV*). This seems to indicate that the two CT phenomena involve the same energy band [16].

The greater stability and the reduced humidity sensitivity in respect to the other components of the series, the high excitonic binding energy and a relative high room temperature conductivity (10^{-3} $S{\cdot}cm^{-1}$) render $(C_2H_5NH_3)_2CuCl_4$ compound a good candidate to electroluminescence studies and UV-LED device realization.

4.3 Field effect devices

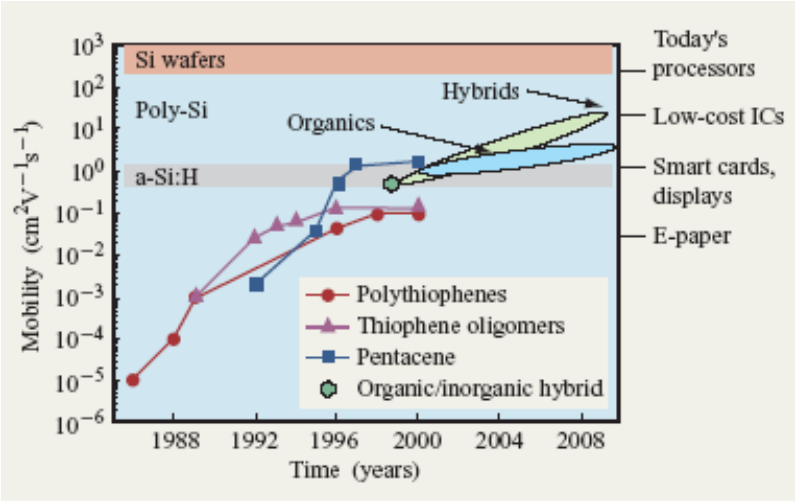

Figure 4.6 – *Performance of organic and hybrid semiconductor and possible future developments* [20].

In the last 20 years the research effort on new organic semiconductor active materials has lead to a dramatic improvement in their performances, due to innovative chemistry tools and processing techniques, as well as to the growing ability to understand and control the self-assembly and ordering processes of oligomers, polymers, and nanocrystals. In particular the research on semiconductive organic solids as thiophene oligomers [21,22], thiophene polymers [23,24], and the small pentacene molecule [25,26] has lead to an

improvement in the mobility of these materials by five order of magnitude in the last few years (**Figure 4.6**).

As already mentioned, the hybrid materials are specially interesting in this framework since they can combine the higher carrier mobility of ionic and covalently bonded inorganic semiconductors with the simple, low-cost and low-temperature thin-film techniques that make organic semiconductors exciting as alternative channel materials. The self-assembling and long range ordering of these hybrid materials can enhance π-orbitals overlap of neighboring conjugated molecules and this is the key to improve the carrier mobility. The mobility μ, in fact, is one of the most important parameters to access the performances of a semiconductor compound in the fabrication of TFT devices. It quantifies the average charge carrier drift velocity per unit electric field and its value largely affects the switching speed between the ON and OFF states of the final transistor [27].

In this context, field effect represent a powerful investigation tool, allowing the study of the electrical properties of the organic semiconductors and the related interfaces with other organic or inorganic layers, by inducing a reversible electron doping without modifying the structural properties and the stoichiometry of the material. This is done through the realization of specifically designed FET devices, and can allow the accurate determination of the carrier mobility.

In crystalline silicon, Metal-Insulator-Semiconductor FET devices (MISFET), the dependence of the I_{DS} current between drain and source on gate voltage (V_G) and V_{DS} voltages can be generally described by simple analytical equations [28]. In particular, if $V_G > V_{DS}$, the device operates in the so-called "linear regime" and I_{DS} is given by:

$$I_{DS} = \frac{WC_i\mu}{L} \cdot V_{DS}(V_G - V_{th}) \qquad (4.2),$$

where V_{th} is the threshold voltage, W and L are the width and length of the semiconducting channel, C_i is the MIS capacitance per unit square, and μ is the charge mobility. In this case, the channel behaves as a variable resistor which can be linearly tuned by V_G. On the other hand, when $V_G < V_{DS}$, due to the *pinch-off* of the accumulation layer, the FET works in the saturation regime and the linear dependence described by (4.2) is substituted by a quadratic dependence on the gate voltage, determined by the equation:

$$I_{DS} = \frac{WC_i\mu}{2L} \cdot (V_G - V_{th})^2 \qquad (4.3).$$

The mobility can be directly calculated both in the linear or saturation regimes, by rearranging equations (4.2) and (4.3), respectively. It is easy to find that in the first case μ can be evaluated by:

$$\mu = \frac{L}{WC_i V_{DS}} \cdot \left.\frac{\partial I_{DS}}{\partial V_G}\right|_{V_{DS}} \qquad (4.4),$$

whilst, in the case of saturation regime, we have:

$$\mu = \frac{2L}{WC_i} \cdot \left(\frac{\partial \sqrt{I_{DS}}}{\partial V_G}\right)^2 \qquad (4.5).$$

The MISFET basic model does not account for contact resistances. However, due to the energy barriers that can be formed in these regions opposing to charge injection, the device performances can be greatly affected by contact resistances [29]. It is also necessary to remember that (4.2) and (4.3) are rigorously valid only if the channel aspect ratio W/L is very high (>100). Otherwise, effective W_{eff} and L_{eff} must be considered and the current distribution has to be determined by numerical methods. A high relative dielectric constant ε_r of the insulating layer can further complicate this evaluation.

Recently, Kagan and his IBM collaborators [30] have demonstrated the first organic–inorganic hybrid material as the semiconducting channel in a TFT, using the hybrid perovskite $(C_6H_5C_2H_4NH_3)_2SnI_4$. **Figure 4.7** depicts the organic–inorganic TFT device structure where a typical structure was utilized. Thin films of the hybrid perovskite are spin-coated from a methanol solution, in an inert atmosphere, onto thermally oxidized, degenerate n-doped silicon wafers where the SiO_2 layer acts as the gate insulator with thickness of 400, 1500, or 5000 Å. The silicon wafer is used as the gate electrode, and high work-function metals, such as Pd, Au, or Pt, are deposited as source and drain contact by e-beam evaporation in both top and bottom configurations. From TFT characteristic curves, the field-effect mobility for the device resulted to be μ = 0.61 $cm^2/V{\cdot}s$, and the I_{ON}/I_{OFF} ratio is ~10^6. This mobility value is comparable with pentacene and amorphous Si mobilities (~1 $cm^2/V{\cdot}s$) (**Table 4.3**).

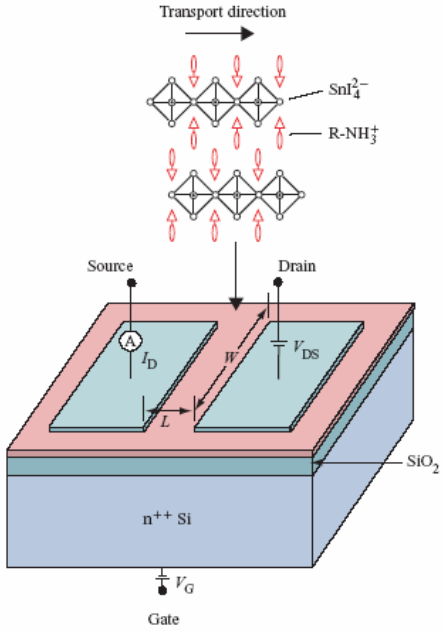

Figure 4.7 – *Schematic diagram of a TFT device structure employing a layered organic–inorganic perovskite as the semiconductor channel* [10].

Semiconductor	**Composition**	**Mobility** ($cm^2/V{\cdot}s$)
Silicon	Silicon crystal	300-900
	Poly-silicon	50-100
	Amorphous silicon	~1
Pentacene	$C_{22}H_{14}$	~1
Phenethylamine–tin(II) iodide	$(C_6H_5C_2H_2NH_3)_2SnI_4$	~1
α.ϖ–dihexil-sexithiophene	DH-6T	10^{-1}
α.ϖ–dihexilanthra-dithiophene	$C_{30}H_{34}S_2$	10^{-1}
Regioregular poly (3-hexylthiophene)	$[C_6H_{13}SC_4H]_n$	10^{-1}
Alkylamine–tin(II) tetraiodide	$(C_nH_{2n+1}NH_3)_2SnI_4$	$\sim 10^{-3} - 10^{-2}$
Methylamine–tin(II) bromide	$CH_3NH_3SnBr_3$	$\sim 10^{-5} - 10^{-2}$
Methylamine–copper(II) tetrachloride	$(CH_3NH_3)_2CuCl_4$	10^{-4}

Table 4.3 – *Comparison and mobility of classes of organic, inorganic and hybrid semiconductors.*

4.3.a Device realization

The FET basic working element can be represented by an equivalent capacitor, formed by a semiconducting channel between two metallic contacts (source and drain), the insulating layer and the gate metallic contact. By applying an appropriate gate voltage V_G, the charge carrier density in the semiconducting channel is electrostatically modulated. It is quite clear that the charge carrier density modulation in the semiconductive layer is strictly dependent on the value of the equivalent capacitor in the FET configuration, which, in turn, is directly proportional to the dielectric constant ε_r of the insulating layer. From an application point of view, the use of a high dielectric constant layer in the fabrication of FET devices is really attractive for the reduction of the operating voltage. Moreover this allows a greater sensitivity in mobility measurements [31,32].

Field effect devices based on STO substrate were recently demonstrated for tuning the carrier density in $Nd_{1.2}Ba_{1.8}Cu_3O_y$ thin films [33] and in submicrometric arrays of gold dots [34] by our research group. The resistivity of the considered samples was modulated by more than one order of magnitude. STO substrates resulted to be particularly suitable as gate oxide, because of the high dielectric constant ε_r. Our measured value was close to 300 at room temperature, in good agreement with the literature data [35]. It is worth to mention that such a ε_r value guarantees an insulator capacitance of about 0.5 nF/cm^2, (with STO thickness of 500 μm). Consequently, the induced charge density per volt can be estimated to be about:

$$\frac{\Delta n_S}{Vgate} = 3.31 \times 10^9 \frac{1}{cm^2 \cdot Volt}. \qquad (4.6).$$

A prototype of the field effect device (FET) was fabricated in this thesis work, following the classical scheme of the thin film transistors (TFT) [28]. This is schematized in **Figure 4.8**, where the geometry of the source-drain gold contacts is shown. In our set-up, a $CH_3NH_3SnBr_3$ film of hybrid semiconductive compounds, deposited by SSTA, represent the conducting channel and the $SrTiO_3$ (STO) substrate is the insulating layer. Two large gold contact (separated by 100 μm) are deposited over the hybrid film (top contact configuration) by thermal evaporation and shadow mask techniques. The use of STO as

dielectric in the FET configuration, also in this case guarantees the possibility to largely modulate the charge carrier density in the organic films and to study their mobility in the strong charge carrier accumulation regime [[36]]. The gate contact was applied with a silver paint on the bottom of STO substrate.

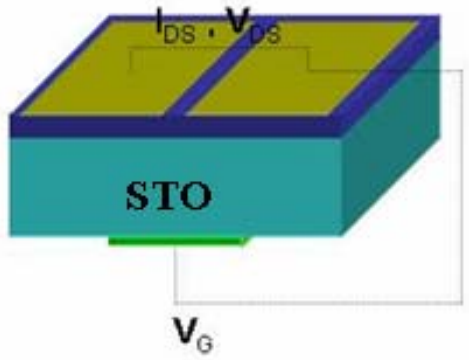

Figure 4.8 – *Layout of the field effect device* [[37]].

4.3.b Device characterization

The FET devices were characterized measuring, under vacuum, the linear transfer characteristic I_{DS} vs. V_G. The film mobility was calculated from the related transconductance:

$$g_m = \left.\frac{\partial I_{DS}}{\partial V_G}\right|_{V_{DS}} = \frac{W \cdot C_i \cdot \mu \cdot V_{DS}}{L} = A\mu \qquad (4.7)$$

attainable from formula (4.4) for the linear regime, where $A = (W \cdot C_i \cdot V_{DS})/L$ is constant for a given device structure once the voltage V_{DS} is fixed .

According to the basic FET working principle, the electrostatic doping induced by the gate voltage modifies the number of carriers, thus modulating the channel resistance.

In **Figure 4.9** the source-drain current (I_{DS}) vs. the gate voltage, V_G, of $CH_3NH_3SnBr_3$ hybrid based device is reported at different temperatures. The measurements were done at V_{DS} = 50 V. The leakage current measured between the gate and the source was monitored and resulted to be less than 1 *nA* during the measurements.

The field effect modulation decreases the channel current flow, I_{DS} , when a positive gate voltages was applied while a strong I_{DS} increase was observed with negative gate voltages. This is consistent with a hole type carriers picture. An increase up to one order of magnitude of the current has been observed for negative V_G values.

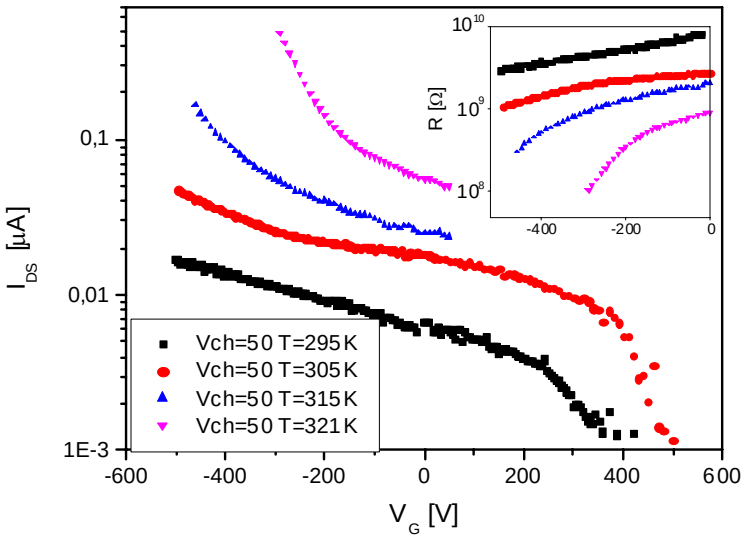

Figure 4.9 – *Transfer curves for $CH_3NH_3SnBr_3$ FET device obtained at different temperatures. In the inset we show channel resistance vs. gate voltage.*

The channel resistance, R_{DS}, is shown in the inset of **Figure 4.9**. At $V_G = 0$, R_{DS} varies from about $8x10^8$ Ω at T = 321 *K*, to about 10^{10} Ω at T= 295 *K*. The data fit an exponential Arrhenius-type function, from which an activation energy ~ 0.16 *eV*, is deduced. This activation energy is in reasonable agreement with the corresponding value obtained from the resistivity measurements close to room temperature (0.10 *eV*) in the previous paragraph on $CH_3NH_3SnBr_3$ films, much lower in respect to the value reported for pressed powders (0.30 *eV* [2,14]), and attributed to trapping conduction mechanisms in this temperature range.

In **Figure 4.10** the mobility vs. temperature is reported for different gate voltage values, since it is known that the FET mobility μ varies with applied field. In the inset of **Figure 4.10**, the mobility vs. field is shown, obtained by the trans-characteristic data at constant temperatures. An exponential dependence on the field is observed at the higher temperatures**.** At $V_G = -300$ *V* and T = 295 *K*, μ, was estimated to be approximately $1x10^{-5}$

$cm^2/(V{\cdot}s)$. At constant field, the mobility rapidly increased with temperature, and at 320 *K* was almost two order of magnitude higher than at room temperature. The field dependence of the mobility is consistent with the multiple trapping and release (MTR) model [38], under the assumption that a narrow delocalized band is associated with a high concentration of localized levels that act as traps. During their transit through the delocalized levels, the charge carriers interact with the localized levels through trapping and thermal release. This scenario is consistent with the temperature dependence of the resistivity and of the mobility and indicates that the films *p*-type conduction is dominated by trapping around room temperature.

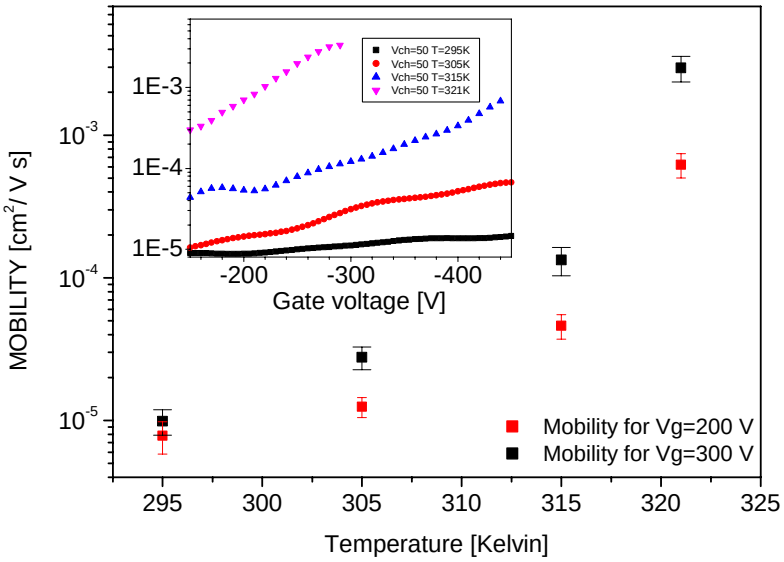

Figure 4.10 – *Mobility-temperature dependence choose two different gate voltage for mobility calculation. In the inset it was presented field dependence of mobility in $CH_3NH_3SnBr_3$*

From analogue preliminary analysis on $(CH_3NH_3)_2CuCl_4$ films, the layered hybrid results a *p*-type materials with an estimated mobility at room temperature of about $2{\cdot}10^{-4}$ $cm^2/V{\cdot}s$.

4.4 Sensitivity of hybrid systems as humidity sensors

As in the case of $(CH_3NH_3)_2CuCl_4$ films, already reported in **Fig. 4.4,** where a two order of magnitude drop in the resistivity was observed when the sample was exposed to humidity, in $CH_3NH_3SnX_3$ (X = Cl and Br) an even larger resistance change, of two-three order of magnitude changing the environmental condition. As an example exposing the film surface from air to vacuum, the film resistance increases dramatically and with very good repeatability.

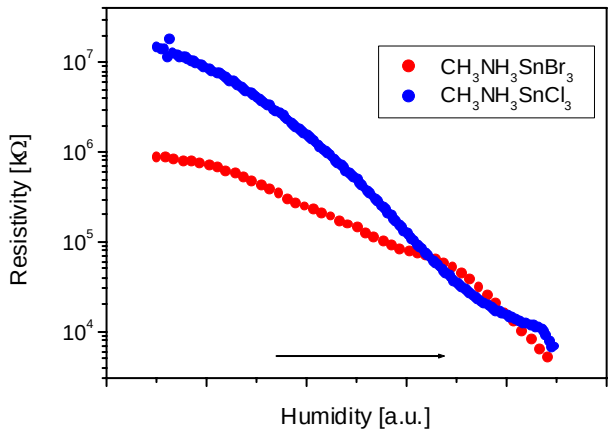

Figure 4.11 – *Change in the resistance of $CH_3NH_3SnCl_3$ (blue points) and $CH_3NH_3SnBr_3$ (red points) films with the change of humidity percentage in the ambient. On the x-axis humidity is presented as arbitrary unit because of in this type of measurements it is not possible control the effective real humidity value, the black arrow indicates increasing humidity.*

All the compounds reviewed in this thesis are halide salts and it is known that ionic solids are typically reactive to polar molecules. The strong influence of ambient condition on films transport properties shown in **Figures 4.4** and **4.11** due to air exposure, was considered to be due to humidity. This has stimulated further measurements to verify the possibility to use these materials in resistive sensor applications.

Rapid advancements in semiconductor technology have made possible the realization of high quality humidity sensors with good resistance to chemical and physical contaminants, at low prices. No single sensor, however, at the moment, is fully satisfactory for all applications. In fact resistive, capacitive, and thermal conductivity sensing technologies each offer distinct advantages. Resistive sensors are interchangeable, usable for remote

locations, and cost effective. Capacitive sensors provide wide RH range and condensation tolerance, and, if laser trimmed, are also interchangeable. Thermal conductivity sensors perform well in corrosive environments and at high temperatures. For most applications, therefore, the environmental conditions dictate the sensor choice.

The most important specifications to keep in mind when selecting a humidity sensor are: accuracy, repeatability, interchangeability, long-term stability, ability to recover from condensation, resistance to chemical and physical contaminants, size, packaging, and cost effectiveness.

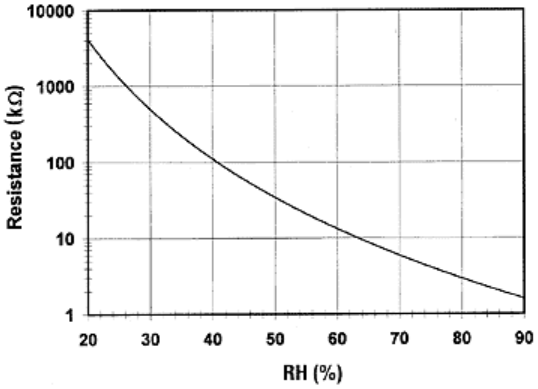

(a)

(b)

Figure 4.12 – (a) *The exponential response of the resistive sensor, plotted here at 25°C, is linearized by a signal conditioner for direct meter reading or process control.* (b) *Resistive sensors are based on an interdigitated or bifilar winding. After deposition of a hydroscopic polymer coating, their resistance changes inversely with humidity. The Dunmore sensor (far right) is shown 1/3 size.*

Resistive humidity sensors measure the change in electrical impedance of a hygroscopic medium such as a conductive polymer, salt, or treated substrate. The electrical contacts consist of noble metal electrodes either deposited on a substrate, coated with the salt or conductive polymer, by photoresist techniques or wire-wound electrodes on a plastic or glass cylinder. The impedance change is typically an inverse exponential relationship to humidity (see **Figure 4.12**). The sensor absorbs the water vapour and ionic functional groups are dissociated, resulting in an increase in electrical conductivity. The response time for most resistive sensors ranges from 10 to 30 s for a 63% step change. The impedance range of typical resistive elements varies from 1 *k*Ω to 100 *M*Ω. Most resistive sensors use symmetrical AC (30 *Hz* to 10 *kHz*) excitation voltage with no DC bias to

prevent polarization of the sensor. The resulting current flow is converted and rectified to a DC voltage signal for additional scaling, amplification, linearization, or A/D conversion.

In residential and commercial environments, the life expectancy of these sensors is >>5 yr., but exposure to chemical vapors and other contaminants such as oil mist may lead to premature failure. An other drawback of some resistive sensors is the tendency to relevant shifts of the reference values when exposed to condensation if a water-soluble coating is used.

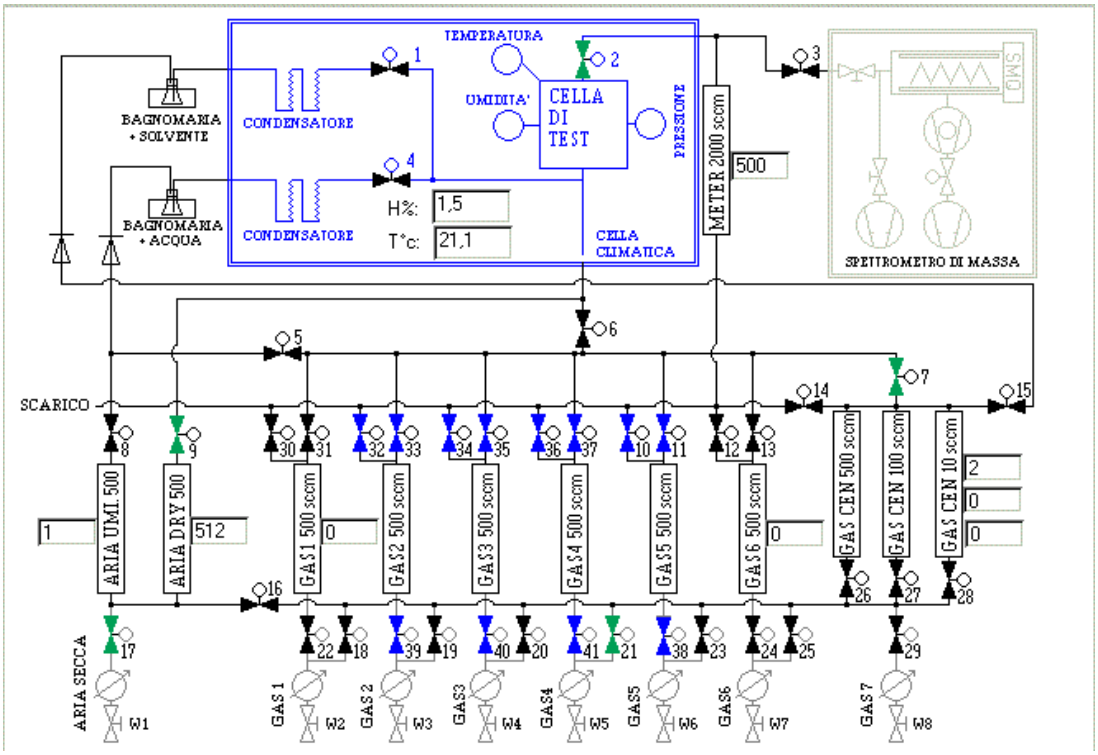

Figure 4.13 – *Synoptic scheme of gas sensor calibration apparatus sited c/o ENEA of Portici (Napoli)* [39].

In the case of our hybrid compounds, the larger effect was observed in $CH_3NH_3SnCl_3$ (**Figure 4.11**). A film of this composition has been contacted with large gold pads (0.1 *mm* separated, see **Figure 4.15**) to create a prototype of resistive sensor. This preliminary device has been examined by a specific analysis carried out by a gas sensor calibration apparatus (**Figure 4.13**) in which it is possible to monitor and control pressure, flow rate, actual gas composition, humidity and environment temperature. 1*V* DC signal was applied between the device electrical contacts. The current flowing in the film was measured with a pico-amperometer. When a dry atmosphere (N_2, CO, NO_2, and O_2) was flowing into the

test chamber, no relevant changes in the current was observed, while a current sensitivity to water vapour was evident when humid air was flowed in the testing chamber.

To determine the device characteristics, this was tested in an experimental run of about 24 h in the test chamber at constant temperature of 25°C. At regular time intervals, the humidity percentage was increased from the base value of 30% gradually up to 70% following the step like profile reported as a blue line in **Figure 4.14**. The device response is reported on the same **Figure 4.14**. The measurement indicate at a first sight the good device behaviour. However a "base-line" problem is evident. In fact when humidity switches back to the starting state (30%) the measured device current does not fully recover to the original value. In principle this effect can be correct with electronics, however when humidity increases to the highest values the sample shows an irregular behaviour with high current and discharges, and the response results to be strongly altered.

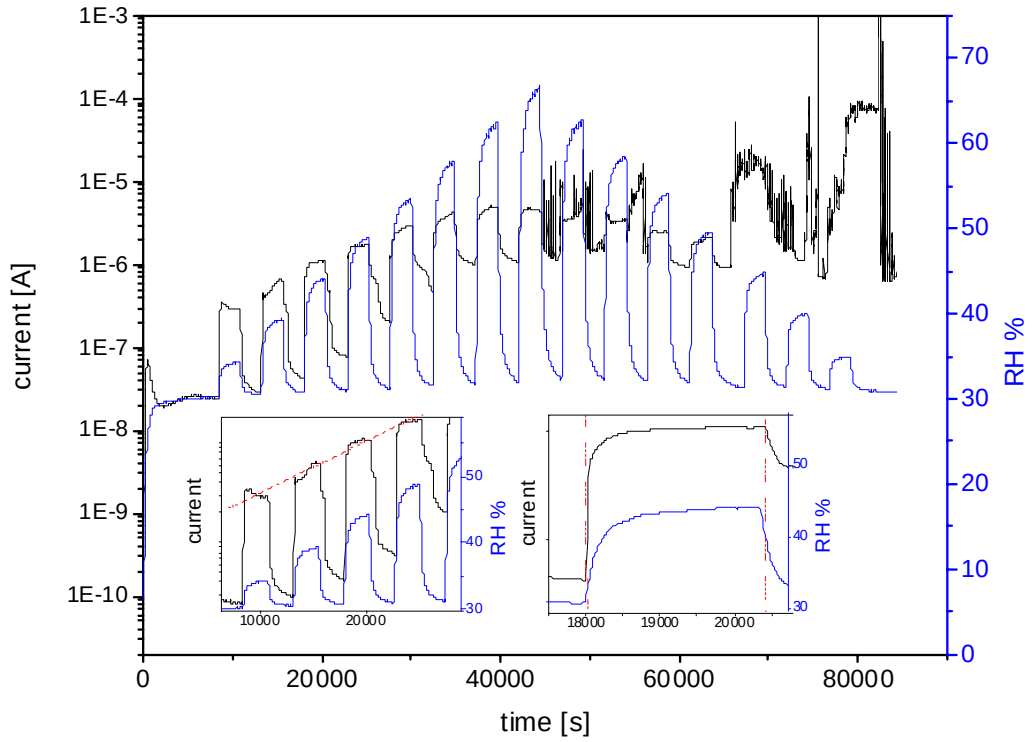

Figure 4.14 – *Device signal obtained at room temperature introducing increasing humidity percents (30-70 %) in the testing chamber. In blue a commercial humidity device current signal is shown to comparison and to control effective humidity percent. In the insets are shown two enlargement of principal plot* [Reported with permission from ENEA-Portici].

As shown in **Figure 4.15**, after that the anodic contact is extensively deteriorated, that should be probably related to ionic and electrolytic conduction in humid atmosphere and indicates a condensation problem on the film surface. However at low humidity levels (less than 40%), the material results to respond to humidity variations with good linearity and sensitivity, and guarantying very high accuracy as shown in the inset of **Figure 4.14**. In particular the response time at humidity variations (black line, 10-90% in only 40 s) is ten time shorter than that of the reference commercial sensor (blue line, 10-90% in 600 s). Finally the use of interdigital electrical contacts and low frequency AC signals, could improve sensitivity and stabilize current conduction in the device.

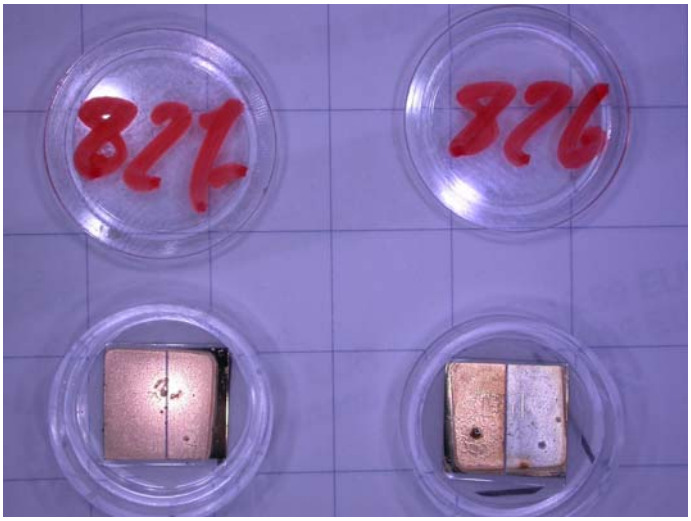

Figure 4.15 – *Picture of two devices of $CH_3NH_3SnCl_3$ with large gold pads. On the right the sample after the measure, with the anodic gold contact strongly damaged. On the left for comparison a twin sample not yet measured.*

Bibliography

[1] C. P. Tigges, J. E. Drumheller, and L. O. Snively, *J. Appl. Phys.*, **54**, 4573 (1983).

[2] N. Onoda-Yamamura, T. Matsuo, and H. Suga, *J. Chem. Thermodynamics*, **23**, 987 (1991).

[3] D. B. Mitzi, C. A. Field, Z. Schlesinger, and R. B. Laibowitz, *J. Solid States Chem.*, **114**, 159 (1995).

[4] D. Weber, *Z. Naturforsch.*, **33b**, 862 (1978).

[5] K. Yamada, T. Matsui, T. Tsuritani, T. Okuda, and S. Ichiba, *Z. Naturforsch.*, **45a**, 307 (1990).

[6] D. B. Mitzi, and K. Liang, *J. Solid States Chem.*, **134**, 376 (1997).

[7] D. B. Mitzi, S. Wang, C. A. Feild, C. A. Chess, and A. M. Guloy, *Science*, **267**, 1473 (1995).

[8] D. B. Mitzi, C. A. Feild, W. T. A. Harrison, and A. M. Guloy, *Nature*, **369,** 467 (1994).

[9] David B. Mitzi, *Progress in Inorganic Chemistry*, Vol **48**, Ed. by K. D. Karlin, Jonh Wiley & Sons, Inc. (1999).

[10] D. B. Mitzi, K. Chondroudis and C. R. Kagan, *IBM J. Res. & Dev.*, **45**, N°1 (2001).

[11] R. E. Wasylishen, O. Knop, and J. B. Macdonald, *Solid State Commun.*, **56**, 581 (1985)

[12] L. J. Van der Pauw, *Phylips Res. Repts.*, **26**, 220 (1958).

[13] L. Glasser, *Chem. Rev.*, **75**, 21 (1975).

[14] K. Yamada, H. Kawaguchi, T. Matsui, T. Okuda, and S. Ichiba, *Bull. Chem. Soc. Jpn.*, **63**, 2521 (1990).

[15] K. Yamada, Y. Kuranaga, T. Ueda, S. Goto, T. Okuda, and Y. Furukawa, *Bull. Chem. Soc. Jpn.*, **71**, 127 (1998).

[16] F. Chiarella, A. Zappettini, P. Ferro, T. Besagni, F. Licci, A. Cassinese, M. Barra, R. Vaglio, and C. Aruta, *Cryst. Res. Technol.* **40,** 1028 – 1032 (2005).

[17] J.P Steadman and R.D. Willett, *Inor. Chim. Acta*, **4**, 367 (1970).

[18] J. Zaanen, G. A. Sawatzky, and J. W. Allen, *Phys. Rev. Lett.*, **55**, 418 (1985).

[19] J. Moritomo, and Y. Tokura, *J. Chem. Phys.*, **101**, 1763 (1994).

[20] J. M. Show, and P. F. Seidler, *IBM J. Res. & Dev.*, **45**, 3 (2001).

[21] G. Horowitz, D. Fichou, X. Peng, Z. Xu, and F. Garnier, *Solid State Commun.*, **72,** 381 (1989).

[22] F. Garnier, R. Hajlaoui, A. Yasser, and P. Srivastava, *Science*, **265,** 1684 (1994).

[23] J. H. Burroughes, C. A. Jones, and R. H. Friend, *Nature*, **335,** 137 (1988).

[24] A. R. Brown, A. Pomp, C. M. Hart, and D. M. de Leeuw, *Science*, **270,** 972 (1995).

[25] A. Dodabalapur, L. Torsi, and H. E. Katz, *Science* **268,** 270 (1995).

[26] C. D. Dimitrakopoulos, S. Purushothaman, J. Kymissis, A. Callegari, and J. M. Shaw, *Science*, **283,** 822 (1999).

[27] S. M. Sze, *Physics of Semiconductor Devices*, Wiley, New York, (1981).

[28] G. Horowitz, *Advanced Materials*, **10**, 365 (1998).

[29] L. Bürgi, T. J. Richards, R. H. Friend, and H. Sirringhaus, *J. Appl. Phys.*, **94**, 6129 (2003).

[30] C. R. Kagan, D. B. Mitzi, and C. Dimitrakopoulos, *Science*, **286,** 945 (1999).

[31] C. D. Dimitrakopoulos, J. Kymissis, S. Purushothaman, D. A. Neumayer, P. R. Duncombe, R. B. Laibowitz, *Advanced Materials*., **11**, 1372 (1999).

[32] C . Bartic, H. Jansen, A. Campitelli, S. Borghi, *Organic Electronics*, **3**, 65, (2002).

[33] A.Cassinese, G. M. DeLuca, A.Prigiobbo, M.Salluzzo, and R.Vaglio, *Applied Phys. Lett.*, **84**, 3933 (2004).

[34] M. Barra, A. Cassinese, F. Chiarella, W.Goedel, D. Marczewski, P. Terno, and R. Vaglio, *Eur. Phys. J. B* **46**, 497–500 (2005).

[35] D.Matthey, S.Gariglio, and J.-M.Triscone, *Applied Phys. Lett.*, **83**, 3758 (2003).

[36] M. Barra, M. Biasiucci, A. Cassinese, F. Chiarella, P. D'Angelo, A. Prigiobbo, and R.Vaglio, *submitted on Journal of Applied Physics.*

[37] F. Chiarella, P. Ferro, F. Licci, M. Barra, M. Biasiucci, A. Cassinese, and R. Vaglio, *submitted on Applied Physics A*.

[38] P.G.Le Bomber and W.E.Spear, *Phys.Rev.Lett.*, **25**, 509 (1970).

[39] L. Quercia, F. Cerullo, V. La Ferrara, G. Di Francia, C. Baratto, G.Faglia, *Phys. Stat. Sol. (a)*, **182**, 473 (2000).

Conclusions

In the development of this thesis work, many of the pre-established aims have been reached, in the film deposition and characterizations, and the comprehension of the correlation between the structures of our hybrid compounds and their physical properties.

The high flexibility of Single Source Thermal Ablation technique for hybrid film deposition has been fully demonstrated. The films obtained in the optimized deposition conditions on different substrates (crystalline, amorphous and flexible), resulted to be, by the different performed analysis, to have good structural, morphological and optical quality.

About the structure-property correlation, in the 2D compounds we observed that optical properties do not depend on changes of the alkylammonium molecule and that room temperature resistivity decreases with increase of the perovskite sheets coupling. In 3D tin(II) structures, it has been observed that energy gap and resistivity increase when the halogen atom change in the structure along the series I → Br → Cl.

All the analyzed 2D layered copper structures show a photoluminescence emission in the UV. In particular the $(C_2H_5NH_3)_2CuCl_4$ compound, thanks to its high stability, low hygroscopicity, and good conduction properties, resulted to be a good candidate for UV-LED applications.

By field effect measurements and analysis, it has been observed that in the realized films of the hybrid compounds, the conduction is due to hole carriers. Preliminary measurements on the sensitivity to humidity have shown interesting sensor properties of the 3D hybrids, with excellent perspectives for future practical applications.

Acknowledgments

I wish to thank Dr. Francesca Licci, Prof. Ruggero Vaglio, and Dr. Antonio Cassinese for their decisive contribution to this work.

I gratefully acknowledge Mrs. P. Ferro and Mr. T. Besagni for the collaboration and technical support in the chemical synthesis, film depositions and X-ray measurements; Dr. M. Barra, and Dr. M. Biasiucci for their contributions in the transport properties analysis and Field Effect characterization; Dr. A. Zappettini for the optical characterization of the films; Dr. P. Perna and Prof. U. Scotti di Uccio for X-ray film structural deepening; Dr. E. Massera and Dr. L. Quercia, for gas calibration of sensor device; Dr. G. Cantele, Prof. D. Ninno, and Prof. G. Iadonisi, for their theoretical view and discussions on the hybrid structure and properties; Mr. S. Marrazzo and Mr. A. Maggio for their untiring technical support; Dr. G. M. De Luca and Dr. M. Salluzzo for fruitful discussions.

Finally it is a will and pleasure for me to thank the CNR-IMEM Institute of Parma, where a noteworthy part of my work was carried out, for the hospitality and handless supply; ENEA Institute of Portici (Dr. L. Di Francia) for the precious collaboration; and ST Microelectronics for the financial support of my PhD studies.